A Study of Loading Parameters that Affect DNA Electrophoresis in Microdevices

by

Maribel Vazquez

Submitted to the Department of Mechanical Engineering
in partial fulfillment of the requirements for the degree of

Doctor of Science in Mechanical Engineering

at the

MASSACHUSETTS INSTITUTE OF TECHNOLOGY

August 2001

Author . . . .
Department of Mechanical Engineering
August 20, 2001

Certified by . . . .
Daniel Ehrlich
Principal Investigator, Whitehead Institute
Thesis Supervisor

Certified by . . . .
Gareth McKinley
Professor of Mechanical Engineering
Thesis Supervisor

Accepted by . . . .
Ain Sonin
Chairman, Department Committee on Graduate Students

A Study of Loading Parameters that Affect DNA Electrophoresis in Microdevices

by

Maribel Vazquez

Submitted to the Department of Mechanical Engineering
on August 20, 2001, in partial fulfillment of the
requirements for the degree of
Doctor of Science in Mechanical Engineering

Abstract

Electrophoresis of DNA has become particularly attractive in today's age of bio-technology. The goal of the present research is to optimize the the gel-loading and sample-loading protocols used prior to electrophoresis within microfabricated devices. During gel-loading, electrophoretic channels are filled with a polymer matrix prior to their use in DNA separations. The injection rate is constrained by the desire to minimize shear-induced degradation of the polymer molecules. In this study, measurements of the zero shear-rate viscosity of linear polyacrylamide (LPA) solutions are used to determine the LPA molecular weight before and after gel-loading protocols. The results demonstrate induced molecular degradation of polymer molecules even when matrixes are injected at minimal flow rates of 1 microliter per minute. Next, digital images are used to analyze the electrophoretic migration of DNA samples during conventional sample-loading and injection protocols. Experimental data illustrate that the 'stacked' DNA sample plug is comprised of distinct concentrated populations of DNA molecules that migrate with the same mechanism of transport. This study produced a detailed exploration of the injection process as well as a standardized method to measure the level of 'stacking' exhibited by a system. Additionally, a novel high voltage injection protocol correlates increases in resolution and separation with higher levels of sample stacking during injection. Developments realized through these experiments demonstrate great promise for upgraded electrophoretic protocols and future microdevices.

Thesis Supervisor: Daniel Ehrlich
Title: Principal Investigator, Whitehead Institute

Thesis Supervisor: Gareth McKinley
Title: Professor of Mechanical Engineering

Biographical Sketch

Maribel Vazquez received a bachelor's degree from the Sibley school of Mechanical and Aerospace Engineering at Cornell University in 1992. She began her career as a mechanical engineer at Intel Corporation where she was part of the cleanroom construction, process manufacturing and microcontamination teams. She left industry to pursue graduate study in 1995 and received a master's degree from the department of mechanical engineering at the Massachusetts Institute of Technology in 1996. Maribel completed her MIT doctoral study as part of the Whitehead Institute for Biomedical Research and will join the faculty of the biomedical engineering center at the City College of New York (CCNY) in September of 2001.

Acknowledgments

I would like to thank all of the people who have contributed to the completion of this doctoral thesis. First, a large thanks to my committee whose critique and advice helped navigate me throughout this research. Second, many thanks to all of my friends and officemates at MIT and the Whitehead Institute who offered various levels of support ranging from biology tutorials to friendly chats over midnight coffee. Lastly, I would like to thank my family, and in particular my husband, Alex Iosilevich, for his continued support throughout these past 4 years. I could not have finished this without you. Thank you.

Contents

List of Figures

List of Tables

Chapter 1

Introduction

1.1 Overview

Electrokinetics describes phenomena that incorporate the interaction between solid surfaces, ionic solutions and macroscopic electric fields. Two of the most widely used electrokinetic systems in engineering applications are electrophoresis and electro osmosis. Electrophoresis is the induced migration of charged ions under the influence of an externally applied electric field. Electro osmosis is the bulk motion of a liquid relative to a stationary, charged surface under the influence of an external field [1], [2]. The work discussed presently is specifically focused on the electrophoresis of DNA molecules.

Electrophoresis is the single most useful technique for the analysis and separation of proteins and nucleic acids. Its usefulness is based upon its high resolution and applicability to a broad range of molecules ranging from simple ions to living cells. In the medical field alone, electrophoretic techniques have lead to the discovery of the molecular basis of such blood diseases as anemias and protein deficiencies [3]. Further, electrophoresis is a non-destructive technique whose effects do not harm delicate biological structures such as proteins and DNA.

Electrophoresis of DNA has become particularly attractive in this age of bio-technology as electrophoretic methods have enabled the mapping of the human genome [4] as well as the development of sophisticated tools for use in forensic science [5], [6] and diagnostics [7], [8]. The current work addresses the recent improvements implemented in a microfabricated system used for the separation of DNA. The first chapter details the history and evolution of electrophoretic systems, reviews the analytical description of the electrophoretic process itself, and presents a detailed discussion of key system components and their properties. The second chapter addresses new protocols for 'gel-loading' that introduce the sieving matrix into the channel without molecular degradation of the polymer solution. Next, the third section discusses new protocols for DNA 'sample-loading' based upon the real time motion of DNA molecules visualized through fluorescence microscopy. Further, chapter three also addressees new operational protocols that utilize high voltages for improved electrophoretic injection. Lastly, chapter four discusses the future of the electrophoresis field and highlights several specific areas of research that show great promise.

1.1.1 Introduction

Electrophoresis is performed to achieve the separation of charged species by molecular size. The sample to be separated is generally comprised of different sized molecules dissolved within an electrolyte buffer that carries positiv and negative ions. The solution is placed within a channel, or tray, and an electric field is applied across it, typically by using electrodes [10]. Charged molecules are drawn by the field towards the oppositely charged electrode and separate from one another based upon their speed of migration. Positively charged ions, called cations, migrate towards the negatively charged electrode, the cathode, while negatively charged ions, called anions, migrate towards the positively charged anode. As expected, neutral solutes are not attracted to either electrode. The molecular rate of migration induced by the electric field depends upon many factors, such as the strength of the field, the size and shape of the molecule, and temperature of the surrounding electrolyte buffer [9], [11], [41]. Separation is accomplished when a detector can identify different populations of DNA molecules that migrate with distinct velocities within the channel or tray.

Many molecules, such as proteins and carbohydrates, can be separated in free solution because they exhibit size-dependent charges [12] [13]. DNA, however, requires the support of an external matrix for sieving by molecular size because its negative charge is evenly distributed throughout the molecule regardless of its length [12], [14], [15]. Consequently, a DNA molecule 100 bases in length has the same ionic charge as a DNA molecule 1000 bases in length. This is unfortunate because it indicates that DNA samples of all sizes migrate with near identical velocities under the same imposed field in free solution. As a result, DNA separations must utilize an external matrix that imposes a size-dependent, frictional force on the molecules [16], [17]. The frictional force exerted by the external matrix acts as a molecular sieve because smaller molecules of the sample, less affected by friction, navigate quickly through the matrix pores. Conversely, the velocity of larger molecules is significantly reduced by the frictional losses experienced during migration and, thus, migrate more slowly.

In this manner, smaller molecules separate from a sample first, followed by molecules of increasing molecular size.

1.1.2 Evolution of Electrophoretic Systems

Electrophoresis is performed in a large assortment of instruments and methodologies [18], [19]. The first sophisticated electrophoretic apparatus was manufactured by Tiselius in 1937 [20] who developed the theory of moving boundary electrophoresis (MBE). In this early device, the sample is placed within a U-shaped tube that is filled with a buffer electrolyte solution as shown in Figure 1-1. Electrodes are then submerged within each end of the tube in order to generate an electric field. Under the influence of this electric field, sample particles begin to migrate towards the oppositely charged electrode and separate based upon differences in velocity [21], [22].

However, the so-called moving boundaries of the sample components are generally invisible to the human eye and require expensive optical equipment for detection. Further, MBE is a disadvantaged method of electrophoresis because it does not achieve complete separation of molecules; only the fastest and slowest moving components can be distinguished. Due to these limitations, moving boundary techniques are currently only used to measure the electrophoretic mobility of molecules in free solution.

Additional electrophoretic techniques became widely developed in the 1940s and 1950s as electrophoresis was applied to an increasing variety of molecules ranging from large proteins to small inorganic ions. Three other types of electrophoresis emerged during this time known as zone electrophoresis (ZE), isoelectric focusing (IEF) and isotachophoresis (ITP).

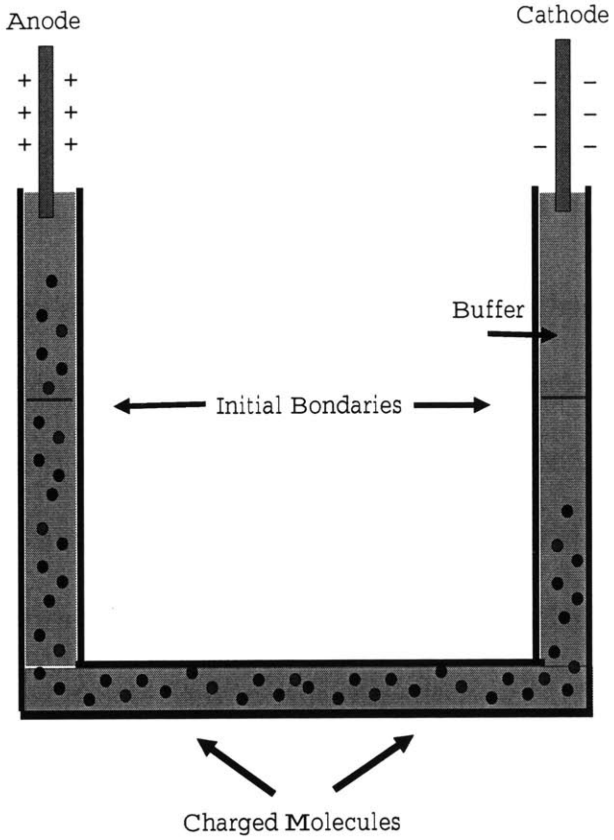

Figure 1-1: Schematic of first electrophoretic device designed by Tiselius in 1937. The machine performs separation of charged molecules via Moving Boundary Electrophoresis (MBE).

Zone Electrophoresis

Zone electrophoresis is currently the most commonly practiced form of electrophoresis in engineering and science applications. This method is similar to moving boundary electrophoresis in that each sample component is allowed to migrate according to its own electrophoretic mobility. The major distinction between the two methods is ZE's use of support media to accomplish total separation of components. The use of a porous media enhances separation because molecules sieve through the matrix pores according to their size. Additionally, the media helps stabilize the boundaries of each component as they migrate through the channel, which tended to mix as a result of thermal gradients or mechanical vibrations in MBE.

Zone electrophoresis uses a homogeneous buffer electrolyte system to establish a constant pH within the channel. As multicomponent samples are drawn through the media, each component separates from its neighbor to form a pure, concentrated zone of molecules that migrates with one velocity. Smaller molecules migrate faster and form concentrated zones the quickest. Consequently, migration distances can be used to measure the electrophoretic mobility of various sample constituents. One potential disadvantage of ZE is its strong dependence on the properties of the sieving matrix [23]. Particular pore sizes are needed for the efficient separation of specific species. This adds a level of complexity to ZE as synthesis of new polymeric media is researched concurrently with methods to improve the electrophoretic system itself.

Isoelectric Focusing

Isoelectric focusing (IEF) was developed in the late 1940's as another type of electrophoresis designed for the fractionation of proteins and peptides [19]. Here, separation is performed in a discontinuous buffer system that utilizes a pH gradient; a low pH near the anode and a high pH near the cathode. The goal of this method is to induce migration of each component to its isoelectric point, where it reaches charge neutrality and ceases to migrate. When the electric field is applied, each component migrates in the direction of decreasing pH and becomes increasingly protonated until it approaches charge neutrality. When all of the sample components reach their respective isoelectric points, no further changes in position or zone width are detected and a steady-state is reached. This indicates the completion of molecular separation via IEF as each zone is then a pure, concentrated region of specific sample components. IEF exhibits very high resolving power as it enables resolution of substances differing in isoelectric points by as little as 0.001 pH units.

The prerequisite for highly resolved and reproducible IEF systems is a stable and continuous pH gradient with constant conductivity and buffer capacity [18], [24]. A pH gradient can be created in an electric field through use of ampholyte buffers in free solution, or use of an external matrix that is polymerized with buffered groups called immobilines. Ampholytes are a complex mixture of molecules whose isoelectric points span the desired pH range. When an electric field is applied, the negatively charged carrier ampholytes migrate towards the anode, while the positively charged ampholytes travel towards the cathode. Each travels with a velocity that is dependent upon the magnitude of its net charge. The ampholytes with the lowest and highest isoelectric points, pI, migrate towards the anode and cathode with the fastest velocities respectively. As remaining ampholytes align themselves in between these two extremes according to their pI, IEF results in a gradually increasing pH gradient from pH 3 to pH 10 [19]. Alternatively, the pH gradient can be incorporated into the supporting media by performing polymerization with buffered immobiline groups able to build a pH gradient within the external matrix used for IEF. Immobilized pH gradients can be exactly calculated in advance and adapted to the separation problem.

The general disadvantage of IEF is its long duration. Since components decelerate significantly as they migrate closer to their isoelectric points, IEF requires several hours to separate a molecular sample. Additionally, IEF requires a constant voltage that can often lead to overheating during the prolonged period of separation.

Isotachophoresis

Isotachophoresis was developed in the early 1950's as an alternative technique for the separation of ampholytes such as proteins and peptides [25]. Separation is performed using two distinct buffer systems where the ionized sample migrates between a leading electrolyte, that migrates with a high mobility, and a terminating ion, that travels with low mobility [18], [26].

When an electric field is applied, the ions start to migrate with the speed of the terminating ion. Since all ions are forced to migrate at the same velocity, the field strength is higher in the area concentrated with ions of lower mobility [19]. Similarly, the field is lower in the region that contains the ions of highest mobility. Different components of the sample are, therefore, separated into concentration zones that are aligned within the channel in order of decreasing electrophoretic mobility [28].

ITP is a unique form of electrophoresis because it accomplishes separation while all solute zones migrate with the same velocity. In addition, constituents of the sample adopt the concentration of the leading electrolyte which allows them to be concentrated by many orders of magnitude.

Pulsed Field Electrophoresis

Types of electrophoresis discussed thus far are performed utilizing a steady field, in which a constant potential gradient is imposed between the cathode and anode. In addition to the methods described, electrophoresis can also be performed using time-dependent fields. For electrophoresis of larger molecules, in particular chromosomes [19], [12] pulsed field electrophoresis is often used. Here, the electric field is applied in a series of timed pulses that forces molecules to change their orientation with changes in the electric field. The three-dimensional structure of the macromolecule is first stretched and then compressed according to its viscoelastic relaxation time, which is strongly molecular weight-dependent [29], [33]. Smaller molecules need less time to reorient themselves than longer molecules, which means separation is accomplished by the length dependent stretching induced by the electric field. Larger molecules between 10 kilobases and 10 megabases can be efficiently separated via pulsed field electrophoresis [27].

1.1.3 Gel Electrophoresis

Separation of DNA is accomplished almost exclusively via zone electrophoresis and can be performed in slab gels [149], [34], capillaries [35], [150], and more recently, within microfabricated channels [5], [36] [37], [38]. As mentioned above in section 1.1.1, DNA molecules exhibit near identical charges in free solution, and therefore require the use of an external matrix to enable separation by molecular size. The migration of charged molecules is impeded by the matrix based upon the ratio of DNA molecular size to the matrix pore size. Any matrix used for DNA separations must remain chemically inert, maintain a consistent pore size, and prevent electro osmotic flow (EOF) during electrophoresis [67]. Zone electrophoresis is widely performed in slab gels comprised of agarose for the separation of large biomolecules greater than 3 kilobases in length. Agarose is the matrix of choice for these separations because the large pore size of the agarose gel facilitates the migration of molecules up to 10 nanometers in diameter [39].

Agarose is made from the organic compound, Agar, which is isolated from the red algae, Rhodophycae [12]. The agarose molecule is comprised of many alternating units of the polysaccharide galactose, and is particularly suited for electrophoresis because it is largely uncharged [14]. Additionally, agarose is an easy matrix to work with because it is a non-hazardous, inexpensive, organic material that does not require cross-linkers for its polymerization [23]. Agarose solutions of low concentrations are fairly rigid and can be used for almost any electrophoretic separation of large molecules.

A solution of agarose is prepared by dissolving the polymer in its powdered form with a solution of boiling water and electrolyte buffer for 2 -3 minutes. The solution is then poured into a gel cast and allowed to cool for approximately 30 minutes until it solidifies to form a slab gel. Solidified gels are typically 5 - 10 mm thick and are placed within a 'submarine' cast as shown in Figure 1-2. The cast isimmersed within a buffer electrolyte, most commonly TBE (Tris/Boric Acid/EDTA). Microliter volumes of biological samples are then placed within the slab gel via small microliter wells that are molded into the agarose solution during its solidification.

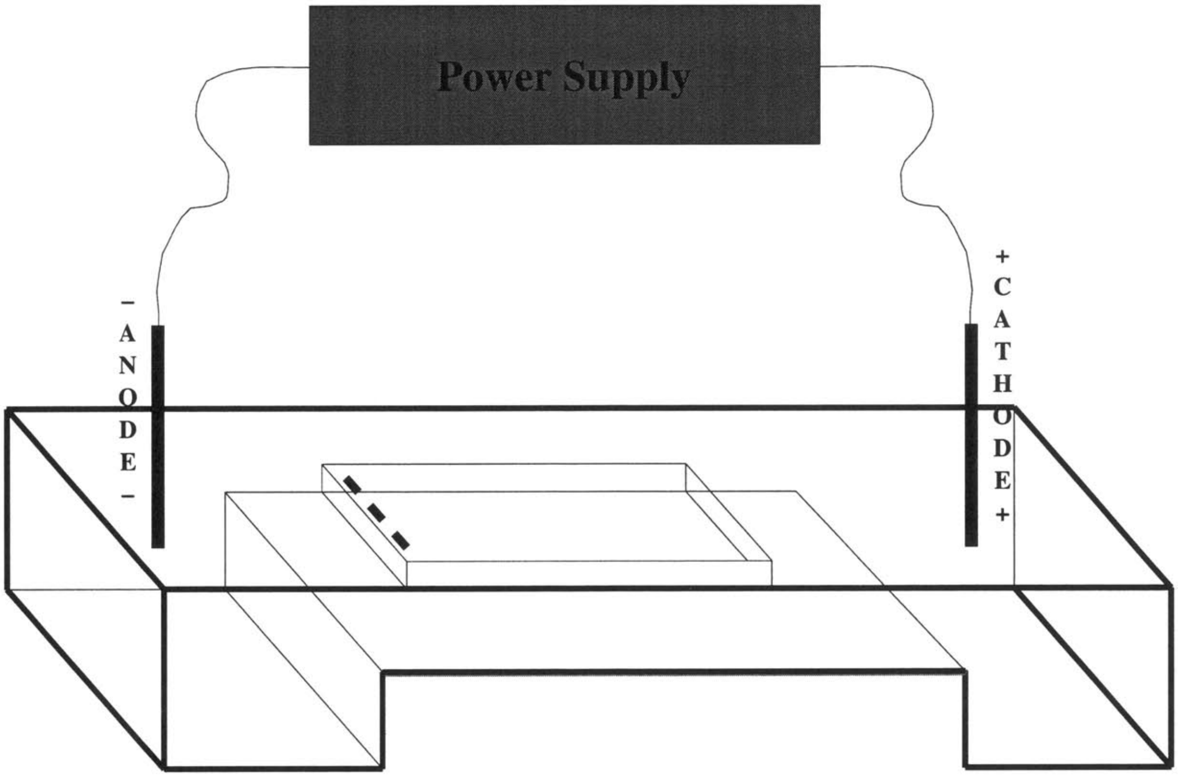

Figure 1-2: Schematic of Gel Electrophoretic device. Solidified Agarose solution is placed within a submarine cast and immersed within an electrolyte buffer solution.

Electrodes on either side of the slab gel apply an electric field that draws negatively charged DNA molecules out of the wells and into the pores of the agarose. Samples are stained with a dying agent, such as ethinium bromide, to enable inspection of the process under ultra-violet (UV) light. The separation of molecules by size is then determined by bright bands that illustrate concentrated zones of molecules with a particular DNA size as shown in Figure 1-3.

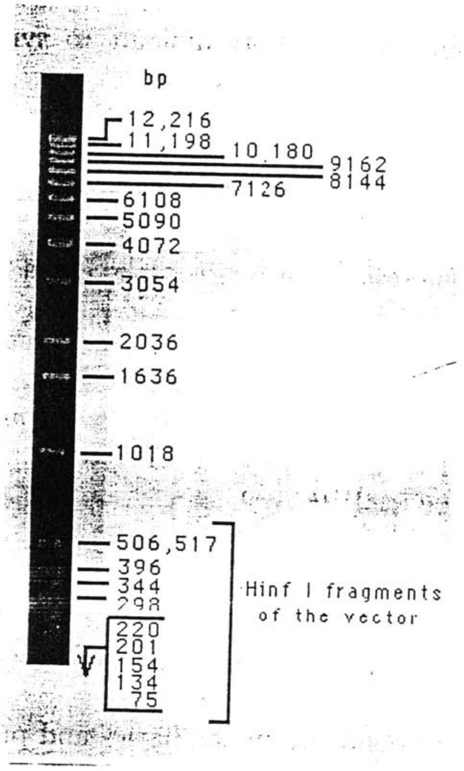

Figure 1-3: Representative results of a biological separation performed using Gel Electrophoresis. Bright bands illustrate concentrated zones of charged molecules of various lengths.

Gel electrophoresis is also performed for the separation of smaller nucleic acids, 25 - 2000 bases in length, using solutions of synthetic polyacrylamide polymers. Here, additional preparation of the slab gel is required although the test protocols remain the same. Polyacrylamide solutions used for slab gel electrophoresis are typically crosslinked polymers synthesized using acrylamide monomers that are covalently linked by crosslinking agents such as EDA and DATD, ethylenediacrylate and diallyltartardiamide, respectively [40]. Unlike agarose solutions, polyacrylamide solutions are more difficult to synthesize because they require additives for polymerization such as ammonium persulfate and tetramethylenediamine (TEMED). Although polyacrylamide is synthetic and more chemically hazardous than agarose, it is widely used for electrophoresis because of its excellent sieving properties for smaller molecules [41], [43], [44].

1.1.4 Capillary Electrophoresis

Slab gel electrophoresis is still widely-used today for the simple separation of larger biomolecules. However, research from Jorgenson and Lukacs [46], [47] in the early 1980s highlighted the advantages of conducting electrophoresis in capillaries and popularized the use of Capillary Electrophoresis (CE). CE operates on the same principles as gel electrophoresis but utilizes a narrow bore capillary to create an electrophoretic path rather than a wide tray. CE is often compared to the older separation technique of liquid chromatography because the methods operate on complementing principles [48], [49].

In High Performance Liquid Chromatography (HPLC), components of a sample are dissolved into a solvent and forced to flow through a chromatographic column under high pressure [14], [25] as shown in Figure 1-4. The column is filled with an immobile packing material, often called the stationary phase, which resolves sample constituents dependent upon their interactions with the packing. Separations can be performed via adsorption-desorption mechanisms, ionic exchange, or size-exclusion. Capillary electrophoresis is most similar to size-exclusion chromatography (SEC) because both channels are filled with a packing material synthesized with specific pore sizes. Molecules of the sample are screened, or filtered, by the packing media according to their solvated molecular size.

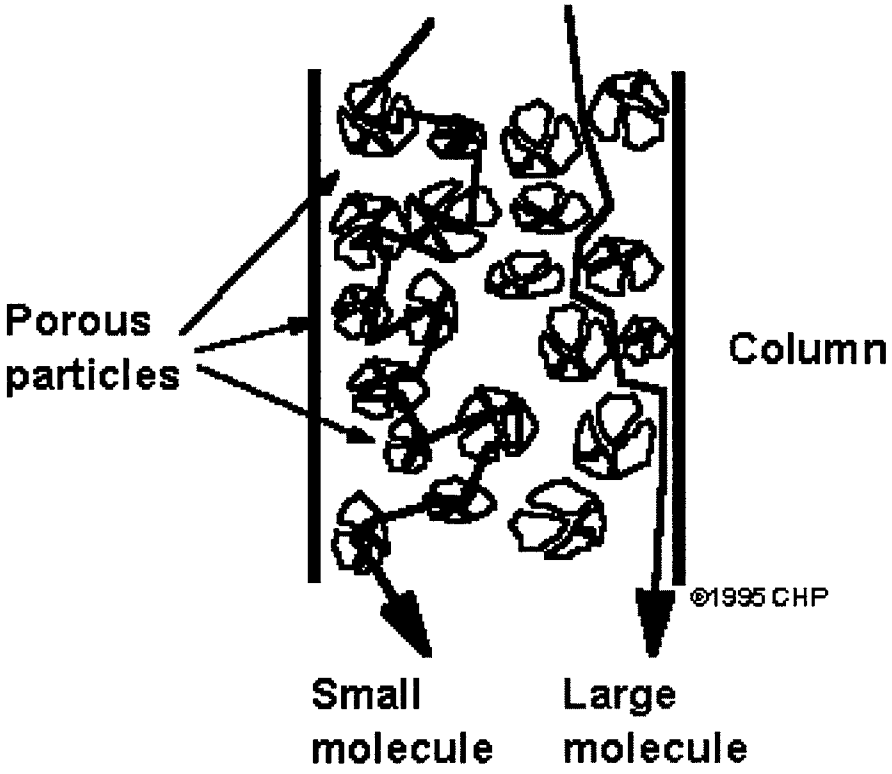

Figure 1-4: Schematic of a High Performance Liquid Chromatography system.

In HPLC, smaller molecules penetrate inside the pores of the packing material and elute more slowly, while molecules too large to migrate through the pores wash rapidly through the column. Capillary electrophoresis uses the external media in an opposite way as pores do not retain smaller molecules but rather impede migration of larger molecules. In CE, smaller molecules migrate through the pores of the matrix by diffusion very rapidly and separate first, while larger molecules reptate within these pores more slowly and separate in order of ascending molecular size.

Capillary electrophoresis frequently utilizes polyacrylamide solutions as the external matrix during separations. Although CE is sometimes performed with crosslinked solutions [149], [158], [49] more recent applications utilize uncrosslinked polyacrylamide solutions. These solutions do not incorporate EDA or TEMED and their entanglements remain loose rather than rigidly fixed with a crosslinker agent. Uncrosslinked solutions are more commonly used for CE due in large part to numerous polymer experiments [66], [144] which indicated DNA molecules interact strongly with the monomers of the solution itself. These interactions induce better separation by molecular size because they increase the frictional losses experienced by longer DNA molecules during migration.

Uncrosslinked solutions of linear polyacrylamide (LPA) are formed when powdered acrylamide is dissolved within electrolyte buffers and left to mix via slow mechanical stirring for several days. No crosslinking agents are added, and the solution is then inserted into the capillary via a syringe, or pump, after an adhesive layer has been applied to the capillary wall. This additional adhesive layer is required because it prevents the migration of the uncrosslinked LPA during electrophoresis as a result of electro osmotic flow (EOF) [54].

In the operation of a CE system, the capillary is filled with a polymer solution and its ends are dipped into reservoirs filled with an electrolyte [150]. As seen in Figure 1-5, platinum electrodes are also inserted within the reservoirs to generate an electric field along the capillary. A small volume of fluorescently-labeled sample is hydrodynamically injected into one end of the capillary, via a pump or vacuum, before the capillary is inserted within the reservoirs. The sample is then drawn towards the anode by a potential gradient imposed via the electrodes. Molecules migrate through the capillary by navigating within the pores of the polymer matrix. Separation is accomplished as smaller molecules migrate more rapidly along the capillary length and separate from the populations of slower-moving, large molecules. Detection of fluorescent sample molecules is established via an ultra-violet absorbance detector that is located at the opposite end of the capillary. Elution time of the labeled molecules is then recorded by the detector and displayed as a function of time in an electropherogram.

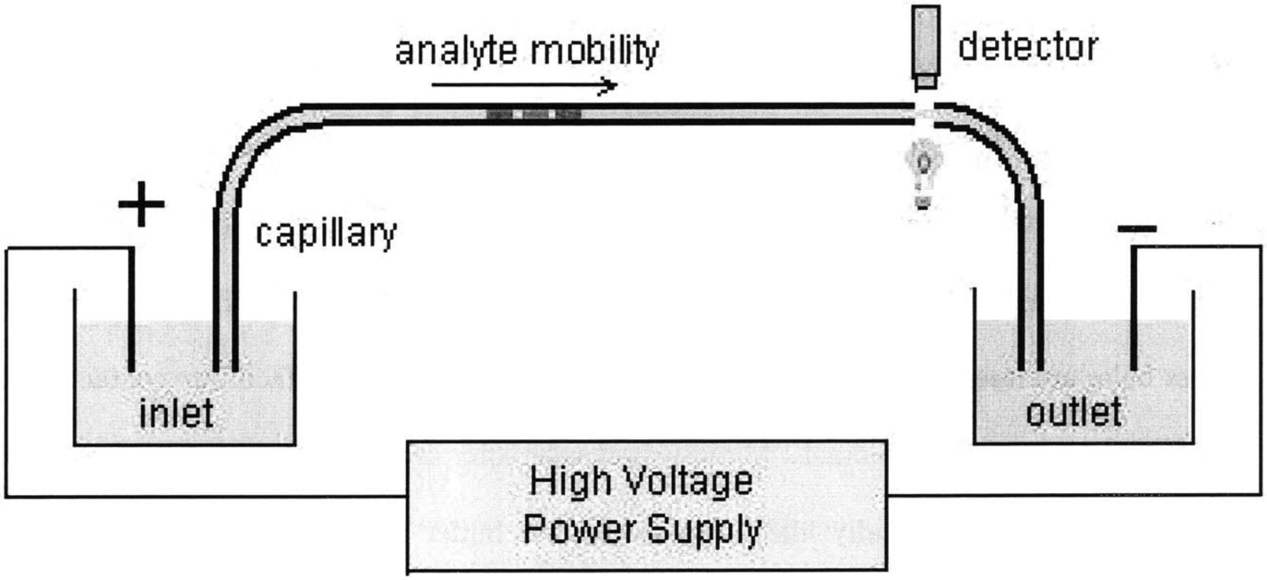

Figure 1-5: Typical Single-Lane Capillary Electrophoresis system.

One major advantage of CE is the efficient heat dissipation provided by capillary walls due to the high surface-area to volume ratio. As a result, voltages as high as 40 kV can be used to achieve rapid, more efficient separations of smaller biomolecules [51], [52], [53]. In addition, separations performed in capillaries offer the possibility of automated analytical equipment, rapid analysis times and on-line detection of separated DNA. In fact, several commercial instruments now incorporate 96 capillaries for high throughput separations of DNA molecules [57], [55], [56]. However, in the early 1990's a new manner in which to conduct zone electrophoresis emerged when researchers incorporated micromanufacturing techniques to develop microdevices for separation of DNA.

1.1.5 Microdevice Electrophoresis

Electrophoresis is now rapidly evolving towards the use of microfabricated channels for both single-lane and high throughput multi-lane separations of DNA [5], [58], [59], [60]. Electrophoresis performed in microdevices utilizes very similar protocols to those followed in CE, with the primary differences exhibited in the electrophoretic channels themselves. Whereas the capillary system has two reservoirs and only one circular channel, microdevices utilize four reservoirs and three distinct rectangular channel sections as shown in Figure 1-6. Small access holes are laser-drilled into the ends of each channel in order to facilitate contact with the polymer within the channel. Miniaturized reservoirs are placed atop of each channel aperture and are individually filled with electrolyte buffer and DNA solutions to enable electrophoresis.

A conventional micro device is comprised of one long channel that is intersected by two smaller perpendicular channels. If these channels intersect at the same point, the device is said to have a 'simple cross' configuration, whereas if the smaller channels intersect at two distinct points, the device exhibits a 'double-T' configuration. These configurations are so-called because their profiles look like they were made with a cross, or by alternating the letter 'T', respectively [61].

The cathode is placed within the reservoir furthest away from the channel intersection(s), while the anode is placed within the reservoir closest to the intersection(s). The smaller channel that intersects closest to the cathode is called the sample channel, while the channel that intersects closest to the anode is called the waste channel. In the double-T configuration, the distance between these channels is called the offset channel. The offset channel is obviously non-existent in the simple cross configuration, and, therefore, either perpendicular channel can be designated as sample or waste. However, the reservoirs at the end of the sample and waste channels must be filled with the appropriate sample and electrolyte buffer solutions, respectively.

The separation channel of a microdevice is defined by the distance in between the anode reservoir and the waste channel. The oposite distance in between the sample channel and the cathode reservoir is then termed the channel tail. Lastly, the portion of the device in between the sample and waste reservoirs is called the cross-injector. The cross-injector of a microdevice with a simple cross configuration is comprised of only the sample and waste channels. In contrast, the cross-injector of a device with a double-T configuration includes the offset length in between the two channels. The cross-injector of a microdevice offers a very specific advantage over conventional capillary or slab gel electrophoretic systems. Namely, the cross-injector enables more precise sample loading of DNA molecules as a specified amount of sample can be injected into the separation channel via specific design of the offset geometry and the applied voltage profile. In addition, cross-injectors eliminate the

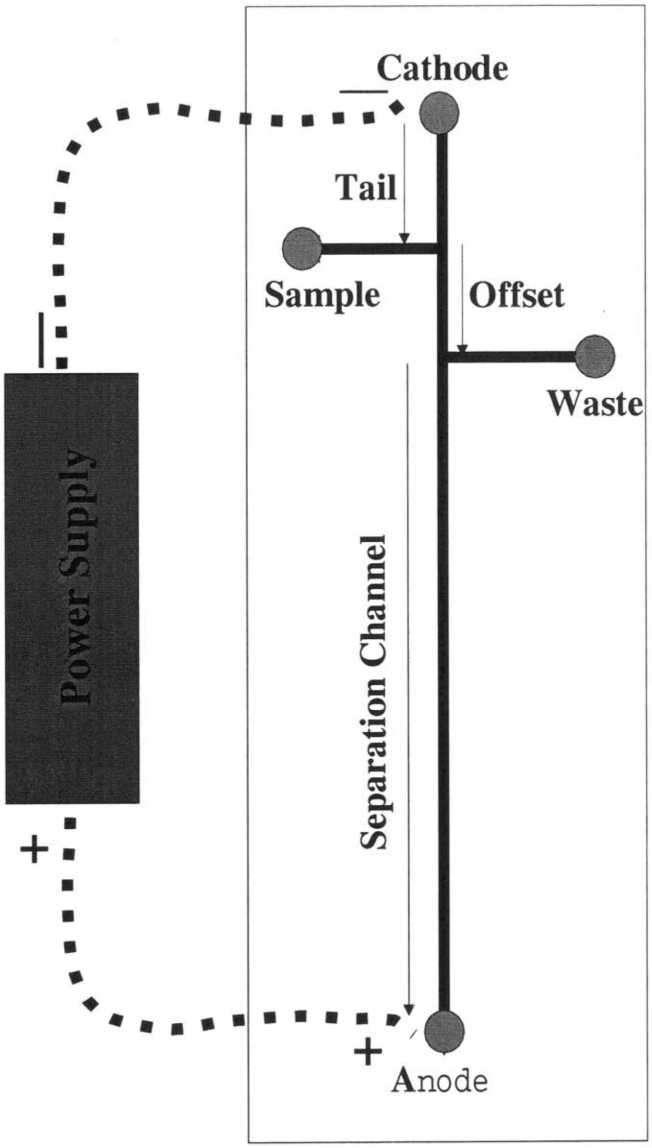

Figure 1-6: Schematic of a conventional microdevice with a double-T configuration. Cathode, Anode, Sample, and Waste reservoirs are identified as are channel tail, cross-injector and separation channels.

need to dip the electrophoretic channel into electrolyte reservoirs, as well as hydrodynamic injection, which helps to streamline the entire electrophoretic process.

Using a cross-injector for sample-loading, DNA molecules are introduced into the separation channel in a two-part procedure. First, a loading voltage forces DNA molecules to migrate from the sample reservoir to the waste reservoir via the cross-injector channels. Second, the loading voltage is turned off, after a pre-specified time, and a separate running voltage is imposed between the cathode and anode. The running voltage causes the migration of DNA molecules out of the injector and into the separation channel, thereby initiating separation. A UV detector is located at the end of the separation channel and generates an electrophoregram just as in CE [6].

Microdevice electrophoresis is an exponentially growing field because its unique sample loading, small separation distances and excellent thermal characteristics allows analysis close to theoretical performance limits. In addition, microfabricated channels result in improved operational robustness, reduced reagent consumption and less human interference through process integration [143].

1.1.6 Electrophoretic Analysis

The success of any electrophoretic separation, regardless of the method used, largely depends upon the peak widths and inter-peak spacing measured from the resulting electrophoregram [10]. The separation capacity of a system is described by resolution measurements denoted R_L, that incorporate both peak width and spacing [63], [64]:

$$R_L = \sqrt{2ln2}\frac{\Delta t_R}{(W_{h1} + W_{h2})} \tag{1.1}$$

where t_R is the retention time of an individual peak in seconds, and W_{h1} and W_{h2} represent the full peak widths at half maximum between 2 successive peaks, also measured in seconds. Resolution values increase when separations produce concentrated zones of DNA with uniform populations because zones are less broadened and are easily distinguished from the populations of their neighbors on an electrophoregram. One other very important quality of an electrophoretic separation is its selectivity. Selectivity refers to the level in which the electrophoretic separation can determine particular analytes in a complex mixture without interference from neighboring components. Selectivity is incorporated in the resolution measurements via the residence time.

The efficiency of an electrophoretic separation is directly proportional to a parameter called the theoretical plate number, N_T. This is defined in terms of the length of the separation channel and the total variance of the sample zone.

$$N_T = \frac{L^2}{\sigma_T^2} \tag{1.2}$$

where L denotes the length of the separation channel and ${\sigma_T}^2$ represents the variance of a Gaussian peak including all dissipative phenomena such as diffusion and dispersion. The variance is often used to define the broadening exhibited by a Gaussian zone. Zone broadening is affected by numerous parameters such as temperature, diffusion, and electro osmotic flow (EOF). The specific components of zone broadening are reviewed in an excellent text by

Grossman et. al [10]. Here, the authors develop an expression that incorporates the factors which primarily affect zone broadening.

$$\sigma_T = \sqrt{\sigma_D^2 + \sigma_{\Delta T}^2 + \sigma_L^2} \tag{1.3}$$

where σ represents the increase in the Gaussian width of a DNA population due to diffusion effects, D, temperature, T,and finite injection volume, L, respectively. As seen from Equation 1.2, the theoretical plate number, and hence the efficiency of a sequencing separation, is improved by protocols that reduce zone broadening.

1.2 Electrophoretic Theory

The dynamics of molecular motion during electrophoresis is rather complex. First, one must consider the morphology of the charged molecule itself, which is largely dependent upon the other ions in solution, pH, temperature, and the applied field [74] [65]. Next, the method of migration must be considered, which is a function of molecular size, the external matrix used, and the applied field [66]. In addition, conservation laws [1], [67] must be upheld and interactions between DNA and the external matrix must be considered [68], [70], [69]. Although these interrelated processes seem overwhelming, they are constrained by a general set of equations that are outlined in this section. These include balance laws that express the conservation of mass, energy, and ionic species, as well as electrostatic relations that describe the interrelation between charge and potential.

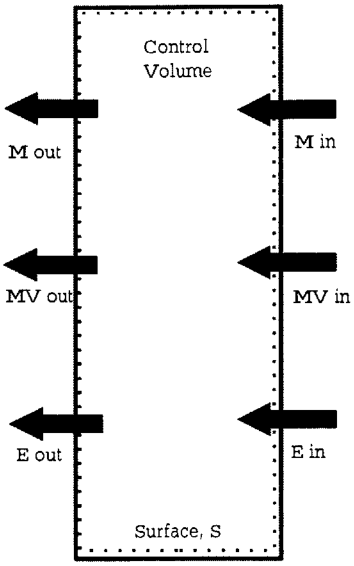

Figure 1-7: Schematic of a Control Volume taken within an electrophoretic system.

1.2.1 Conservation Laws

The motion of any fluidic system is described by conservation of mass, momentum, and energy. To explain these relations, it is helpful to define a control volume, V, around a small section of an electrophoretic channel as shown in Figure 1-7. This element is defined by a surface, S, and is constrained by permeable boundaries that permit fluid flow in and out of the control volume.

First, the total mass within the control volume is equal to the rate at which fluid particles cross the boundaries of the control volume plus their rate of accumulation within the volume. This can be expressed mathematically as:

$$\left[\frac{\partial \rho}{\partial t} + (\nabla \cdot \rho \mathbf{u})\right] = 0 \tag{1.4}$$

Where ρ is fluid density, t is time, and u is velocity. This equation expresses conservation of mass and is often simplified for incompressible fluids (ρ = constant) as:

Continuity Equation

$$(\nabla \cdot \mathbf{u}) = \mathbf{0} \tag{1.5}$$

Next, using the same control volume element in Figure 1-7, the transfer of momentum within the element must be similarly conserved. The rate of momentum transferred across the surfaces of the control volume via bulk flow, molecular motions and interactions, is balanced by the force exerted on the fluid by external forces, such as gravity, and the rate of accumulation within the volume. The relationship is often called the equation of motion and is described mathematically as:

Equation of Motion

$$\frac{\partial}{\partial t}(\rho \mathbf{u}) = -[\nabla \cdot \rho \mathbf{u}\mathbf{u}] - [\nabla \cdot \mathbf{\Pi}] + \rho \mathbf{g} \tag{1.6}$$

where $\mathbf{u}$ is velocity, ρ is density, and $\mathbf{\Pi}$ is the momentum flux tensor or stress tensor [159].

Returning to the designated control volume element in Figure 1-7, as the mass and momentum of fluid particles within the element are conserved, their energy is also similarly conserved. The conservation of energy within the control volume is obtained via the first law of thermodynamics. According to the first law, the rate of increase in kinetic and internal energies of a system must equal the rate at which energy is added to the system, minus the rate at which the fluid inside of the control volume does work against surrounding flow and external forces [72]. Mathematically this equates to:

Conservation of Energy

$$\frac{\partial}{\partial t}(\rho U) = -(\nabla \cdot \rho U \mathbf{u}) - (\nabla \cdot \mathbf{q}) - (\mathbf{\Pi} : \nabla \mathbf{u}) \tag{1.7}$$

Where ρ is density, U is internal energy, $\mathbf{u}$ is velocity, $\mathbf{q}$ is heat, and $\mathbf{\Pi}$ is the stress tensor.

With a specified consituitive relation and boundary conditions for a specific fluidic system, Equations 1.5, 1.6 and 1.7 comprise the set of basic equations that are valid for any generalized fluid flow. However, for the specific study of electrophoresis, the conservation of chemical species and charge are additionally required. The local rate of ion accumulation within the control volume is balanced by the rate of ion transfer to the volume plus the rate of ion generation within the volume due to chemical reactions [67]. For a general species, i, chemical conservation is mathematically represented as:

Conservation of Chemical Species

$$\frac{\partial}{\partial t}(n_i) = R_i - \nabla \cdot \mathbf{f}_\mathrm{i} \tag{1.8}$$

Where n_i is the concentration of species i, R_i is the rate of generation of species i by chemical reactions within the control volume, and $\mathbf{f}_\mathrm{i}$ is the flux vector. Note that the rate of generation is neglected for electrophoretic systems and the flux vector is defined by diffusion, electromigration and convection. Additionally, the flux components can be linearly superposed for dilute systems to obtain:

$$f_i = n_i u + e z_i \mu_i n_i E - \mu_i k_B T(\nabla n_i) \tag{1.9}$$

Where n_i is the concentration of species i, $\mathbf{u}$ is velocity, e is the fundamental unit of electric charge of value $1.6 \times 10^{-19}C$, z_i is the valency of the i'th species, μ_i is the mobility of the i'th species, $\mathbf{E}$ is the applied electric field, k_B is the Boltzmann constant of value $1.38 \times 10^{-23} J/K$, and T is the absolute temperature in Kelvin.

The last major conservation relation needed for the analysis of electrophoresis is conservation of charge. The ionic charge of any molecule can be positive, negative or identically zero dependent upon its molecular composition. Molecules of opposite charge attract, while molecules of like charge are repelled. Electric charge is a conserved quantity such that the total charge before and after any reaction remains the same.

charge, respectively.

Ionic charge is particularly important in electrophoresis because molecules of a sample are attracted and repelled by molecules of different and similar charges, respectively, during migration. Further, the electric force exhibited by one molecule on another is independent of particle mass and depends only upon its electric charge. For small charged bodies, the familiar Coulomb's law [76] describes the force exerted by one point charge on another.

$$F = \frac{1}{4\pi\epsilon_0}\frac{qq'}{r^2} \tag{1.10}$$

Where ϵ_0 is the permittivity constant, $8.85 \times 10^{-12} C^2(N \cdot m^2)$, q and q' are particle charges in units of Coulombs, C, and r is the distance between them. Note that Equation 1.10 is only valid for a pair of small charged bodies whose sizes are much less than the distance between them, i.e. point charges. This equation strongly resembles Newton's Law for the gravitational force, $\mathbf{g}$, which describes the gravitational force exerted by one molecule of mass, m_1 on another of mass m_2 [76]. However, the relative strength of the attractive electric force between two charged molecules as its value between an electron and proton is $\sim 10^{40}$ times stronger than the gravitational force between them. Hence, electric field considerations are extremely important in many fluidic systems, which makes it important to understand their influences on the migration of charged species.

1.2.2 Electrokinetics

All phenomena that incorporate externally applied fields can be discussed in terms of the fundamental laws of electricity and magnetism derived by James Maxwell in the late 18th century. Maxwell's equations are particularly powerful because they demonstrate that only four fundamental laws are needed to completely describe the behavior of electric and magnetic fields in a system. These four laws are Gauss' law of electricity, Gauss' law of magnetism, Faraday's law of induction, and the modified Maxwell-Ampere law of electro motive force. Although Maxwell did not develop these individual equations himself, these four taken as a whole are called Maxwell's Laws because it was he who recognized that they couple and unify the dynamic interaction between electric and magnetic fields [2].

Gauss' law of electricity states that the electric flux through an enclosed, charged surface is directly proportional to the attraction and repulsion between its stationary charges. Conversely, Gauss' law of magnetism affirms that the magnetic flux through the same enclosed surface is identically zero; or stated more conventionally, there exist no magnetic dipoles. Faraday's law of induction illustrates that an electric field is induced by a changing magnetic field and the Maxwell-Ampere law establishes that a magnetic field is similarly induced by a changing electric field. The equations of Maxwell's laws are expressed mathematically below.

Gauss' Law of Electricity

$$\int E \cdot dS = \frac{Q}{\epsilon_0} \tag{1.11}$$

Gauss' Law for Magnetism

$$\int B \cdot dS = 0 \tag{1.12}$$

Faraday's Law of Induction

$$\int E \cdot dl = -\frac{d\Psi_B}{dt} \tag{1.13}$$

Maxwell-Ampere Law

$$\int B \cdot dl = \mu_0 I + \mu_0 \epsilon_0 \frac{d\Psi_E}{dt} \tag{1.14}$$

where E is the applied electric field in V/cm, S is a surface, Q is charge in Coulombs, and ϵ_0 is the electric permittivity of a material measured in $C^2/(N \cdot m^2)$. B is the magnetic field measured in Tesla, l is the length of the path, and Ψ_B is the magnetic flux and Ψ_E is the electric flux in volts. Lastly, μ_0 is the permeability constant expressed in units of $V \cdot s/A \cdot m$ and I is current in Amperes, A.

Although Maxwell's laws are the basis of electromagnetic theory, the effects of any magnetic fields, imposed or otherwise induced, are negligible for the specific discussion of electrophoresis. In this case, the modified Maxwell's relations for electrostatics well describe the interplay between charged molecules in solution and applied electric fields. For this discussion, only two specific electrostatic relations are needed which are obtained by applying the Divergence theorem to Equation 1.11 and Stokes theorem to Equation 1.13.

$$\epsilon_0 \nabla E = \rho^{(f)} \tag{1.15}$$

$$\nabla \times E = 0 \tag{1.16}$$

where ϵ_0 is the permittivity of a vacuum, $8.854 \times 10^{-12} C^2/Nm^2$, E is the applied electric field measured in V/cm, and $\rho^{(f)}$ is the free charge density. For electrophoresis, the new parameter $\rho^{(f)}$ is equal to the local excess of ionic charge arising from N ionic species within an electrolyte solution. It is described more accurately by its following electro chemical definition [67], [78].

$$\rho^{(f)} = \Sigma e z^i n^i \tag{1.17}$$

where e is fundamental charge equal to $1.6 \times 10^{-19} C$, z^i is the valency of the i'th ion, and n^i is the concentration of the i'th ion in the electrolyte solution. The free electric energy, $\rho^{(f)}$, enables a description of Gauss' law that is more applicable to electrophoresis using the divergence theorem [77]:

$$\int E \cdot dS = \frac{1}{\epsilon_0} \int \rho^{(f)} dV = \frac{Q}{\epsilon_0} \tag{1.18}$$

Equation 1.16 indicates the electric field is a conservative field, meaning it can be represented in terms of a potential function, Φ.

$$E = -\nabla\Phi \tag{1.19}$$

The electrostatic potential, Φ, must still satisfy Equation 1.15. and via substitution we obtain the more specific Maxwell law of electrostatics.

$$\epsilon_0 \nabla^2 \Phi = -\rho^{(f)} \tag{1.20}$$

In order to obtain an expression for the potential field, Φ, the next task is to describe the concentration of ions that produce the free electrical charge density, $\rho^{(f)}$.

1.2.3 Migration of Polyelectrolytes

DNA molecules in solution are polyelectrolytes, meaning they carry multiple charges during migration. During electrophoresis, DNA are surrounded by a high number of smaller counter ions from the electrolyte buffer that move in turn with the macromolecule during electrophoretic migration [74], [80]. The distribution of ions within the solution surrounding the macromolecule is governed by the balance of electrostatic and Brownian forces. Assuming the ions far away from a charged macromolecule are in equilibrium, the net force acting upon them must vanish. In this case, the driving force is the gradient of the electro chemical potential [1], [14] obtained from Equation 1.15 and Equation 1.17.

$$k_B T \nabla ln(n^i) + e z^i \nabla(\Phi) = 0 \tag{1.21}$$

where k_B is Boltzmann's constant, T is temperature, n^i is the concentration of the i'th ion,

e is fundamental charge equal to $1.6 \times 10^{-19}C$, and z^i is the valency of the i'th ion. The solution to Equation 1.21 indicates the ions follow the Boltzmann distribution:

$$n^i = n^i_b \exp\left(\frac{-ez^i\Phi}{kT}\right) \tag{1.22}$$

Substitution of Equation 1.22 into Equation 1.17 then reveals that the electrostatic potential in ionic solutions, Φ, is described by the familiar Poisson-Boltzmann distribution.

$$\epsilon\epsilon_0\nabla^2(\Phi) = -e\Sigma z^i n^i_b \exp\left[\frac{-ez^i\Phi}{k_B T}\right] \tag{1.23}$$

Where ϵ_0 is the permittivity of a vacuum of value $8.855 \times 10^{-12}C^2/Nm^2$, Φ is the electric potential in units of volts, e is fundamental charge of value $1.6 \times 10^{-19}C$, z^i is the valency of the i'th ion, n is the concentration of the i'th ion, k_B is Boltzmann's constant of value $1.38 \times 10^{-23}J/K$, and T is absolute temperature in Kelvin.

The solution to Equation 1.23 describes the distribution of electrolyte ions within a given potential field, Φ, and is often called the Gouy-Chapman theory [79]. In the Gouy-Chapman model, the random thermal motion of ions near the macromolecule results in a diffuse layer of charge that surrounds the molecule. Within this diffuse layer, the concentration of counter ions is greatest near the surface of the macromolecule and decreases exponentially within the bulk electrolyte where a homogeneous distribution of ions is formed. This layer of ions travels with the DNA molecule and is called the electric double layer. The innermost layer of ions remain immobile with respect to the macromolecule while the outer layer consists of diffusive ions that migrate with velocities different from than the macromolecule. Since electrophoretic migration is most affected by the diffuse layer, its thickness is frequently measured by a parameter called the Debye length, λ_D:

$$\lambda_D = {\frac{\epsilon\epsilon_0 k_B T}{e^2 \Sigma z_i^2 C_i}}^{-1/2} \tag{1.24}$$

where z_i and C_i are the valency and bulk concentration of ions of species, i, respectively. The Debye length is measured in nanometers and is important to the discussion of electrophoretic migration because it often acts to reduce the velocity of the molecule [79], [1], [81]. The external field applied during electrophoresis exerts a force on both the macromolecule and surrounding ions. Due to the excess counter charge, the cloud of ions surrounding a macromolecule is dragged in a direction opposite that of the molecule, exerting hydrodynamic drag and impeding macromolecular motion. This effect is called electrophoretic retardation and it is one of the reasons why analytical expressions of electrophoretic mobilities are often higher than measured values. The counter motion of the electric double layer also causes electrophoretic relaxation which sets up a counter electromagnetic force that reduces the electrophoretic mobility of the molecule. This is caused when the center of the electric double layer is not concentric with the center of the molecule. The last effect of the electric double layer is surface conductance. Due to its excess counter ion concentration, the ion cloud increases the value of the local conductivity surrounding the molecule resulting in lower voltage gradients and hence, slower mobilities.

1.2.4 Simplified Solutions

Although a complete analytical solution for the migration of a polyelectrolyte is very rigorous, simplified solutions are obtained for the limits of small and large Debye lengths. In the limit where the Debye layer is large, meaning the Debye thickness, λ_D, is much greater than the radius of the molecule, R_g, the electric force and viscous drag acting on the molecule can be found independently. In this analysis, the electrical body force is balanced by the viscous drag according to Stokes' law and an expression for the electrophoretic mobility is obtained.

$$\mu = \frac{v}{E} = \frac{Q}{6\pi\eta R_g} \tag{1.25}$$

Where η is the viscosity of the polymeric sieving matrix, and Q is molecular charge. In the opposite limit, where the Debye layer is thin compared with the particle size, shear occurs along the electric double layer and the complete equation of motion must be solved. The electric potential present at the shear plane is called the zeta potential, ζ. A solution in this limit was first proposed by Smoluchowski [1] in 1903 who illustrated that the resulting velocity is independent of molecular size and shape.

$$\mu = \frac{\epsilon\epsilon_0\zeta}{\eta} \tag{1.26}$$

where ζ represents the zeta potential of the macromolecular surface [1].

Note, however, that Smoluchowski's equation actually describes the motion of the surface of a macromolecule with respect to a surrounding fluid that is at rest. It can, therefore, be equivalently applied to the motion of electrolyte ions near an immobile charged surface, which describes the theory of electro-osmotic flow.

Electro-osmotic flow is an important aspect of electrophoretic systems because it generated when the pH level of the electrolyte buffer stimulates the dissociation of silicon-oxygen linkages present in the channel walls [81], [49]. The dissociation creates a negatively charged surface near the wall that attracts a layer of positive ions from the bulk electrolyte solution. When the running voltage is applied, the migration of these positively charged ions towards the cathode creates a pressure gradient that counteracts the flow of DNA molecules towards the anode. This counter motion is called electro-osmotic flow, or EOF, and is described by Smoluchowski's result shown in Equation 1.26.

Although both of these analyses bring insight into the dynamics of macromolecules under applied fields, the true effects of the electric double layer on velocity, depend upon the method of migration used during electrophoresis. These mechanisms are discussed in the fourth section of this chapter, which specifically describes macromolecular properties and dynamics. However, before discussing the specifics of electromigration, it is important to describe and understand the properties of the microdevices that are used to facilitate electrophoresis.

1.3 BioMEMS Devices

Microdevices used for DNA separations can exhibit many different types of channel designs. The simple cross and double-T configurations were mentioned earlier, but in addition there exist designs that utilize multiple sample and waste channels [61], as well as designs which utilize the same sample and waste channels for multiple electrophoretic lanes [82], [83]. However, regardless of the specificities of the channel, all microfabricated devices must accomplish the same task, separation of charged molecules.

1.3.1 Properties

First and foremost, devices must be made of materials that are rigid and durable. The material must be able to withstand elevated operating temperatures during operation and cannot react with the chemicals needed for separations. Channels are generally 40 μm by 90 μm in cross section and can have different depth characteristics dependent upon the method of etching used. Further, from an optics standpoint, devices must not scatter light so that fluorescently labeled sample can be easily identified by a UV absorbance detector.

1.3.2 Manufacture

Conventional MEMS devices are manufactured using 2 pieces of glass, of either fused silica or boron silicate. The pattern of interest is transposed onto one of the substrates using photolithography, which is subsequently bonded with the blank substrate to form an enclosed channel. The full manufacture involves photolithography, chemical etching, excimer drilling, chemical treatment of the surface, and high temperature bonding.

Photolithography

The first stage in the manufacturing process is the development of the photomask. Photomasks are the equivalent of film negatives because they are reproduceable copies of the design geometry. Photomasks are generally made of soda lime, which is a glass material whose salt composition slightly affects the passage of light through it. The thickness of the mask must be very uniform as even slight irregularities can affect the quality of the finished mask. The glass is coated with an extremely uniform and thin layer of chrome, or iron oxide, which is then covered by a layer of photo-sensitive polymer called photoresist. The pattern of interest is then etched onto the mask to make a permanent cast of the design.

Photomasks can be positive or negative depending upon the type of resist used. A positive mask represents the geometry of the desired pattern, including line size dimensions and lengths, with opaque material, and keeps surrounding areas translucent. Conversely, a negative mask uses opaque material for the areas surrounding the design and translucent material for the design itself. When light is transmitted through the mask, only regions with non-opaque material allow the light to pass.

Once the desired pattern is captured with a photomask, the manufacturing process can begin. The substrate is also coated with a thin, uniform layer of chrome, followed by a thin uniform layer of photoresist via traditional sputtering equipment. Unlike the high sensitivity required for the photomask, layers of chrome and resist ~ 50 μm thick are adequate. The photoresist is a photosensitive polymer that modifies its material properties when irradiated with strong ultra-violet light. Two types of photoresist can be used for processing, termed positive and negative to match the negative and positive polarity of the photomask, respectively. UV light incident upon the positive resist weakens the polymer, while UV that illuminates negative resist strengthens the polymer. Note, the conventional manufacture of Bio MEMS devices generally utilizes positive resist and negative photomasks and, hence, this discussion will focus on that process.

The desired pattern on the photomask is transposed onto the substrate via photolithography as seen in Figure 1-8. Using an ultra-violet lamp, UV light is radiated through a positive mask onto the surface of the substrate for a 60- to 90-second duration. UV light makes the exposed resist very soft and easily dissolved by like chemical compounds. Following UV exposure, the substrate is immersed within a developer solution that removes the regions of weakened resist. Using a positive resist and negative mask, only those areas of the substrate illuminated by the UV light are chemically removed by the photodeveloper. The remaining areas of resist, unexposed to UV light, remain chemically affixed to the layer of chrome, which is in turn affixed to the substrate surface.

After the photoresist is removed, there remains a chrome layer above the pattern of interest. In order to remove this layer, substrates are immersed within a different solution of chrome etch that chemically removes the exposed chrome. Substrates are subsequently well rinsed with water and can then display the transposed pattern. Although microscopes are sometimes preferred for magnified inspection, the success of the photolithography is easily detected by eye after the chrome has been removed.

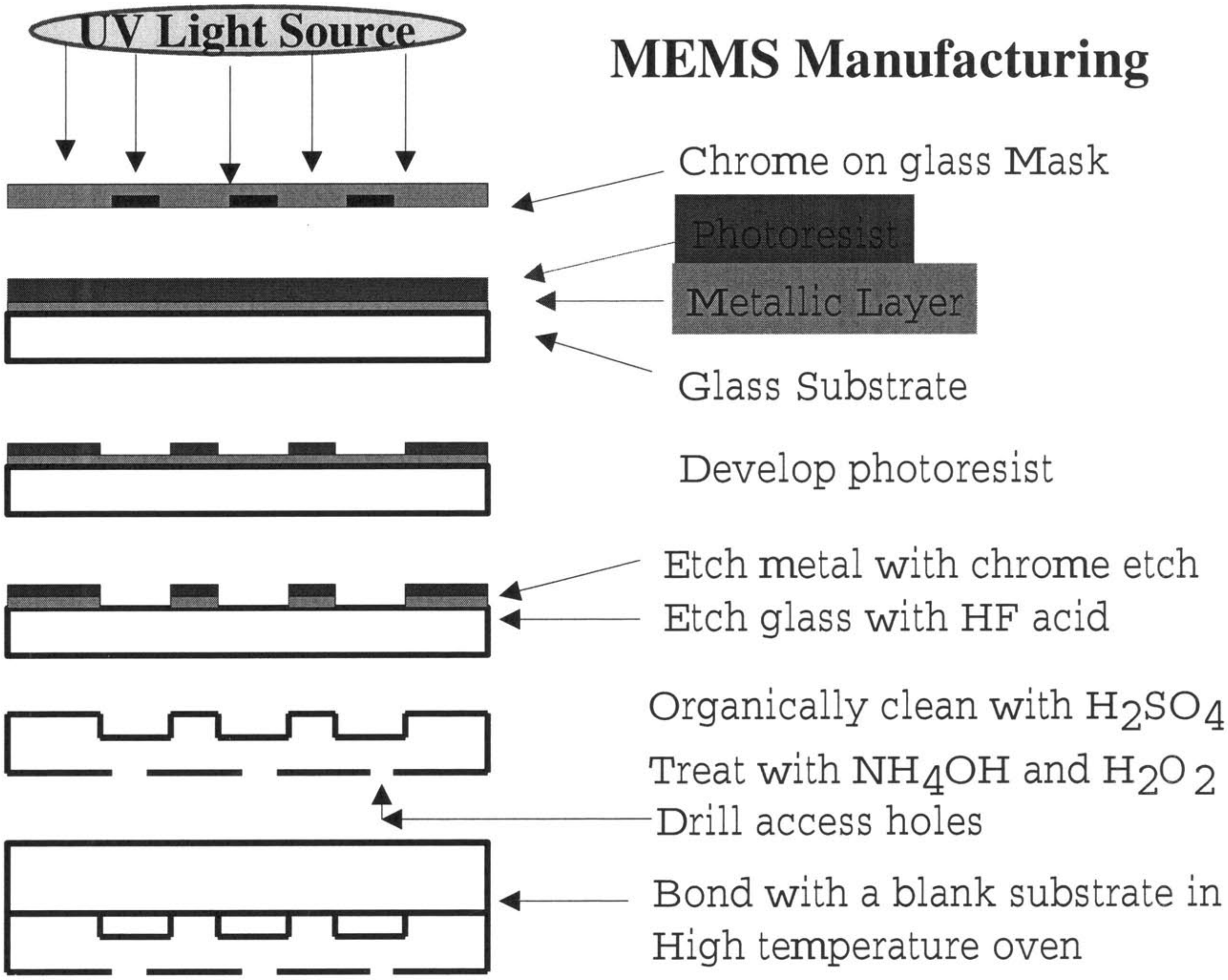

Figure 1-8: Conventional MEMS manufacturing via photolithography using ultra-violet light, a positive chrome on glass photomask, negative resist, and hydrofluoric acid (HF) etching.

Chemical Etching

Once a channel design has been transposed onto one of the substrates, the next step in the device manufacture is to obtain the desired depth. For this task, the substrate is placed within a bath of diluted hydrofluoric acid (HF) $\sim 2\%$ by volume. HF is an extremely strong inorganic acid that is commonly used for a variety of processes ranging from glass frosting to plastic production. Although HF acid is a corrosive compound, the hydrogen ion plays a relatively minor role in etching as it is the fluoride ion which binds with the silica to remove the substrate material [14]. Using HF, silica is removed from points lateral and perpendicular to the pattern of interest, meaning an HF etch produces a semi-hemispherical channel rather than a purely rectangular one. The nonuniformity of the channel depth is an important point for subsequent imaging and micro-fluidics to be discussed in the forthcoming chapter 3.

Although hydrofluoric acid can be very dangerous if mishandled, it is used exclusively for BioMEMS manufacture because it is an extremely useful etch for silicon dioxide. HF has a number of advantages over other etching techniques that include its high reproducibility rate and low cost. The etch rate of silicon dioxide in HF is much larger than the etch rate of silicon which means patterns of interest are etched away preferentially and quickly. Further, HF can easily be masked by photoresist which prevents the etching of the remaining surface of the substrate. Additionally, the etch rate produced with HF is quite repeatable and remains constant after a large number of samples have been etched. This leads to the added benefit of producing near identical batches of devices. Lastly, the equipment required to etch with HF is relatively simple and inexpensive.

Channels are etched to a depth of 40μm at a moderate rate of 1.0 μm per minute. The channel depth is measured every hour using a profilimeter that provides a profile of the channel. When the desired depth is reached, the substrate is removed from the HF bath and aggressively rinsed with de ionized water for 30 minutes.

Laser Drilling

At this stage, the substrate contains the desired pattern and required channel depth. However, before the channel is formed by bonding the treated substrate with its blank partner, access holes must first be drilled into the ends of each channel in order to permit access during experiments. These apertures are important because during electrophoresis, all solutions are loaded into the channel through reservoirs located atop each of these drilled holes. The holes themselves are rather small and can often require pulsed gas laser drilling with ultra-high accuracy (e.g. excimer drilling) for 10μm-diameter apertures. However, larger apertures with $\sim$ 50 μm centers have been successfully utilized via lower-accuracy laser drilling for many conventional BioMEMS devices.

During drilling, a large number of inorganic and organic contaminants are introduced onto the substrate surface. This is harmful because any type of contamination can prohibit bonding and, therefore, can easily destroy the device. Hence, after drilling, aggressive cleaning of the substrate is required and the newly drilled substrate, together with its blank partner, are placed within a hot 'piranha', or nanostrip, solution for precise chemical cleaning. This solution provides an extremely aggressive cleaning treatment because it is comprised of 90% sulfuric acid and 10% hydrogen peroxide. These corrosive agents efficiently remove all residue from the substrates, including inorganics and organics such as oils from fingerprints. To insure thorough chemical cleaning, both substrates remain in the 'piranha' solution for approximately 24 - 36 hours.

High Temperature Bonding

Once the substrates are chemically washed of all contaminants, they are treated overnight with a different chemical solution of ammonium hydroxide and hydrogen peroxide. This new solution makes the substrate surfaces extremely hydrophilic so as to induce their initial attraction and subsequent bonding. The following day, both substrates are immersed within a water bath of de ionized water whose volume is continuously flushed once per minute. This induces additional hydrophillicity from the substrates which are then pressed together underneath the water level in order to begin the bonding process. The pressed substrates are then placed within a low temperature oven at 200°C overnight to begin chemical bonding. Low temperature is used to evaporate excess water molecules that remain between the substrate surfaces after they are initially pressed together in the water bath. To further stimulate their bonding, a weight of $\sim$ 10 lbs is evenly distributed on their surface.

Inspection the following morning ascertains if the low temperature phase was accomplished successfully, or if the substrates de-bonded while their sandwiched water molecules were evaporated. If the substrates display signs of bonding, the device is placed within a high temperature oven for an additional 48 hours and ramped up to 735°C in order to complete the long-lasting chemical bond between substrates. If the low temperature phase was unsuccessful, substrates are placed back in the hot piranha solution and are ready for the next bonding attempt within 24 hours.

Coatings

Successfully bonded devices are subsequently coated with a low molecular weight linear polyacrylamide (LPA) solution that adheres to the surface of the newly formed channel [54]. This coating is conventionally applied in several stages that require sodium hydroxide exposure for 12 hours, immersion in bi-functional solution for a subsequent 24 hours, and final loading within the channel for an undisturbed 12-hour period. Once the coatings are complete, the center of the channel is filled with a polymeric sieving solution that enables separation.

1.3.3 Alternative Devices

Although conventional BioMEMS utilize glass or silica, many pioneering researchers have fabricated devices using polymeric materials, most specifically, PDMS, poly(dimethylsiloxane). Micromolding techniques using PDMS have successfully produced similar micro fluidic devices for a fraction of the cost [59], [83]. Micromolding involves the manufacture of channel negative, using PDMS polymer, and glass. First, a master negative of the desired channel is made using conventional photolithography. Next, a master mold is etched out of glass or polymer and finally, a PDMS solution is poured over the master mold. The polymer is allowed to cure for 24 hours and is then peeled and placed onto a desired glass surface. The PDMS mold hermetically seals to the glass and creates a closed microchannel within a few hours.

Regardless of the manufacture route, MEMS devices must be filled with a polymeric sieving solution that enables separation of DNA by molecular size. The particular properties of the sieving matrix is a large area of research undertaken by many polymer chemists. The pore size, molecular weight, and monomer length must all be optimized to produce the best separations. Concentrated solutions(2% - 6% (w/v)) of Linear PolyAcrylamide (LPA) are widely used in CE and Microdevice electrophoresis because of their viscosity and self coating ability [85], [84]. Hence, the unique properties of the polymeric solutions used for separation are now discussed, followed by the specificities of the DNA macromolecules which migrate within them.

1.4 Polymers and Macromolecules

A polymer is a large molecule composed of many simple structural subunits called monomers. Due to their large size and repetitive nature, polymers are also often called macromolecules. Synthetic macromolecules, such as polypropylene and polyethylene, are widely used for their light weight and high strength [90], while biological macromolecules, such as DNA and proteins, are widely studied for their conformational properties [86], [87] [144]. Most polymers are linear macromolecules, which means their subunits are joined together in a linear chain called the molecular backbone. The backbone is generally highly flexible as chemical units continuously twist and bend around their various degrees of freedom due to thermal or mechanical agitation. Further, a macromolecule is acted upon by Brownian motion which induce the molecule to exhibit a coiled configuration in its natural state [89].

1.4.1 Types of Solutions

Polymer solutions are considered liquid mixtures of long macromolecular chains, and small, light molecules of solvent [89]. Polymer solutions are classified into four different regimes based upon the separation distances observed between individual macromolecules. These regimes are called dilute, unentangled-semi-dilute, semi-dilute-entangled, and concentrated. A dilute solution is one where the concentration of polymer is sufficiently low such that macromolecular chains are hydrodynamically isolated from each other. Here, polymers have close to zero interaction with one another and are largely unaffected by neighboring macromolecules. As the concentration of polymer is increased, the number of macromolecular chains begins to increase and coils begin to come in contact with one another. Although coils are now in close contact, they do not interpenetrate or interact with one another and the solution is classified as semi-dilute but unentangled. Additional increases in polymer concentration generate solutions where polymer coils do interact and interpenetrate to form entanglements. These types of solutions are called entangled semi-dilute solutions because macromolecules now begin to interact and overlap with their neighbors due to their close contact. Entangled solutions are distinguished by their interpenetrations because the entanglements affect the physical properties of the solution. The polymer volume fraction, also often called the overlap threshold , c*, identifies the concentration for which macromolecules just begin to overlap and interact with one another. This critical concentration identifies the formation of entangled solutions and is defined [91] as:

$$c^* = \frac{3M_r}{4\pi N_A R_g^3} \tag{1.27}$$

where c^* is the critical concentration in g/ml, M_r is an averaged polymer molecular weight, N_A is Avagadro's Number, and R_g is the radius of gyration.

Lastly, a further increase in macromolecular concentration leads to concentrated solutions where polymer chains interact so strongly with one another that they form a physical network of entanglements. As the polymer coils continue to overlap and interpenetrate, a new parameter called the entanglement concentration, $c^\dagger$, defines the new region of concentrated solutions [70]. Scaling arguments the relationship between the entanglement concentration and molecular size:

$$c^\dagger \sim N^{5\nu-3} \tag{1.28}$$

Where N represents molecular size, and ν is the excluded volume coefficient [70]. For θ-solvents, the excluded volume coefficient is approximately 1/2, indicating the entanglement concentration is molecular weight-dependent. For good solvents, however, ν approaches a value of 3/5 indicating $c^\dagger$ is independent of molecular weight. In this case, Graessley has shown that the entanglement concentration, $c^\dagger$, is generally near 10% [70].

1.4.2 Properties

Regardless of the type of solution used, polymeric solutions possess several unique physical properties due to their fluidic microstructure. This section highlights those parameters most important to the discussion of electrophoresis such as molecular weight distribution, viscosity and viscoelasticity.

Molecular weight Distribution

When a macromolecule is dissolved into solution, a mixture is formed between smaller solvent molecules and individual polymer coils, each with a specific molecular weight. A solution composed of macromolecules of the same molecular weight is called monodisperse. Conversely, solutions comprised of macromolecules of varying molecular weights are called polydisperse. Although many biomolecules are monodisperse in nature, synthetic polymers are typically polydisperse solutions. Hence, when working with any polymer solution, it is pragmatic to establish its molecular weight distribution before measuring any of its properties or analyzing its flow.

In order to describe molecular weight distributions quantitatively, we assume that a polymer solution is composed of a fixed number of monodisperse populations, i. Further, each population contains N_i moles of molecules with a specific molecular weight, M_i. To define the molecular weight of a solution, different kinds of averaging methods can be used. One of the most commonly used molecular weight definitions is that of the number-average molecular weight, M_n. This average is obtained by multiplying the molecular weight of each population by its number of moles, and dividing the result by the total number of moles in solution.

$$M_n = \frac{\Sigma N_i M_i}{\Sigma N_i} \tag{1.29}$$

Note, M_n is sensitive to the addition of small amounts of low molecular weight populations because it divides by the total number of moles as seen in Equation 1.29.

Another way to describe the molecular distribution of a solution is to use the weight-average molecular weight, M_w. This quantity uses the weight fraction of each population to form an average rather than the number of moles. The weight of the solution is equal to the weight fraction of each population, w_i, times its molecular weight, M_i. The weight-average molecular weight is then determined by averaging the molecular weight of each population with respect to the total solution weight.

$$M_w = \frac{\Sigma w_i M_i}{\Sigma w_i} = \frac{\Sigma N_i M_i^2}{\Sigma N_i M_i} \tag{1.30}$$

The weight-average molecular weight, M_w is consequently more sensitive to the addition of high molecular weight species. Note, although M_n and M_w are two of the most commonly used molecular weight averages, many other types of averaging may be used for specific applications [84].

The commonly-used molecular weight averages, M_w and M_n of a polymer sample can be also describe its polydispersity. Due to the difference in averaging used, M_n and M_w will never predict the same molecular weight for a given polymer unless itis monodisperse. Rather, M_w will always be slightly higher than M_n as seen from Equations 1.29 and 1.30. Although the details of the shape of the distribution depend upon the preparation, and any fractionation, a simplified measure of the polydispersity index, *PDI*, is often given by:

$$PDI = \frac{M_w}{M_n} \tag{1.31}$$

Note that a solution is generally considered monodisperse if its polydispersity index is less than ~ 1.5 [84], [85].

Viscosity

Perhaps the most significant characteristic of all polymer solutions is their viscosity, η. The viscosity of a polymer solution is a measure of the fluid's resistance to change in shape or flow. Viscosity can be thought of as a fluidic internal friction, or more conventionally, as a measure of how 'sticky' the fluid is. Solutions with higher values of viscosity indicate the fluid flows less readily under applied pressure gradients, while solutions of low viscosity flow quite easily. Newtonian fluids are defined by their constant viscosity, μ, and its linear dependence on shear-rate via Newton's Law [71].

$$\tau_N = \mu\dot{\gamma} \tag{1.32}$$

where τ_N is shear stress experienced by a Newtonian fluid, and $\dot{\gamma}$ is shear-rate. Polymer solutions are often called non-Newtonian fluids because their viscosity does not concur with the Newtonian representation of Equation 1.32. Rather, the shear stress of a polymeric solution, τ, depends upon a viscosity that is largely dependent on the imposed shear-rate, $\dot{\gamma}$.

$$\tau_P = \eta(\dot{\gamma})\dot{\gamma} \tag{1.33}$$

where τ_P is shear stress experienced by a polymeric solution, and η is the solution viscosity as a function of shear-rate, $\dot{\gamma}$. The non-Newtonian viscosity, η, typically has three characteristic regions shown in Figure 2-1: a low shear-rate plateau, a shear thinning region and a high shear-rate plateau. The maximum viscosity value, corresponding to low shear-rates, is called the zero shear-rate viscosity, η_0, and is defined by:

$$\eta_0 = \lim_{\dot{\gamma}\to 0}[\eta(\dot{\gamma})] \tag{1.34}$$

The zero shear-rate viscosity, η_0 represents polymer viscosity under near equilibrium conditions and can be correlated to the molecular weight of the polymer through calibration [90]. The infinite shear-rate viscosity, found at very high shear-rates, is usually the solvent viscosity.

The region in between the maximum and minimum viscosity values is called the shear thinning region. Within these intermediate shear-rates, the viscosity of the polymer solution, when plotted on log-log scale, exhibits a pronounced linear decrease in viscosity over several decades [159]. Graessley's entanglement theory [70] attributes the non-Newtonian viscosity behavior to the effect of shear-rate on entanglement density [70]. As shear-rate is increased, polymer chains become increasingly disentangled resulting in lower viscosities.

Lastly, the point of transition from the low shear-rate plateau to the shear thinning region occurs at a critical shear rate, $\dot{\gamma}_C$. This parameter often provides insight into the polymer molecular weight, molecular weight distribution, and concentration. For instance, polymers with narrow molecular weight distributions transition into the linear shear thinning regime across a very narrow range of shear-rates.

Other Material Properties

As seen, polymeric solutions exhibit very different flow properties from Newtonian fluids due in large part to the solution microstructure which is composed of flexible macromolecules.

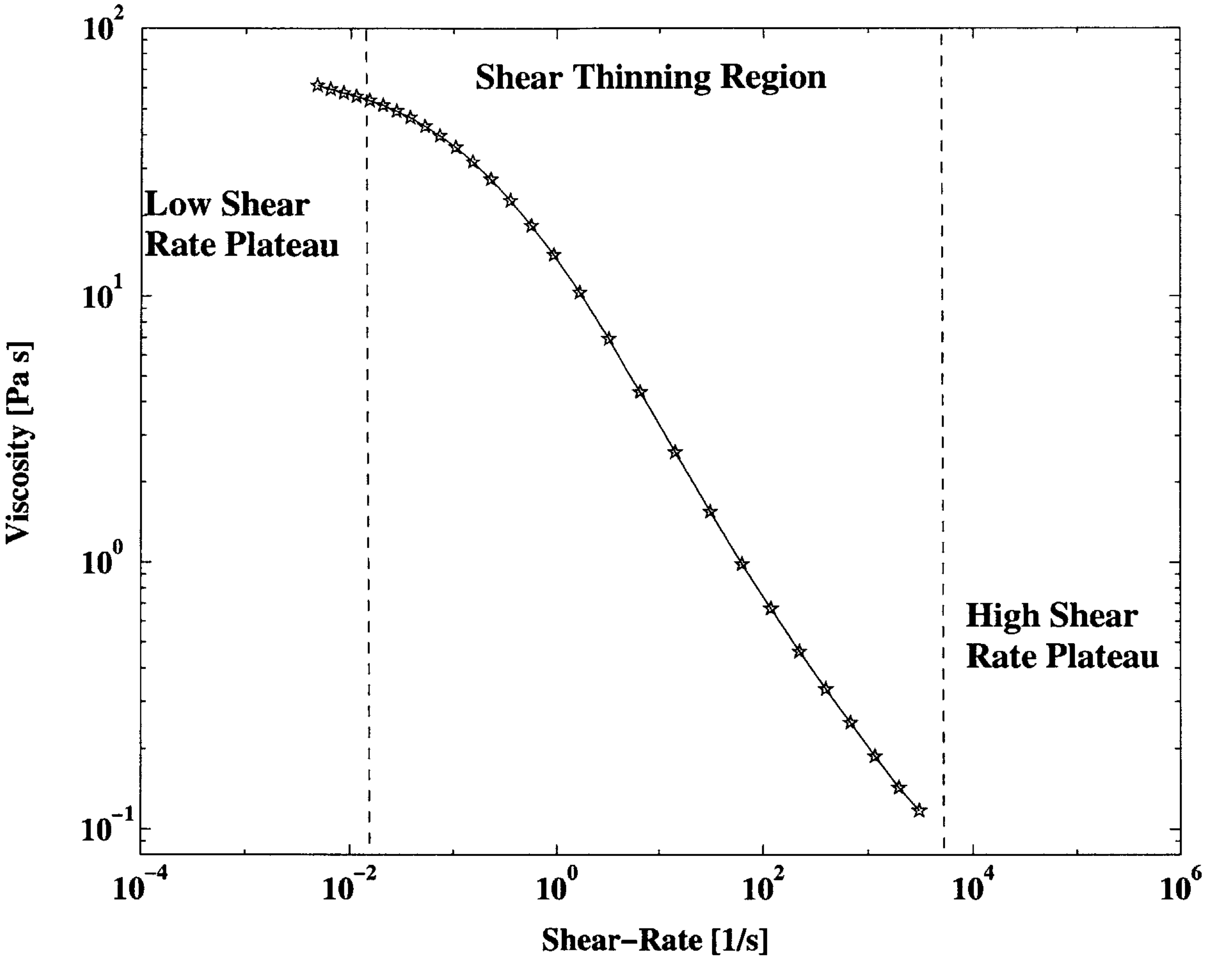

Figure 1-9: Representative plot of the non-Newtonian viscosity of a polymeric solution. High shear-rate plateau, shear thinning, and low shear-rate plateau are identified.

Another notable characteristic of non-Newtonian fluids is that they exhibit shear and tension along flow streamlines [159]. The extra tension in polymeric solutions arises from the stretching and re-orientation of their polymer coils during flow, which is not applicable to Newtonian fluids. As a result, polymeric fluids experience non-zero normal stresses during flow. The differences between the components of these stresses are represented by the first and second normal stress coefficients, Ψ_1 and Ψ_2, respectively, defined below for shear flows.

$$\Psi_1(\dot{\gamma}) = \frac{\tau_{xx} - \tau_{yy}}{\dot{\gamma}_{yx}^2} \tag{1.35}$$

$$\Psi_2(\dot{\gamma}) = \frac{\tau_{yy} - \tau_{zz}}{\dot{\gamma}_{yx}^2} \tag{1.36}$$

Where τ_{ii} represents the values of normal stresses in each corresponding direction, i, and $\dot{\gamma}$ is the shear-rate. Similarly, the stress ratio, SR, measures the fluid elasticity in terms of the relative magnitude of the normal stresses with respect to the shear stress.

$$SR = \frac{(\tau_{xx} - \tau_{yy})}{\dot{\gamma}_{yx}^2} \tag{1.37}$$

The stress ratio increases monotonically with shear-rate and has typical values of 2 -3 for polymer melts, such as polyethylene, but can exhibit values as high as 20 - 30 for polymer solutions such as polyacrylamide. Fluid elasticity is a very important aspect of non-Newtonian fluids as all polymeric solutions are classified as viscoelastic fluids.

Viscoelasticity

Polymeric solutions are classified as viscoelastic liquids because they display both elasticity and viscous dissipation during flow. The properties of viscoelastic solutions lie somewhere between those of a pure elastic solid, and an ideal viscous liquid. A pure elastic solid is a material that has a definite shape which can be deformed by external forces, but is fully restored once the load is removed [76]. In contrast, an ideal viscous liquid has no definite shape and flows irreversibly under external forces [71]. In a pure elastic solid, stress is linearly proportional to strain via Hooke's relationship.

$$\tau_{yx} = G \cdot \frac{\partial \delta_x}{\partial y} \tag{1.38}$$

where τ represents shear stress in Pascals, G is the elastic modulus, also in Pa, and $\frac{\partial \delta_x}{\partial y}$ is the deformation gradient measured in m/m. A linear viscous fluid under shear stress obeys a different relationship, i.e. Newton's Law:

$$\tau_{yx} = \mu \cdot \frac{\partial u_x}{\partial y} \tag{1.39}$$

where μ is the linear fluid viscosity in Pa-s and $\frac{\partial U_x}{\partial y}$ is the rate of deformation measured in 1/s. Polymeric solutions exhibit viscoelastic behavior because their microstructure enables them to store energy elastically, and simultaneously dissipate energy through shear-flow when a load is applied. Macromolecules retain their entropy and give rise to the concept of 'fading memory' in polymer systems. Here, polymer coils attempt to recover their equilibrium configuration as they relax when the load is removed. Since the molecules are entangled, flexible coils, there is a time lag associated with their recovery, called a relaxation time, λ. Polydisperse mixtures are comprised of numerous macromolecules, each of which may exhibit a different relaxation time corresponding to its initial length and conformation. Hence, a given polymeric solution exhibits a spectra of relaxation times, denoted $\lambda_1 ... \lambda_N$.

One common dimensionless group used to characterize the non-Newtonian, or elastic, properties of a solution is called the Deborah number, De [159]. The Deborah number relates the solution time scale to the observed time scale as shown in Equation 1.40.

$$De = \frac{\lambda}{t_{obs}} \tag{1.40}$$

Where λ is the longest relaxation time of the polymer solution, and t_{obs} is the observed time. The concept of the Deborah number is based upon the idea that all matter flows, if given a sufficiently long observation time scale. The quantity De can be alternatively be interpreted as, 'How long will a fluid remember its previous deformations?' If the time scale of observation is very large, or if the relaxation time of the material is very small, the Deborah number approaches zero, $De \sim 0$. This means the fluid forgets previous deformations quickly and an observer can witness the material flowing. Conversely, if the relaxation time of the material is larger than the time of observation, the Deborah number approaches infinity, $De \sim \infty$. Here, the fluid will remember previous deformations forever, and the material never appears to flow to an observer. Flows of a viscoelastic material exhibit a Deborah number in between these two limits, near order one, $De \sim 1$. Given the added complexities associated with the properties of polymeric solutions, an analysis or design involving such materials must incorporate their time-dependent, viscoelastic behavior.

1.4.3 Models

Viscoelastic models provide constitutive relations to describe many of the time-dependent motions of polymers. Linear viscoelastic models describe the properties of a material under very small strain or deformations such that the fluidic microstructure remains unperturbed during flow [159]. Although the results are only valid for very small deformations, linear viscoelastic models can be used to interpret viscoelastic behavior for many flow properties, at least qualitatively. Two of the more commonly-used linear viscoelastic models are the Maxwell and Kelvin models.

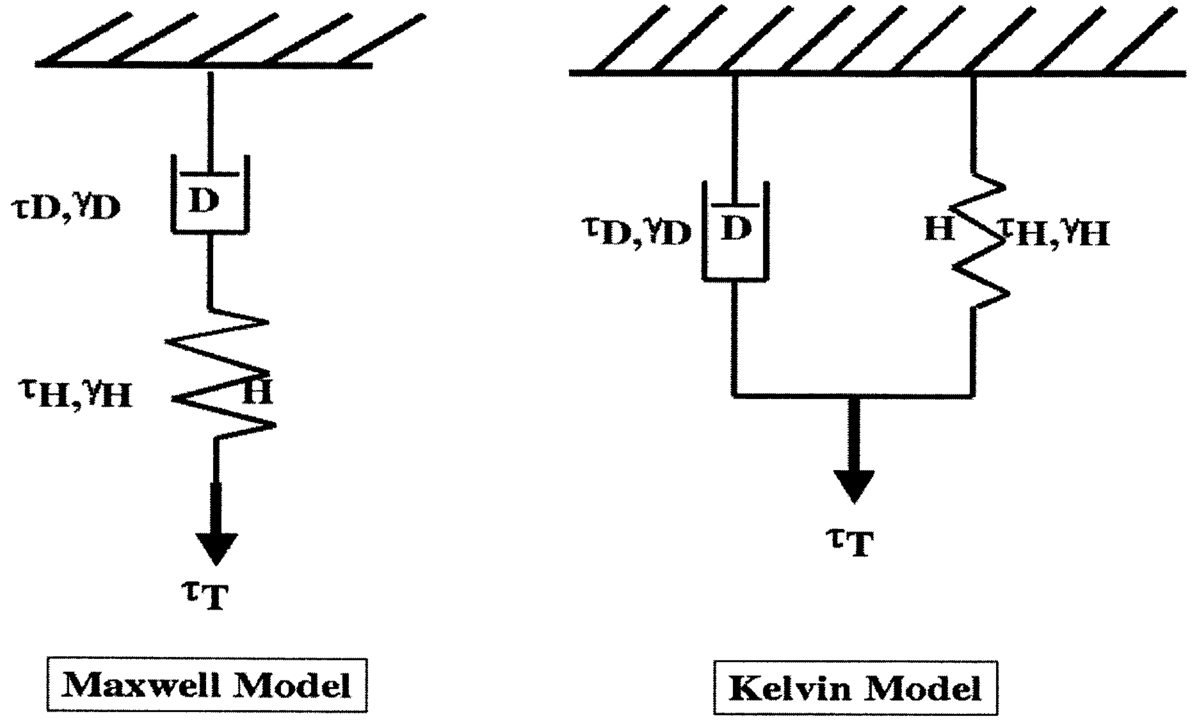

Maxwell Model **Kelvin Model**

Figure 1-10: Schematic representations of the Maxwell and Kelvin Linear Viscoelastic Models.

Both the Maxwell and Kelvin models incorporate the elasticity and viscous dissipation of polymeric solutions by representing each with an ideal system element. The elastic portion of the polymeric response is represented by an ideal Hookean spring, *H*, while the viscous response is characterized by a dashpot, *D*, in both models. In the Maxwell model, these elements act in series when a shear stress, τ is applied to the system, as seen on the left-hand-side of Figure 1-10. Such a configuration indicates that the displacements of each element are additive, $\gamma_T = \gamma_H + \gamma_D$, but the shear stress experienced by each is equal,

$\tau_H = \tau_D$. Conversely, these elements are connected in parallel by the Kelvin model, as seen on the right-hand-side of Figure 1-10, so that their displacements are equal, $\gamma_H = \gamma_D$, but their shear stresses are additive, $\tau_T = \tau_H + \tau_D$. The characteristic equation for each system is obtained using basic Kirchoff circuit analysis.

Maxwell Model

$$\tau + \frac{\eta}{G}\frac{\partial \tau}{\partial t} = -\eta_0 \gamma \tag{1.41}$$

Kelvin Model

$$\tau + \eta_0 \frac{\partial \gamma}{\partial t} = -G\gamma \tag{1.42}$$

where τ is shear stress, γ is displacement, $\dot{\gamma}$ is shear-rate, η_0 is zero shear-rate viscosity, and G is the relaxation modulus. Note, both models are only qualitatively describe viscoelastic phenomena because they oversimplify the elastic and dissipative aspects of polymer solutions under stresses. However, the Maxwell model can be used for experiments that apply constant shear-rate, $\dot{\gamma}$, while the Kelvin model is more favorable for experiments that model constant stresses, τ, such as creep behavior.

Increasingly complex models develop more accurate constitutive relations better able to describe the response of a real polymeric system. The Generalized Maxwell Model, for example, uses the viscoelastic spring and dashpot system in series N times to account for the N relaxation times exhibited by the polymeric solution, $\lambda_1 ... \lambda_N$. Similarly, models such as the Burgers [69] and Voigt models [85] use multiple dashpot elements, in both series and parallel, with multiple Hookean elements in order to better represent the viscoelasticity of polymer solutions. Additionally, non-linear viscoelastic models describe the viscoelastic response of polymer systems using integral and differential models which are not limited to small deformations in the flow. However, precise knowledge of the viscoelastic response of a material is based on measurement and, hence, the study of rheology is an important one in polymer systems.

1.4.4 Rheology

Rheology is the science of flow and deformation of matter that describes the interrelations between force, deformations and time [85]. Rheometry provides a means to extract molecular information about polymer solutions from bulk measurements of the fluid viscoelasticity. A rheometer is used to measure fluid material properties from experiments that impose constant shear stress, τ, or shear-rate, $\dot{\gamma}$. In this manner, viscosity, η, relaxation modulus, G, normal coefficient of stress, Ψ_1 and Ψ_2, and stress ratio, SR, are calculated. While viscometers make a single measurement of viscosity at a fixed shear-rate, rheometers measure deformations using both a shear-rate and frequency analysis. Rheometric equipment is needed in the laboratory because researchers do not usually generate homogeneous flows, nor directly measure the material functions of a solution. As a result, engineers use rheological equipment to measure forces and torques exerted on pieces of the equipment and relate these measurements to the desired material functions.

Conventional rheometers include the parallel disk, plate and cone, and rotating disk rheometers. In the common cone and plate rheometer, the polymer solution is placed within the thin gap formed between an inverted cone and plate as the cone is rotated at different angular velocities. For small cone angles, a near homogeneous shear flow develops in the gap and by varying the imposed torque, the viscosity as a function of shear rate, $\dot{\gamma}$, or shear stress, τ is obtained [159]. One can also determine values for the complex and dynamic viscosity, η^* and η', respectively for small amplitude oscillatory flows.

In addition, rheometry enables the measurement of other important parameters such as the storage modulus, *G'*, and loss modulus, *G"*. The storage modulus provides information about the elastic behavior or energy storage of the material during deformations while the loss modulus describes the viscous characteristics of the fluid, or its energy dissipation during flow.

For DNA electrophoresis, we are interested in the measurement and analysis of flow of very dilute solutions of DNA macromolecules. Further, solutions of DNA are highly polydisperse as they are comprised of molecules whose molecular lengths vary by two orders of magnitude. In the next section, we explore the properties of individual DNA molecules more specifically, and discuss their mechanisms of migration and separation.

1.5 The DNA Macromolecule

Specific knowledge of the DNA macromolecule is a prerequisite for any study of DNA electrophoresis. DNA is one of the more heavily researched biological macromolecules both because it accounts for the molecular uniqueness of organisms, and because it is an ideal polymer molecule that occurs naturally in monodisperse samples and in various configurations. DNA is comprised of nucleic acid monomers and is an acronym for deoxyribose nucleic acid. The nucleic acids are predominately chemical combinations of sugar phosphates and four dominant bases: Adenine (A), Cytosine (C), Guanine (G) and Thymine (T). Although the helical configuration of DNA is well known, DNA also exists in star-shaped or super coiled configurations [12].

1.5.1 Single Molecule Dynamics

Dynamic motion of these biomolecules is characterized by chain conformation and flexibility, both of which are functions of molecular composition and length. One of the simplest idealizations of a flexible polymer chain is the 'random-walk' configuration [91]. Here, a macromolecule is represented by a series of N repeat units, aligned randomly in space and each of length l. The random-walk is used to describe a variety of physical phenomena, ranging from diffusion to the conformation of long molecular chains. The random-walk model of a macromolecule is obtained by assuming that conformations of a single link of the polymer are equally probable. Consider a simple square lattice on which a random-walk DNA molecule is placed. Each link of the molecule regards its initial position as the origin and will migrate to a new position in the lattice at random. There is an equal probability that the new position will be any of the link's nearest neighbors. However, once the link reaches this position, it establishes a new origin and forgets its original position. In this way, the links of a DNA molecule following a random-walk make each step at random, and independently of other steps and links. The random-walk behavior is also often linked to translational Brownian motion where thermal collisions cause molecules to execute a random walk. Each step of a random-walk is measured by the length l, which is also called the persistence length of the molecule [93]. This definition arises because it is the length scale at which Brownian motion dominates over structural rigidity.

Table 1.1: Properties of λ-DNA.

Property	Symbol	Value
Contour Length	L	16 μm
Persistence Length	l	53 nm
Charge	q	1.6×10^{-19} C
Ionic Conductivity	κ_D	$0.00143\ S/m^2$
Base Pair Spacing	S_{BP}	2.3

The power of using the random-walk lies in the ability to mathematically model and analyze many properties of an entangled macromolecule. For instance, the separation distance between the free ends of a molecule can be mathematically represented by the time-averaged-mean-square-distance between them, $< R^2 >$:

$$< R^2 >= Nl^2 \tag{1.43}$$

Further, the square root of the end-to-end distance can be used to represent the radius of an entangled molecule, R_g. Termed the radius of gyration, R_g represents the average separation distance between a chain segment N, and the molecule's center of mass [89]. The radius can be mathematically represented as:

$$R_g = \sqrt{(R * R)} = \frac{N^{1/2}l}{\sqrt{6}} \tag{1.44}$$

Commonly-used λ-DNA has a persistence length of 53 nm and a contour length of $\sim$ 160 nm. It has a constant charge per unit mass of e, and an ionic conductivity in dilute solution that is less than $10^{-2}S/m^2$. Various physical properties of the λ-DNA macromolecule are shown in Table 1.1.

1.5.2 Molecular Models

The single chain dynamics of most polymer systems can be described by a variety of molecular models such as the Bead and Spring [159], Worm-Like-Chain [89], and FENE dumbbell [69]. Two of the simplest molecular models commonly used in polymer science are the Rouse and Zimm models. Both models represent a polymer strand as a collection of beads and entropic springs where beads represent the viscous interactions of the chain, and springs represent their elastic interactions. The Rouse model assumes the macromolecule will behave as a 'free-draining coil', which means the flow will penetrate through the macromolecule with molecular interaction. Here, the flow imposes a hydrodynamic drag which acts only on the beads of the molecule. In contrast, the Zimm model assumes the macromolecule is a 'non-free draining coil' such that flow does not penetrate through the molecule but rather interacts with the chain in its entangled state. Here, the bead and spring configuration deflects flow streamlines around the macromolecule and hydrodynamic drag is imposed along R_g. More complex models continue to use the bead and spring representation, but employ Hookean or non-linear elastic springs instead. Although these simplified models are a good starting point to describe the migration of viscoelastic molecules, the highly charged nature of the DNA macromolecule during electrophoresis introduces many other complications to the flow.

1.5.3 Polyelectrolyte Properties

The electric double layer and its affects on DNA migration have been previously discussed in section 2. However, the specific details of its formation are dependent upon the DNA molecule itself and its conformation. Polyelectrolytes are macromolecules having many ionizable groups, such as the nucleic acids in DNA. In solution, polyelectrolytes exist as large macro-ions surrounded by a huge number of smaller counter ions of opposite charge, e.g. solvent molecules. The high charge of the macro-ion produces a strong electric field that attracts the counter ions and the strong electric interaction between them is one source of the characteristic properties of polyelectrolytes.

Morphology of charged macromolecules is one of the central problems of polyelectrolytes. Most macro-ions are long flexible chains which are greatly expanded in solution. Their size and shape depend upon the charge and the interaction with counter ions. With increasing charge, the flexible chain changes its shape from a entangled coil to a fully extended one [74]. The effect of interactions among ionized groups, counter ions and solvent molecules is amplified by the high charge density of the macro-ion. A small difference in the interaction may have great influence on the properties of polyelectrolytes meaning they are most sensitive to structure and environment.

The polyelectrolyte nature of DNA is largely responsible for its specific mechanism of electrophoretic migration within polymeric solutions. The migration of DNA molecules can be described specifically by the models of Ogston sieving, reptation, and entropic trapping.

Ogston Sieving

The first model to describe the general migration of a flexible macromolecule through a polymer network was proposed by Sir A.G. Ogston in the 1950's [92]. In this model, DNA molecules are modeled as isotropic, non-deformable, spheres of radius R_g, with large double layers of thickness λ_D, while the polymer is represented by a random network of interconnected pores [92] of mesh size ξ. DNA migrates through the pores of a polymer matrix based upon its molecular size, R_g and the diameter of the pores, ξ, of the polymeric solution. The electrophoretic mobility of a molecule is, therefore, proportional to the available volume fraction of the polymeric medium as shown in Figure 1-11. In this form of migration, molecules with access to a larger fraction of the available pores travel fastest, and hence the Ogston model is often referred to as molecular sieving.

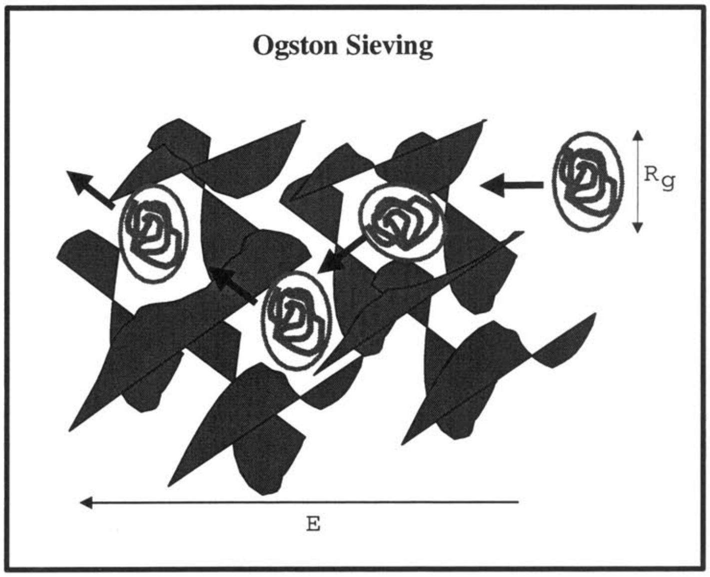

Figure 1-11: Electrophoretic Migration of a DNA Molecule within an Entangled Polymer Matrix via Ogston Sieving.

In the Ogston model, mobility is related to the probability that a spherical molecule will not overlap with polymer chains. The Ogston representation of the polymer matrix indicates that this probability is a function of the average length and thickness of the polymer strands [144]. The polymer matrix is represented by a random distribution of open pores surrounded by linear polymer fibers. The probability distribution of pores large enough to admit a molecule of radius R_g, is described by:

$$P(R_g) = \exp\left[-\pi\phi l(R_g + r)^2\right] \tag{1.45}$$

where ϕ is the average number of fibers per unit volume, l is the average fiber length, R_g is the DNA radius of gyration, and r is the fiber radius. Ogston hypothesized that DNA mobility is related to the probability that a spherical object will not overlap with matrix fibers. As a result, the Ogston expression for the mobility of a molecule, μ, decreases exponentially with increasing molecular size, N, or ${R_g}^2$.

$$\frac{\mu}{\mu_0} = \exp\left[-K(R_g + r)^2 C\right] \tag{1.46}$$

where μ_0 is the measured mobility of DNA in free solution (i.e. without a sieving matrix), R_g is the radius of gyration of a DNA molecule, r is the radius of the polymer fibers, C is the concentration of the polymer solution, and K is a constant of proportionality often incorporating the effects of the Debye length, λ_D.

The Ogston model also establishes estimates for the diffusivity, D, and relaxation time, λ, of a polymer system, which are key parameters of a non-Newtonian fluidic system. Here, Einstein's relation establishes a good estimate for the diffusivity, D.

$$D = \frac{k_B T}{f_d} \tag{1.47}$$

where k_B is the Boltzmann constant, T is temperature, and f_d is the coefficient of hydrodynamic friction imposed upon the macromolecule by the flow. The hydrodynamic force, F_d, exerted on a spherical, rigid, DNA molecule undergoing Brownian motion is described by

Stokes theorem [125].

$$F_d = 6\pi\eta R_g u = f_d u \tag{1.48}$$

where η is the non-Newtonian viscosity of the surrounding polymer matrix, R_g is the molecule radius, and u is velocity. Note that the size of a molecule is represented by the Zimm model and scales with R_g or $\sqrt{N}$. Note, using a Rouse model representation of DNA, the hydrodynamic drag would occur only on the beads of the polymer chain and would result in a linear dependence on the number of beads, N, (${R_g}^2$). This is a subtle but important point as substitution of Equation 1.48 into Equation 1.47 indicates that DNA diffusivity via Ogston sieving is inversely proportional to the square root of chain length.

$$D \sim \frac{1}{\sqrt{N}} \tag{1.49}$$

Lastly, the Ogston transport model is characterized by a maximum relaxation time, λ_M. Using scaling arguments, the relaxation time is represented by the end to end distance of the macromolecule divided by its diffusivity.

$$\lambda_M \sim \frac{< R^2 >}{D} \tag{1.50}$$

Where λ is the relaxation time, $< R^2 >$ is the root mean square distance between the two free ends of the DNA molecule, and D is the diffusion coefficient. By substituting the previous results of Equation 1.49 and 1.50, we obtain :

$$\lambda_M \sim \frac{N}{(1/\sqrt{N})} \sim N^{\frac{3}{2}} \tag{1.51}$$

which indicates relaxation time scales with the size of the DNA chain tp the 1.5 power. The relaxation times for long DNA molecules are known to be much greater than those of shorter fragments.

Yet, the Ogston model is a static model of migration which does not incorporate many of the critical dynamic factors that dominate DNA electrophoresis within entangled solutions [106], [148]. One needs to carefully determine if a dynamic property like mobility, μ, is truly directly proportional to a static quantity, such as the available volume fraction, as predicted by Ogston. Further, the Ogston model incorporates several restricting assumptions which are not necessarily applicable to electrophoresis of DNA [106]. For example, the Ogston model is a zero field model, meaning it assumes the magnitude of the electric field has no effect on the kinetic resistance of the matrix. Further, all matrix pores are assumed spatially uniform, and their connectivity and precise matrix architecture are neglected. Lastly, there are only excluded volume interactions between the particle and matrix in the Ogston model, meaning hydrodynamic interactions between the solute and the matrix are also neglected. However, despite these restrictions, numerous experiments [158] [43], [144] have verified the Ogston-type dependence of mobility on DNA size for single-stranded DNA molecules less than $\sim$ 200 bases in length, depending upon the properties of the separation matrix.

As seen from Equation 1.46, mobility decreases exponentially with molecular size so long as the radius of gyration, R_g, is smaller than the pore size of the polymer, ξ. When a molecule is larger than the polymer pore size, however, the Ogston model predicts that its electrophoretic mobility will rapidly approach zero. Since it is well-known that large DNA molecules continue to migrate under an electric field even when their radii of gyration are larger than the polymer pore size, larger DNA molecules must utilize a method of electrophoretic migration other than Ogston sieving. When describing the dynamic motion of such large, more entangled DNA molecules, a second migration method, called reptation, is considered.

Reptation

Transport via reptation was first described in publications by de Gennes, Doi, and Edwards in the 1970's. The basis of the model is that larger DNA molecules do not remain isotropic spheres during transport, but instead begin to elongate and migrate through the sieving matrix in a flexible, snake-like fashion as a result of the electric field [89]. A schematic of macromolecular motion via reptation is shown in Figure 1-12. In this case, the effects of the electric double layer are reduced as λ_D is diminished and the reptation model replaces the structure of the sieving matrix with a hypothetical 'tube' formed by a series of interconnected pores within the matrix. No lateral motion is allowed beyond the tube due to entanglements, forcing the molecule to migrate in the direction of the electric field solely by diffusing along the contour length of the tube.

For DNA molecules migrating under the applied fields typical of short-lane electrophoresis, the reptation model predicts that DNA obeys a random-walk within each pore of the sieving matrix during transport. When placed within a large electric field, however, the

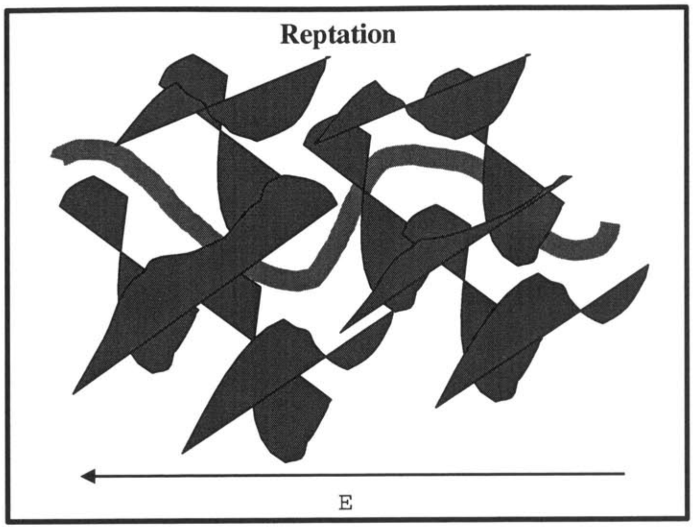

Figure 1-12: Reptative Migration of a DNA Molecule within an Entangled Polymer Matrix.

reptation model states that DNA molecules no longer follow a random-walk, but rather stretch and elongate in order to migrate in the direction of the electric field. The former phenomenon is called reptation while the latter is called biased reptation, or reptation with orientation [126].

Lumpkin et al. [45] developed an expression for DNA mobility which reflects the non-linear effects produced by the applied field in both reptation and biased reptation.

$$\frac{\mu}{\mu_0} = \frac{q}{3\eta}\left[\frac{1}{N} + \frac{Eql}{k_B T}^{2}\right] \tag{1.52}$$

In Equation 1.52, q is charge per unit length of DNA, η is the viscosity of the polymer matrix, N is the number of DNA segments, k_B is the Boltzmann constant, T is absolute temperature in Kelvin, l is the persistence length of DNA, and E is the applied electric field. The limits of reptation and migration via biased reptation can be seen from Equation 1.52. In the limit where the electric field is small, DNA mobility is inversely proportional to molecular size, N. In the opposite limit, where the electric field is strong, DNA mobility is size independent if the quantity $\frac{Eql^2N}{k_BT}$ is much greater than 1.

In general, reptation assumes that matrix fibers confine a molecule so that it can travel only by reptating along its own contour [89], [160]. It is also presumed that the conformation of the molecule, and the tube it inhabits, is influenced by the electric field. However, Slater and Noolandi [112] noted in 1985 that a finite field affects the tube conformation by influencing the motion of the chain ends, thereby causing an orientation effect. Further, Duke et. al. [41] demonstrated that the motion of the chain ends have to be considered rather carefully as rapid fluctuations in the positions of the ends due to DNA elasticity play a vital role in its reptative migration: The degree of molecular orientation induced by the electric field is determined by a competition between longitudinal fluctuations and drift of the molecule along the tube [41], [111]. These researchers demonstrated that that the end-to-end distance of long molecules varies with the square root of the field strength, not linearly as previously proposed. A modified reptation model was then termed, BRF, Biased Reptation with Fluctuations, which demonstrates that reptative mobility displays a non-linear dependence on the field strength due to the fluctuations of a molecule within its tube. Numerical simulations and experiments show that detailed results derived using the reptation model instead of BRF are likely invalid and must be revised [41].

Fortunately, the original reptation model remains correct at the qualitative level in most instances. Experimentally, mobilities that are inversely proportional to size, as per reptation theory, have been demonstrated by the migration of molecules larger than $\sim$ 120 bases in length within semi-dilute, entangled solutions [144]. Similarly, the mobility predicted by reptation with orientation has also been demonstrated by the migration of DNA molecules longer than $\sim$ 1000 bases within semi-dilute entangled solutions [44].

For reptating motion, the chain dynamics within the tube are well described by diffusion and relaxation time. But note, it is the diffusion coefficient of the reptating chain which is of interest, not the diffusivity of the tube. Using Einstein's relation once again, diffusion of a reptating chain scales as:

$$D \sim \frac{< R^2 >}{\lambda_M} \tag{1.53}$$

where $< R^2 >$ is the root mean square distance between chain ends and λ_M is the longest relaxation time of the system. However, the longest relaxation time of the reptating system (tube and chain) is best represented by the reptation of the tube itself. This is because the chain's memory of all previous deformations within the tube is lost making successive time intervals statistically independent [89]. The relaxation of the reptation tube is determined by the end-to-end distance of the tube, Λ^2 divided by the diffusion coefficient of the tube, D_{Tube}.

$$\lambda_M \sim \frac{\Lambda^2}{D_{tube}} \tag{1.54}$$

What remains is a scaling for the diffusivity of the tube, D_{Tube}. As a first order scaling, we can say that the linear diffusivity of a reptating tube is related to the diffusion of the reptating molecule and its molecular length.

$$D_{Tube} = \frac{D^*}{N} \tag{1.55}$$

where D^* is the diffusion coefficient of the individual segments, and N is its number of repeating segments. Through direct substitution of Equation 1.55 into Equation 1.54, we obtain a scaling for the longest relaxation time of the polymer chain.

$$D \sim \frac{N}{N^3} \sim \frac{1}{N^2} \tag{1.56}$$

Which indicates that the diffusion coefficient of a reptating chain scales with chain size to the power -2.

Entropic Trapping

Another mechanism of electrophoretic transport was experimentally discovered by researchers in the early 1990's. This mechanism is called Entropic Trapping (ET) and its theory is still under development by a number of researchers. The theory of entropic trapping is based upon the conformation energy of a DNA molecule and its changes in entropy during navigation. The premise of ET is that when the radius of a flexible molecule, R_g is comparable to the matrix pore size, ξ, the DNA's internal entropy becomes an important factor in its transport. Transport by ET implies that the conformational entropy of macromolecules determines their mobility through the matrix pores. The region of ET applicability is limited to DNA fragments whose internal entropy is on the order of the configurational entropy attainable within a pore. The entropy of a macromolecule can be described by the Boltzmann equation:

$$S = K_B lnW \tag{1.57}$$

Where k_B is Boltzmann's constant and W is the number of configurations available to the molecule. Thermodynamically, undisturbed macromolecules prefer to remain in a state of maximum entropy. From Equation 1.57, this corresponds to environments that allow the greatest degree of configurational freedom. The free volumes within larger sized pores of the matrix therefore attract DNA molecules because they provide large configurational freedom.

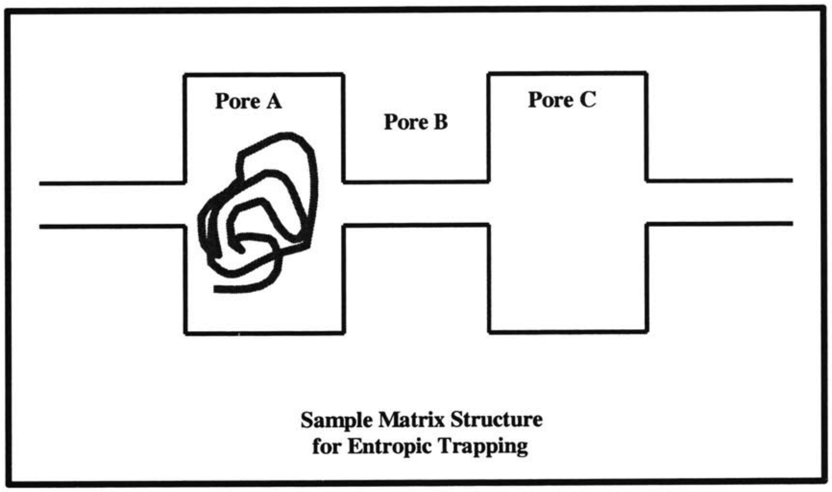

Figure 1-13: Schematic representation of the Entropic Barriers Model.

Consider a matrix with the structure shown in Figure 1-13. This particular configuration shows two large pores, A and C, connected to one another through a much smaller pore B. DNA undergoing electrophoresis within this matrix would experience large increases in configurational freedom within Pores A and C, maximizing its internal entropy to a value

S^{MAX}. However, transport from Pore A to Pore C must occur through Pore B, whose smaller free volume reduces DNA conformational freedom, resulting in a configurational entropy of S^{MIN}. The decrease in entropy, or activation energy, required for transport between the two pores is denoted by ΔS:

$$\Delta S = S^{MAX} - S^{MIN} \tag{1.58}$$

Proponents of ET transport argue that for this configuration, the DNA molecule will remain trapped within Pore A. The activation energy required for DNA transport from a pore where configurational freedom is maximized, to a pore where conformation is minimized, is too great for the chain to overcome. Transport from Pore A to Pore B restricts the configurational freedom of the molecule and hence, Pore B acts as an entropic barrier to translation.

Escape from such an entropic trap requires a decrease in the relative entropy, ΔS, between the configurational energy on one side of the barrier, Pore A, and the conformational freedom on the other, Pore B. This can occur if DNA configuration is altered to either decrease its entropy within Pore A or increase its entropy within Pore B. To increase the entropy of the chain within Pore B, the diameter of the pore must be expanded. This cannot realistically be performed during electrophoresis. However, a decrease in the entropy of the chain within Pore A can be accomplished through an increase in the electric field. The non-linear effects of the voltage on the DNA molecule result in chain orientation and elongation which alters the molecule's configuration. When the DNA molecule is elongated and oriented, its configurational entropy within Pore A is no longer a maximum, but instead a lower quantity, S^*. The activation entropy, ΔS^*, now required for ET transport between the pores has decreased and the DNA molecule can break free of the trap and continue its migration.

$$\Delta S^* = (S^* - S^{MIN}) < (S^{MAX} - S^{MIN}) \tag{1.59}$$

Video microscopy images by Chern et al [94] document the motions of a DNA molecule within an entropic trap. The images illustrate how DNA molecules form spherical blobs in order to maximize their conformational entropy while they are caught in an entropic trap. Increasing the electric field orients the DNA molecule more strongly and also produces sufficient chain elongation to enable transport out of the pore. For increased fields, the images show an initial orientation and stretching of the DNA molecule and then a quick transport out of the pore. Further experimentation [94]concluded that if left undisturbed, DNA molecules remain trapped within the pores indefinitely.

Transport by entropic trapping implies that DNA mobility through an external matrix is determined by the conformational entropy of the macromolecule. As a result, transport via entropic trapping is limited to DNA fragments whose internal entropy is on the order of the configurational entropy attainable within a matrix pore. Both experimental data [110], [109] and computer simulations [108] have illustrated that the entropic barriers model is most valid for combinations of low fields and large DNA molecules. Rousseau et al [107] verified experimentally that entropic trapping is not important for molecules less than 300 bases in length and does not exist in fields greater than 30 V/cm.

Unfortunately, a physical model describing transport by Entropic Trapping is not yet analytically defined. However, independent numerical results [96], [97] determined that physical scaling for ET transport resemble that of reptation. Hence, a preliminary physical model to describe transport by ET uses the reptation scaling parameters with an adjustment factor, β. The parameter β represents the strength of entropic traps within the ET regime. The ET mobility can be related to the frequency of barrier crossings (i.e. pore structure) and expressed in terms of β.

$$\mu \sim \frac{1}{N^{1+\beta}} \tag{1.60}$$

Entropic barriers also retard the long-range diffusion of macromolecules and can be expressed in a manner similar to mobility:

$$D \sim \frac{1}{N^{1+\beta}} \tag{1.61}$$

When a DNA molecule enters an entropic barrier, it remains trapped within the pore for a certain time t_{ET}. This time scale was described by Han et al [98] as:

$$t_{ET} \sim \exp\left[\frac{\alpha}{E_s k_B T}\right] \tag{1.62}$$

Where α is a constant, k_B is the Boltzmann constant, T is temperature and $\mathbf{E}$ is the electric field.

Although development of the entropic barriers model is fascinating, ET is not a viable mechanism of electrophoretic transport for smaller sized DNA molecules within high fields. Hence, only the mechanisms of Ogston sieving, reptation and biased reptation, are utilized by DNA molecules of a sequencing reaction during their migration and separation within microfabricated channels.

In order to understand the migration of DNA molecules within microdevices more specifically, microscopy experiments are used to capture the electrophoretic movements of DNA within applied fields. Since many of the conclusions obtained from this study are obtained from digital images, the next section outlines the basics of microscopy and how it is used to gather images of biomolecules.

1.6 Introduction to Microscopy

Scientists and engineers routinely use microscopes in order to produce a magnified, visual image of a micro or nanoscale object. Microscopes exploit the reflection and refraction of light by using optical lenses and mirrors to direct light rays as needed in the optical train between the specimen and the eye. The quality of a lens if often described in terms of its numerical aperture, NA, and resolution characteristics, R_L. The numerical aperture measures the ability of the lens to gather light at a fixed distance.

$$NA = [n][\sin(\theta)] \tag{1.63}$$

where NA denotes numerical aperture, n is the index of refraction of the material, and θ is the half angle of incident light. Resolution is the ability of the lens to resolve specimen details and is described as the minimum distance needed to distinguish two separate points of an image. The resolution of a particular image system is determined by the Abbe equation [76]:

$$R_L = \frac{\lambda \cdot 1.22}{NA_{OBJ} + NA_{COND}} \tag{1.64}$$

where R_L is resolution, λ is the wavelength of the illuminating light, and *NA* is numerical aperture of the objective and condenser respectively. In general, the resolution magnification of a lens is $\sim$ 1000 times its numerical aperture. For example, a 40x objective with an NA of 0.65 has a useful magnification of 650 times. Beyond this point, the image looks fuzzy primarily due to optical abberations.

1.6.1 Depth of Focus

One very important aspect of microscopy-based research is the depth of focus used. Details visible on images with different focus settings, are generally not visible on a single image because of the limited depth of focus typical of conventional microscopes. As a result, the thickness of a specimen largely affects the image quality seen with a microscope.

The depth of focus is the distance above and below the image plane over which an image appears in focus. It decreases inversely with the magnification used. A similar parameter, called the depth of field, is the range of distance along the optical axis in which the specimen can move without the image appearing to lose sharpness. This obviously depends on the resolution of the microscope. The forthcoming study of DNA molecules within microfabricated channels used the limited depth of focus determined by the light path of the microscope. It is important to remember that these images are, therefore, a two-dimensional representation of a three-dimensional object. This is an important point when using microfabricated channels that have three-dimensional effects, as will be discussed in chapter 3. Note, confocal microscopy may be used to accurately image these three-dimensional effects if desired. Confocal microscopy visualizes at a two-dimensional cross-section of a three-dimensional image at the depth of focus specified by the user. This technique is often essential when studying protein interactions and cells in-vivo.

1.6.2 Fluorescence Microscopy

Many forms of microscopy have been developed to suit the specialized needs of new scientific fields. In biology, fluorescence microscopy is one of the most widely used techniques utilized for cellular and sub-cellular imaging of molecules such as DNA. Fluorescence is the ability of an object to emit light when excited by incident light of a specific wavelength. During fluorescence, a photon of incident ultraviolet radiation collides with an electron in a specimen atom and excites and elevates the electron to a higher energy level. As the excited electron relaxes to its original lower energy level, it emits a lower-energy photon in the form of an electromagnetic wave with longer wavelength [76], [101].

The goal of fluorescence microscopy is two-fold. The imaging system must first permit excitation light to irradiate the specimen, and second, separate the fluorescent re-radiation from the original excitation light. Only the emission light must reach the eye, or other detector, with sufficient contrast to permit detection. Figure 1-14 pictorially demonstrates how a particular specimen, S, is observed using a fluorescence microscope. Ultraviolet light of a specific excitation wavelength, λ_E, is filtered through an exciter filter and directed onto the sample. Upon illumination, the specimen reflects some of the UV light but also absorbs part of its energy. The absorption causes the specimen to emit light isotropically, in a new fluorescent wavelength, λ_F, that is part of the visible spectrum. The total radiation emitted from the specimen is then filtered via a barrier filter to selectively enhance the visible portion of the fluorescent radiation, λ_F, and simultaneously prevent passage of reflected UV light, λ_E, to the detector, or eye.

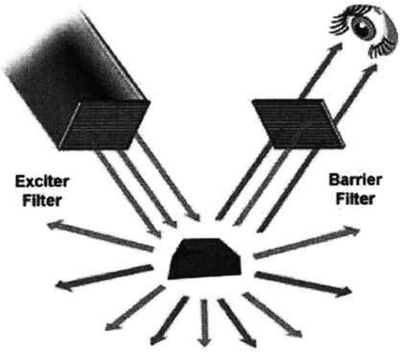

Figure 1-14: Graphical representation of a fluorescing sample observed with a fluorescence microscope.

The use of fluorescent microscopy was truly popularized with the invention of fluorochrome tags to induce secondary fluorescence [102], [103]. The technique utilizes fluorescent tags to stain specific specimens which did not fluoresce on their own. Fluorochromes attached to a particular specimen then produce an image of the specimen conformation when illuminated with the proper excitation light, λ_E. The presence of fluorescing material is determined with extreme sensitivity as specimens stained with as few as 50 molecules of fluorchrome per cubic micron are easily detected.

Many of the images depicting DNA motion have been generated utilizing secondary fluorescence. Austin et al. [104] first illustrated the electrophoretic migration of a 10^{-5}M solution of DNA within an array of microfabricated columns. Here, researchers used ethinium bromide to visualize the dynamics of kilobase length $\lambda-$DNA within the high fields typical of electrophoresis. Similarly, aggregation of larger sized DNA molecules was visualized by Mitnik et al. [43] during pulsed field electrophoresis of a $10^{-5}M$ solution of $\lambda-$DNA. Heller [44] demonstrated the interactions of DNA molecules with the external polymer matrix by utilizing ethinium bromide stains to visualize DNA conformation during electrophoretic migration within capillaries. Additionally, numerous researchers [147], [105] have used secondary fluorescence to study the single-molecule dynamics of DNA within free solution and within micromolded devices. The particular study of DNA within microdevices described in the forthcoming third chapter of this text will similarly utilize secondary fluorescence to visualize the migration of DNA molecules within microfabricated channels. Many of the conclusions derived from fluorescent microscopy studies in this work are obtained from analysis of digital images.

All of the background material detailed in this chapter is used to study new methods in which to improve the separation of DNA molecules within microdevices. In the forthcoming second chapter, properties of the external polymer matrix are studied in order to optimize the gel-loading protocols used in microdevices. In chapter 3, fluorescence microscopy is used to visualize and demonstrate the real-time dynamics exhibited by DNA molecules during conventional sample-loading protocols. These results are then digitized and used to develop an empirical model that relates these dynamics to the results of electrophoretic separations. Additional microscopy experiments have enabled us to capture the migration of DNA samples using ultra-high voltage injections and then correlate these dynamics to the empirical model.

Lastly, the results of these interrelated studies are used in chapter 4 to project the future of the electrophoresis field and describe several emerging research areas that show great potential for the future.

Chapter 2

Study of Gel-Loading Protocols

2.1 Introduction

All electrophoretic channels must be filled with a polymer matrix prior to their use in DNA separations. This process is called gel-loading, and can be accomplished using a variety of protocols. However, the high shear-rates typical of flow within microfabricated channels requires careful inspection of gel-loading protocols. This chapter provides a detailed examination of the gel-loading process in order to understand its effects on the polymer matrix and any subsequent effects on DNA separation.

Entangled solutions of linear polyacrylamide (LPA) are widely used in electrophoresis, performed both in capillaries and microfabricated devices, because of their excellent sieving capacity during DNA separations [117]- [119]. Researchers typically use solutions of unbranched LPA with an average molecular weight of 9 to 13 MDa and concentrations between 2 and 6 weight percent (w/v) [120]. The highly entangled polymer matrix is gel-like with 'pores' between the entanglement points which provide the necessary sieving for DNA separations by molecular size [121]. Video microscopy studies have illustrated how entangled polymer chains of the matrix are actively dragged by DNA molecules during electrophoretic separations [43], [122]. Consequently, the level of chain entanglement in the polymer solution, pore structure and monomer length play a significant role in the mechanism and quality of electrophoretic DNA separations [120], [123], [50].

Currently, there is no standard protocol by which LPA solutions are loaded into electrophoretic channels. Filling may be accomplished manually, through the use of syringes [5], may incorporate automated pumps [57], [124], or the use of vacuum. With any method of filling, however, the narrow gaps of electrophoretic channels produce high shear rates along the channel walls during gel-loading [125]. Such shear rates can affect the strand length and entanglement density of polymer solutions via chain scission or coil disentanglement. Since the LPA matrix creates a network in which DNA molecules are sieved, any distortion or rupture of the polymer chains, and/or their configuration, affects DNA migration within the channel. Molecular degradation of LPA solutions is, therefore, of great practical interest because any change in DNA navigation affects subsequent sequencing analysis. Such shear-induced changes in the viscoelastic properties of an entangled solution can be monitored by rheological observation. For a complete theoretical review, the reader is referred to the texts of Doi and Edwards [126], and Bird, Armstrong and Hassager [159].

Rheology provides a means to extract molecular information about polymer solutions from bulk measurements of the fluid viscoelasticity. Previous work with dilute and concentrated solutions has illustrated how the zero shear-rate viscosity of a polymer matrix, η_0, can be used to identify its molecular weight [128]. For dilute systems, the zero shear-rate viscosity is related to the intrinsic viscosity by a Taylor series expansion [159].

$$\frac{\eta_0}{\eta_s} = \eta_s[1 + [\eta]c + k'[\eta^2]c^2 + ...] \tag{2.1}$$

where $[\eta]$ is the intrinsic viscosity, or limiting viscosity number [127] in units of ml/g, η_s is the solvent viscosity, c is concentration in ml/g, and k' is the Huggins coefficient [159] specific to a given polymer-solvent pair. The intrinsic viscosity can be obtained experimentally using an Ostwald viscometer and is a rheological measure of how a fluid's viscosity increases with its molecular weight. Note, Equation 2.1 is only appropriate to determine the zero-shear-rate viscosity, η_0, for dilute solutions in which $c[\eta] < 1$ [70], [130]. For entangled materials, rheological measurements and theoretical analysis shows that the zero shear-rate viscosity is proportional to the viscosity-averaged-molecular weight, M_v, to approximately the 3.4 power [159].

$$\eta_0 \sim {M_v}^{3.4} \tag{2.2}$$

Viscometric data is thus a very sensitive probe of small changes in the molecular weight of an entangled polymer solution. The molecular weight of a polymer solution provides an estimate for the pore structure and chain disentanglement of the polymer matrix. In particular, the number of entanglement points is given by :

$$N_e = \frac{M_w}{M_e} \tag{2.3}$$

where M_e, is the entanglement molecular weight, defined as the molecular weight between entanglement points [126]. This value is approximately 10^5 Da for an LPA concentration of 11% [131]. Since electrophoresis depends on the number and size of pores between entanglement points [50], monitoring changes in polymer molecular weight can determine changes to these parameters. In the present study, we relate the zero shear-rate viscosity, η_0, to the molecular weight through experimental calibration, as will be described in the materials section.

The current study describes experiments performed using an automated syringe pump for gel-loading. Here, 2% and 3% (w/v) concentrations of unbranched LPA solutions, of 9 MDa molecular weight disolved in water, were loaded into 12-cm-long capillaries of 50-μm and 75-μm internal diameters. Given these dimensions, the polymer volume within a filled capillary is 0.23 μl and 0.53 μl respectively. The polymer matrixes were loaded into the channels at measured fill times between 1 second and 2 minutes. It is useful to convert each fill time into an average volume flow rate, Q. An imposed flow rate of 1 μl/min, for example, means that the polymer volume within a 12-cm-long-capillary is replaced twice per minute. Although flow rates used during gel-loading are generally not reported in the literature, using a timer we estimated that reasonable fill times for a 12-cm-long channel lie between 30 and 90 seconds, corresponding to a flow rate of $\sim 15\mu$l/min. For completeness, rheology data for flow rates ranging between 1 μl/min and 33 μl/min will be discussed.

The tests in the present work quantify polymer degradation by relating the zero shear-rate viscosity, η_0, to the viscosity-averaged molecular weight, M_v, before and after gel-loading. Molecular weight averaging is needed for polydisperse solutions since typical samples of linear macromolecules have a distribution of molecular weights as a consequence of their chemical synthesis. Unlike the more conventional number-averaged molecular weight, M_n, and weight-averaged molecular weight, M_w, the viscosity-averaged molecular weight, M_v, is a polynomial average related to the hydrodynamic volume of the chain.

$$M_v = \left(\frac{\Sigma w_i M_i^a}{\Sigma w_i}\right)^{1/a} \tag{2.4}$$

where w_i is the fraction of strands of degree of polymerization i, M_i is the individual molecular weight of a polymer strand i and a is the polymer-specific exponent from the Mark-Houwink-Sakurada equation [84]. The heterogeneity index, (M_w/M_n), is often used as a measure of the polydispersity of a solution. Equation 2.4 is valid for polymer solutions with $(M_w/M_n) < 3$ and peak molecular weights between 10^2 and 10^8 Da [84]. The LPA solutions used in this study fall within these limits with heterogeneity index $(M_w/M_n) < 2$ and peak molecular weights of order 10^7 Da [131].

The viscometric properties of each collected polymer sample were measured using a cone and plate rheometer. In order to correlate the rheological results to DNA sequencing analysis, LPA solutions in which degradation was identified were used as separation matrices during electrophoresis performed on 12-cm-long microfabricated channels. The increases in peak widths and decreases in electrophoretic resolution between the degraded and non-degraded LPA solutions are correlated to the decrease in molecular weight as a result of shear-induced degradation.

2.2 Theory

2.2.1 Shear-rates

LPA solutions used for electrophoretic DNA separations are typically entangled solutions, where individual molecules interpenetrate forming entanglements. In a basic polymer system, macromolecules are separated by large distances that minimize individual interactions between the molecules. In more complex systems, macromolecules are highly entangled and interact with one another so strongly that the contributions of individual macromolecules are hard to distinguish [89]. At low polymer concentrations, solution properties are determined by the properties of individual macromolecules and the solutions are classified as dilute. With increasing concentration, polymer coils begin to overlap forming semi-dilute, and eventually concentrated, solutions.

A parameter called the overlap threshold, or crtical concentration, c^*, denotes the region where polymer molecules just begin to interact. Solutions of concentrations greater than c^* are considered semi-dilute. As the polymer coils continue to overlap and interpenetrate, a new parameter called the entanglement concentration, $c^\dagger$, defines the region of concentrated solutions [133]. Scaling arguments show that the entanglement concentration, $c^\dagger$, is independent of molecular weight for $M_v \geq M_e$. For LPA solutions with molecular weights within 9-13 MDa, the critical concentration, c^* has been experimentally verified as 0.1% [131] while the entanglement concentration, $c^\dagger$, is approximately 10% [131]- [133]. LPA solutions of 2% and 3% (w/v) typically used for DNA separations are therefore within the semi-dilute, entangled regime [70].

During gel-loading, LPA solutions are exposed to large shear stresses as they are forced under pressure into microfabricated channels or capillaries. The resulting effect of the shear stress depends upon the types of flow which occur during LPA injection. A typical gel-loading protocol may inject LPA solutions into capillaries by using a small syringe for example. In such an instance, LPA is ejected from a 500-μl syringe with needle diameter 350 μm, into an electrophoretic channel of diameter 75 μm; forcing the polymer through an area contraction of 22:1. Flows through such contractions are classified as Fast Transient Flows (FTF), and are well documented to result in polymer degradation independent of specific nozzle geometry [136]. Further, once inside the electrophoretic channel, the polymer solution is forced along the channel under constant pressure gradient. During this process, the solution experiences a steady shearing flow with a distribution of shear rates increasing from zero at the centerline, to a maximum at the channel walls [159]. Numerous papers show that high molecular weight polymers are easily fractured in such common pure shear flows configurations [137]- [140]. The shear rate imposed during this gel-loading is of the order:

$$\dot{\gamma} \equiv (\frac{dv_z}{dr}) \sim \frac{Q}{\pi R^3} \tag{2.5}$$

where Q is the volume flow rate, and R is the channel radius. For the flow rates and channel sizes discussed above, shear rates in the range $10^2 \leq \dot{\gamma} \leq 10^3 \ s^{-1}$ can be experienced.

2.2.2 Non-Newtonian Viscosity

The viscosity, η, of an entangled polymer solution is a strong function of the shear rate since the orientation of polymer segments and the number of entanglement points in the material depends on the externally applied load. The shear-rate dependent viscosity, $\eta(\dot{\gamma})$, is a viscometric material function that can be determined using a plate and cone rheometer. In this device, the polymer solution is placed within the thin gap formed between an inverted cone and plate as the cone is rotated at different angular velocities. For small cone angles, a homogeneous shear flow develops in the gap and by varying the imposed torque, the viscosity as a function of shear rate, $\dot{\gamma}$, or shear stress, τ is obtained [159].

A typical viscosity profile for a 2% LPA solution generated by a cone and plate rheometer is shown in Figure 2-1. The figure displays two curves, upper and lower, of an LPA solution dissolved in buffer [5], and de-ionized water respectively. Each curve displays experimental viscosity values for shear rates spanning six orders of magnitude. Typically the non-Newtonian viscosity has three characteristic regions: a low shear-rate plateau, a shear thinning region and a high shear-rate plateau.

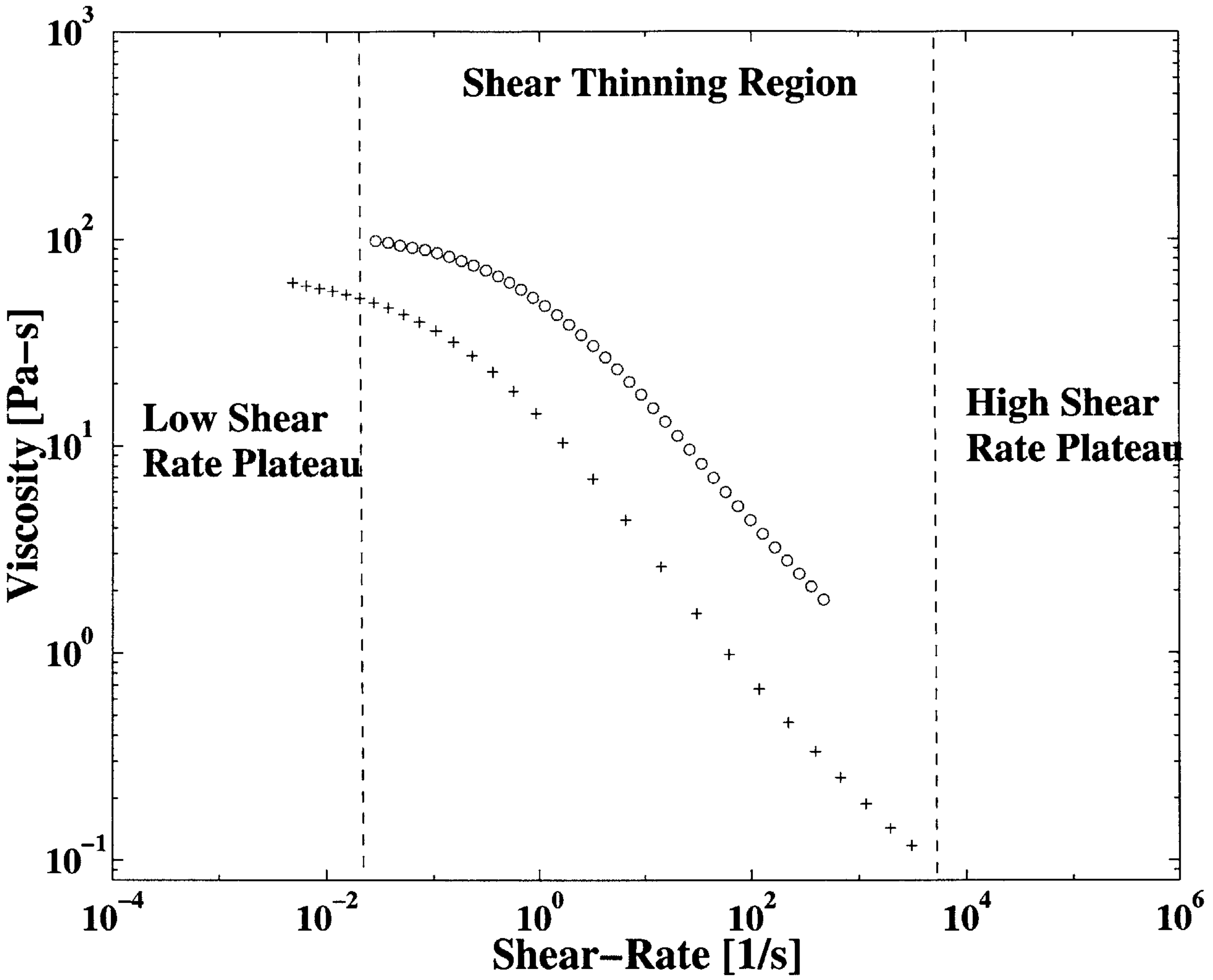

Figure 2-1: Characteristic non-Newtonian viscosity profiles for a 2% (w/v) LPA solution of 2.2 [MDa] molecular weight. The lower curve illustrates viscometric measurements for a solution of LPA dissolved in de-ionized water at 25^0C, while the upper curve illustrates viscometric data for a solution of LPA dissolved in a 1 x TBE separation buffer(90 mM Tris/64.6 mM boric acid/2.5 mM EDTA). The low shear-rate, shear thinning, and high shear-rate regions are identified. Note, data in the high shear-rate region is generally unobtainable as shear-rates greater than $10^4 s^{-1}$ are required.

The low shear-rate plateau corresponds to viscosity values obtained below shear rates of $\dot{\gamma} \sim \lambda^{-1}$ where λ is a characteristic measure of the fluid relaxation time. The limiting viscosity value, corresponding to low shear rates, is called the zero shear-rate viscosity, η_0, and is defined by:

$$\eta_0 = \lim_{\dot{\gamma} \to 0} [\eta(\dot{\gamma})] \tag{2.6}$$

The zero shear-rate viscosity, η_0, provides a measure of the fluid rheology under near equilibrium conditions and is correlated to the molecular weight of the polymer through theory and calibration [128]. The infinite shear-rate viscosity, found at very high shear rates, is usually close to the solvent viscosity. The shear-thinning region in between the maximum and minimum viscosity typically exhibits a power-law decrease in the viscosity with increasing rate [159]. Graessley's entanglement theory attributes the non-Newtonian viscosity behavior to the effect of shear rate on entanglement density [70]. As shear rate is increased, polymer chains become increasingly disentangled resulting in lower viscosities. The point of transition from the low shear rate plateau to the shear thinning region occurs at a critical shear rate, $\dot{\gamma}_{crit}$, which is the the reciprocal of the relaxation time, λ. At low concentrations, the critical shear-rate is roughly independent of concentration and scales as [159]:

$$\dot{\gamma}_{crit} \sim \frac{1}{\beta} \sim \frac{RT}{[\eta]\eta_s M} \tag{2.7}$$

where $[\eta]$ is intrinsic viscosity, defined from Equation 2.1, η_s is the solvent viscosity, M is the molecular weight, R is the universal gas constant, and T is temperature. At higher concentrations. $\dot{\gamma}_{crit}$ correlates linearly with the product of concentration and viscosity averaged molecular weight, M_v [159]. Higher values of critical shear-rate correlate with solutions of increased polydispersity.

The variation in the viscosity of a non-Newtonian fluid can be characterized by a number of simple models. For engineering work, the shear thinning region is often described by a power-law expression of the form:

$$\eta = m(\dot{\gamma})^{n-1} \tag{2.8}$$

where η is the solution viscosity, $\dot{\gamma}$ is the shear rate in units of s^{-1}, m is a polymer specific constant (often called the consistency index) with units of Pa- s^n and n is a dimensionless exponent specific to a particular polymer solution. For LPA dissolved in de-ionized water, these specific parameters have been experimentally calculated as 0.766 Pa- s^n and 0.326 respectively for molecular weights greater than 10^5 Da [134].

Another model commonly used in rheology is the Carreau model [159]. The Carreau model is a 5 parameter model which incorporates the critical shear rate of the polymer in its calculation of solution viscosity, η.

$$\frac{\eta - \eta_s}{\eta_0 - \eta_s} = \frac{1}{[(1 + (\lambda\dot{\gamma})]^{2\,\frac{1-n}{2}}} \tag{2.9}$$

where η_0 represents the limiting viscosity at zero shear-rate, η_s represents the solvent viscosity, $\lambda = (\dot{\gamma}_{crit})^{-1}$ is the critical shear rate for onset of shear thinning, and n is the exponent for the shear thinning region. In the present work we regress our experimental measurements of $\eta(\dot{\gamma})$ to Equation 2.9 and evaluate the degradation in the molecular weight in terms of the variation in η_0 and $\dot{\gamma}_{crit}$.

2.2.3 Effects of Shearing

Many equations which define and relate characteristic parameters of an entangled polymer network to specific properties of the polymer chains are only applicable for near equilibrium conditions. As a result, equations which define network properties such as the distance between entanglement junctions, network chain length and so on, neglect the effects of imposed shear. For instance, in concentrated solutions the distance between two entanglement points is characterized by an average mesh size, ζ. A generalized formula for the mesh size of an entangled solution was proposed by Cottet et.al. [135]:

$$\zeta = 1.43 \left(\frac{k^{\frac{3}{2}}}{6} c^* \right)^{\frac{1}{3a}} \left(\frac{3}{4\pi N_A c} \right)^{\frac{a+1}{3a}} \tag{2.10}$$

where k and a are the characteristic polymer-solvent parameters used in the Mark-Houwink Sakurada Equation, c^* is the critical concentration, c is the solution concentration and N_A is Avagadro's number. This expression indicates that the mesh size of a polymer network is dependent only upon solution concentration and implies that two entangled solutions with $M_w >> M_e$, of the same polymer and concentration, have the same mesh size regardless of their molecular weights. However, the Cottet and Viovy equation was derived for polymers in the unperturbed state. The shear-induced degradation effects on LPA solutions resulting from gel-loading make it inappropriate to rely upon such equations for near equilibrium conditions.

Shear imposed on polymer strands can cause coil disentanglements or chain scission, both of which severely distort the matrix mesh size and number of entanglements, thus affecting DNA migration and separation. Electrophoretic studies of DNA separations using low molecular weight polymer solutions, or solutions which were not well entangled, reveal increased peak widths in the resulting electrophoregrams [120], [123], [50]. Further, disentangled polymer strands allow electrophoretic motions of DNA within the matrix which would otherwise be restricted [50]. Changes in the molecular structure of the sieving matrix can be detrimental to separations as evidenced by video-microscopy studies [43], [122] which illustrate how DNA molecules actively drag surrounding polymer chains during electrophoresis. To resist such deformations, the matrix chains must be well-entangled. The referenced experiments highlight how shear induced degradation of the polymer matrix during gel-loading may reduce the resolution and quality of separations.

Although shear imposed during gel-loading may result in temporary chain disentanglement, chain scission, or both, each effect will degrade the molecular weight and the entanglement density of the polymer solution. To quantify these effects, we define the percentage molecular degradation, D_p, for a sheared polymer solution. The quantity, D_p, refers to the shear-induced degradation of a polymer's viscosity-averaged molecular weight, M_v, during gel-loading and is defined as:

$$D_p = \frac{M_v|^o - M_v|^f}{M_v|^o} \times 100\% \tag{2.11}$$

where $M_v|^o$ represents the viscosity-averaged molecular weight of the original polymer solution and $M_v|^f$ represents the final viscosity-averaged molecular weight of the polymer following shearing. Since viscosity scales with molecular weight to the 3.4 power [159], small changes in molecular weight translate into large changes in viscosity. By using the viscosity averaged molecular weight, the effects of polymer chain disentanglements and chain scission can be seen by a decrease in the solution viscosity. Note, by its definition, the percent molecular degradation, D_p, will measure a reduction in the viscosity-averaged molecular weight of the polymer solution whether it is solely a result of chain disentanglement, chain scission, or a combination of both. To identify which effect is prevalent, additional techniques not incorporated in this study, such as light scattering or Gel Permeation Chromatography (GPC), provide a more detailed analysis of the full molecular weight distribution.

Scaling arguments can be used to provide a more physical understanding of the defined quantity percent degradation, D_p. If one assumes the effects of shear-induced degradation lie solely in the lengths of the polymer strands, values of D_p can be correlated to these chain lengths. The weight average molecular weight of a polymer solution is defined as [159]:

$$M_w = \Sigma(x_i M_i) M_i = x_i M_i^2 \tag{2.12}$$

where M_i is the molecular weight and x_i is the fraction of chains with molecular weight M_i. The model of entangled polymer solutions [89], [91] illustrates that molecular weight, M_i, is proportional to the chain length, L_i. Using this scaling, percent degradation, D_p, can be expressed in terms of the different polymer lenghts, L_i, within the solution before and after shearing.

$$D_p = \frac{M_i|^0 - M_i|^f}{M_i|^0} \times 100\% = \frac{\Sigma(x_i L_i^2)|^0 - \Sigma(x_i L_i^2)|^f}{\Sigma(x_i L_i^2)|^0} \times 100\% \tag{2.13}$$

It is clear from Equation 2.13 that percent degradation values do not scale directly with the lengths of the degraded chains. There is no linear relation because polymer chains are not always degraded nor must they always degrade to the same length. Thus, a 50% degradation value does not mean that all polymer chains are broken in half. In fact, using Equation 2.13, a much higher degradation value of 75% is obtained for such a case.

The effect of shearing in a capillary are further complicated by the fact that the flow is spatially non-homogeneous. Solving the equations of motion reveals that the shear stress, τ, varies linearly from zero along the centerline to a maximum value at the wall [125]. Since the shear-dependent viscosity of an entangled polymer solution is a strong function of the imposed deformation rate, the familiar parabolic velocity profile expected for a Newtonian fluid is also modified. By substituting an appropriate constitutive relation such as the power-law of Equation 2.8, the modified profile can be determined. For a shear thinning fluid, the shear rate is highest and hence the viscosity is lowest, near the wall. The resulting velocity profile is 'plug like' with shearing effects confined to regions near the no-slip boundaries of the channel, i.e. the walls.

Using the power-law constitutive model for a shear-thinning fluid, an analytical expression for steady, fully developed flow through a circular channel can be obtained [159]. In particular, the shear stress at the wall τ_w is found to be:

$$\tau_w = \eta(\dot{\gamma_w}) \left[\left(\frac{Q}{\pi R^3} \right) (3 + 1/n) \right] \tag{2.14}$$

where $\eta(\dot{\gamma_w})$ is the viscosity evaluated at the wall, $\dot{\gamma_w}$ is the shear rate at the wall, Q is the volume flow rate, R, the channel inner radius, and n is the exponent for the shear thinning region. The shear-rate is largest at the wall and the ratio of the wall shear-rate, $\dot{\gamma}_w$, to the average, $< \dot{\gamma} >$, is:

$$\frac{\dot{\gamma_w}}{< \dot{\gamma} >} = \frac{\dot{\gamma_w}}{\frac{Q}{\pi R^3}} = (3 + 1/n) \tag{2.15}$$

as n decreases it is clear that the local shear-rate near the wall becomes increasingly large. The analytical expression for shear stress, indicates that values of shear rate at the wall, $\dot{\gamma_w}$, and shear stress at the wall, τ, during gel-loading are on the order of 10^2 - 10^3 s^{-1} and 10^5 - 10^6 Pa respectively. Note, previous work indicates that even stresses less than 10^4 Pa result in the shearing of high molecular weight polymers [138].

2.2.4 Electrophoretic Analysis

The performance of any electrophoretic procedure depends upon the inter-band spacing and peak widths [88]. Selectivity is a measure of the relative difference in analyte mobility and is determined from the electrophoregram inter-band spacing. Resolution, R_L, is a measure of the separation capacity and is determined by the peak widths and spacing on the electrophoregram. It is defined as:

$$R_L = 2\sqrt{2ln2}\frac{\Delta t_R}{(W_{h1} + W_{h2})} \tag{2.16}$$

where t_R is the retention time in seconds, and W_{h1} and W_{h2} represent the peak widths at half maximum between 2 successive peaks, also measured in seconds. The effects of any shear-induced degradation of LPA during gel-loading can be quantitatively measured from the loss in resolution between electrophoretic runs. As the molecular weight of a polymer solution is decreased due to shearing, the number of entanglements is also decreased, as is the length of the chains in the case of chain scission. Although these effects do not alter the solution pore size above the critical concentration, they do affect the sieving properties of the polymer. The result is wider peak widths during separations and subsequently lower resolution values [123], [50].

2.3 Experiments

2.3.1 Synthesis and Calibration of LPA Separation Matrices

LPA powders (Poly Science Standards) of 1.1, 4.36, 8.78, and 12.1 MDa were slowly dissolved in de-ionized (DI) water to obtain 2% and 3% (w/v) solutions for gel-loading. The viscosity averaged molecular weight, M_v, of each polymer sample at 25^0C was determined using an Oswalt viscometer. This device measures the intrinsic viscosity, $[\eta]$, of the sample which when combined with the Mark-Houwink-Sakurada equation [159], yields the molecular weight. For LPA, the Mark-Houwink-Sakurada constant, k, is 0.00631 ml/g and the dimensionless exponent, a, is 0.755 [134]. The viscosity data of these solutions, η_0, was used to generate a separate molecular weight calibration curve for each concentration of LPA. Each curve was then fitted with a power-law relation to facilitate calculations of percent degradation, D_p. Note, although LPA solutions of various molecular weights were used for calibration

Table 2.1: Experimentally calculated parameters used for the calibration of viscosity-averaged molecular weight, M_v, and zero shear-rate viscosity, η_0.

Solution(%)	C_1	C_2
2 %	0.708	2.44
3 %	1.44	3.16

purposes, only LPA solutions with a viscosity-averaged molecular weight of 9.0 MDa were used for degradation experiments.

For electrophoretic results, high-viscosity-averaged molecular weight LPA (9 MDa) powder was synthesized in-house according to the procedure described by Goetzinger et. al. [141]. LPA solutions were prepared using 1 x TBE (90 mM Tris/64.6 mM boric acid/2.5 mM EDTA) with 3.5 M urea/30% (v/v) formamide or with 1 x TTE (50 mM Tris/50 mM TAPS/2 mN EDTA) with 7 M urea. The solutions were ready for use after 3 days of slow stirring in a glass jar.

Five measurements per sample were averaged to obtain M_v for calibration. The variation in molecular weight calculations was less than 1 % for each sample.

$$\eta_0 = C_1 M_v^{C_2} \tag{2.17}$$

where η_0 is the zero shear-rate viscosity in Pascal-seconds, Pa-s, C_1 is a constant measured in Pascal-seconds, and C_2 is a dimensionless exponent. Viscosities of polymer samples were correlated to their corresponding molecular weights, before and after gel-loading. LPA solutions used for degradation experiments had original viscosity-averaged molecular weights of 9.0 MDa.

2.3.2 Micromachining

The design of the microdevice used for DNA separations and the laser induced fluorescence (LIF) detection system have both been described previously [5]. Electrophoretic microdevices were made from 150-mm-diameter glass wafers (Corning, Corning, NY) using techniques described in the literature [5]. The device uses a cross injector for sample introduction with a hemispherical separation channel 11.5 cm in length, 40 μm deep and 90 μm wide. The side channels forming the injector were 2.5 mm in length and horizontally offset by 250 μm. Glass reservoirs (Ace Glass, Vineland, NJ) of 50 μl volume were affixed around the channel access holes to hold the sample and buffer. Channel inner surfaces were coated with LPA using a modified Hjerten procedure [54].

2.3.3 Electrophoresis

Between each run, the separation and cross injector channels of the device were simultaneously refilled with fresh LPA solutions from the anodic end of the separation channel using a gas-tight syringe. The electrophoresis buffer composed of 1 X TTE was also changed after each run. Pre-electrophoresis was performed at 55^0C for 3 minutes at 200 V/cm. The DNA sequencing samples were loaded applying a negative potential of 1500 V (300 V/cm) to the sample reservoir with the waste reservoir at ground and the buffers in both the anode and cathode reservoirs left floating. Leakage of excess sample from the loading procedure into the separation channel during the run was prevented with a small electric field ($\sim$ 20 V/cm) applied to both halves of the loading channel.

2.3.4 DNA Sequencing Reactions

DNA sequencing reactions were conducted using standard cycle sequencing chemistry with AmpliTaq-FS and Big-Dye-labeled M13 universal primers (Applied Bio-systems/Perkin Elmer Corp., Foster City, CA) and M13mp18 as template (New England Biolabs, Beverly, MA). A total of 0.4 μg of template DNA was used per sample (0.1 μg of M13mp18 per single color reaction). Cycle sequencing was performed on a Genius thermo-cycler (Techne, Duxford, Cambridge, UK) consisting of 15 cycles of 10 seconds at 95^0C, 5 seconds at 50^0C and 1 minute at 70^0C, followed by 15 cycles of 10 seconds at 95^0C and 1 minute of 70^0C.

2.3.5 Sequencing Sample Purification

The DNA sequencing samples were desalted using Centri-Sep spin columns (Princeton Separations, Adelphia, NJ). The spin columns were hydrated for at least 30 minutes by adding 800 μL of de-ionized water. The interstital volume was excluded by spinning the columns for 3 minutes at 3000 rpm. The sequencing sample was diluted in 40 μL of de-ionized water and then placed in the column and spun for 3 minutes at 3000 rpm. The resulting sample volume was diluted to 50 μL with deionized water, and a 10-μL aliquot was then pipetted onto the electrophoretic device.

2.3.6 Data Analysis

The C-traces of four-color DNA sequencing reactions using (-21M13) forward BigDye primers were used for data analysis. The C-traces were selected due to miminal cross-talk and ease of tracking single isolated peaks over the entire range of fragment sizes. From the resulting electrophoregrams, the migration time of the sequencing fragments versus base pair number were plotted and curved fitted with a third order polynomial using Microcal Origin 6.0 software (Microcal Software Inc., Northampton, MA). The fitted values were used to calculate resolution as defined previously in Equation 2.16.

2.3.7 Experimental Procedure

The apparatus shown in Figure 2-2 simulates a gel-loading protocol using automated pumping. The apparatus consists of a syringe pump [Harvard Apparatus, Harvard, MA], a 500-μl-gas-tight syringe [Hamilton, Reno, NV], uncoated fused silica capillaries [Poly-micro Technologies, Phoenix, AZ], stainless steel tees, ferrules, and plastic collection vials. LPA solutions of 2% and 3% (w/v), dissolved in de-ionized water and molecular weight 9 MDa, were pumped through 12 cm of 50-μm and 75-μm-internal diameter (i.d.) capillaries at different fill rates, and collected into plastic vials for viscosity testing.

To select appropriate volume flow rates, we estimated reasonable fill times for 12-cm-long channels. As mentioned earlier, these fill times were converted into volume flow rates using the microliters of LPA injected into each channel. Flow rates for this study ranged between 1 μl/min and 33 μl/min corresponding to average wall shear rates, $\dot{\gamma_w}$, of 10^2 and 10^3 s^{-1} respectively as seen from Equation 2.5. The flow rate of 1 μl/min was the minimum rate attainable using automated pumping, while the maximum rate of 33 μl/min was chosen as a worst case representation of manual gel-loading. Due to the large range of flow rates studied, throughout the remaining sections the volume flow rate of 15 μl/min is referred to as the 'typical' or 'average' rate during gel-loading.

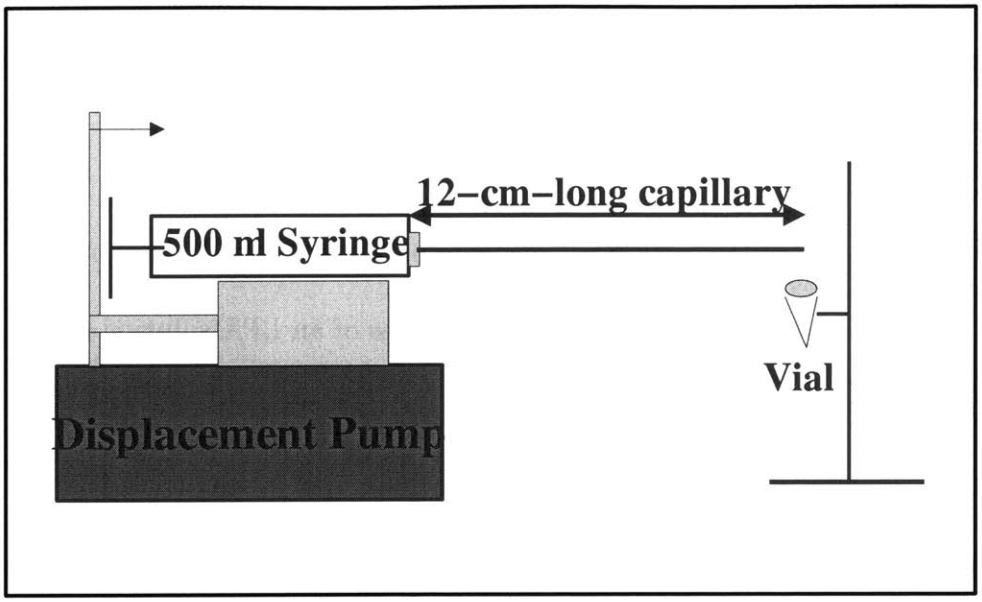

Figure 2-2: Schematic of experimental apparatus used to gather LPA solutions as they were loaded into electrophoretic channels at different flow rates.

The non-Newtonian viscosity profile of each collected polymer sample was analyzed using a commercial cone and plate rheometer [AR 1000-N, TA Instruments] with torques in the range 10 - 1000 μNm. To enable further study, the same LPA solutions were later used as sieving matrices for DNA separations. For these later experiments, LPA solutions were loaded into microfabricated channels using the same apparatus and identical flow rates.

2.4 Results

2.4.1 Effects in polymer samples of 2% and 3% LPA

Figure 2-3 depicts the non-Newtonian viscosity profiles of an LPA solution after it has been pumped through a 12-cm-long capillary of 50-μm-i.d. at different flow rates. Similarly, Figure 2-4 depicts the non-Newtonian viscosity profiles of an LPA solution after it has been pumped through a 12-cm-long capillary of 75-μm-i.d. at different flow rates. The solution shown is a 3% (w/v) LPA solution, dissolved in de-ionized water with 9 MDa molecular weight. The uppermost curve is the viscosity profile of the original LPA solution loaded at the lowest flow rate, while the remaining curves represent the profiles of each polymer sample loaded into the capillary at increasing flow rates. All data was gathered at 25^0C with less than 0.7^0C variation as measured by the rheometer. The measurements show that each curve retained the shape of the original viscosity profile but displayed much lower values of viscosity at every shear rate. It is also seen that the zero shear-rate viscosity, η_0, of each loaded polymer solution decreased as the fill rate was increased. If no molecular degradation were present, the viscosity profile of each polymer sample would be identical. Yet the behavior shown in Figure 2-3 indicates shear-induced degradation is present at every fill rate during gel-loading. As seen from the definition of viscosity-averaged molecular weight, M_v, in Equation 2.4, the measured decreases in viscosity indicate chain disentanglement, coil fracture, or combinations of both, are present during gel-loading. Further, the lower values of viscosity corresponding to polymer samples loaded at higher flow rates indicate shearing effects increase with increased gel-loading rates. In such a sheared polymer solution, not only are the viscosity and average molecular weight decreased, but the strand length, pore size, and distribution functions of each are also affected [50]. Changes in such parameters will generate substantial differences in the entanglement density and network pore size of the original sieving matrix, thereby influencing DNA migration within the LPA solution.

Figure 2-5 ad Figure 2-6 show the viscosity profiles of the same 2% (w/v) LPA solutions loaded through a 50-μm-i.d and 75-μm-i.d. capillary, respectively, at different pump speeds. The curves in this figure reveal the same trend as the previous figure where all curves retain the shape of the non-sheared LPA sample viscosity profile, but display lower values of η_0 as the flow rate is increased.

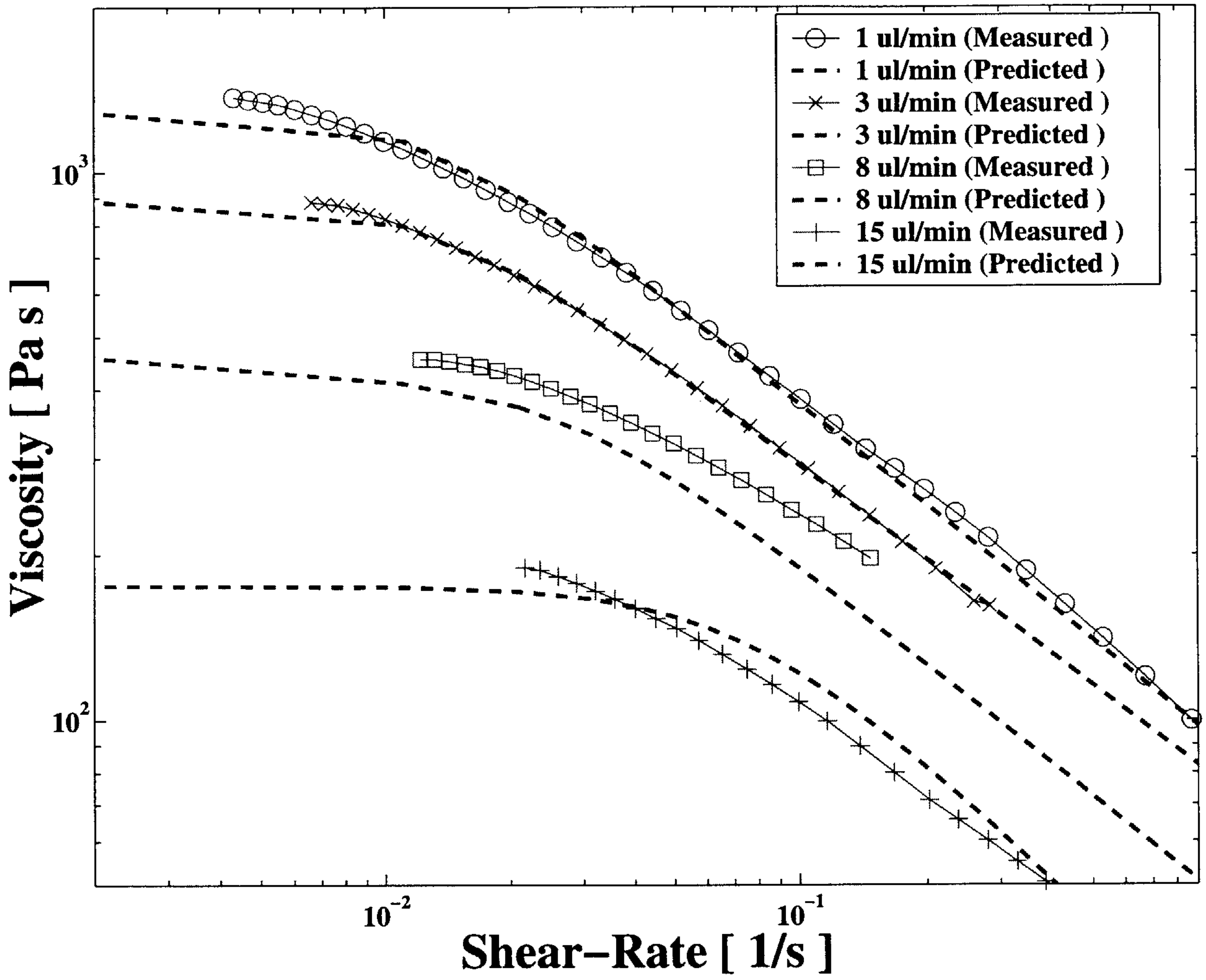

Figure 2-3: Non-Newtonian viscosity profiles of 3% (w/v) LPA solutions at 25^0C after gel-loading was performed within a 50-μm-i.d. capillary at different volume flow rates. The polymer solution shown was dissolved in de-ionized water and of molecular weight 9 MDa before gel-loading. The symbols represent viscosity data gathered using the rheometer while the dashed lines represent the viscosity predictions of the Carreau model for each flow rate.

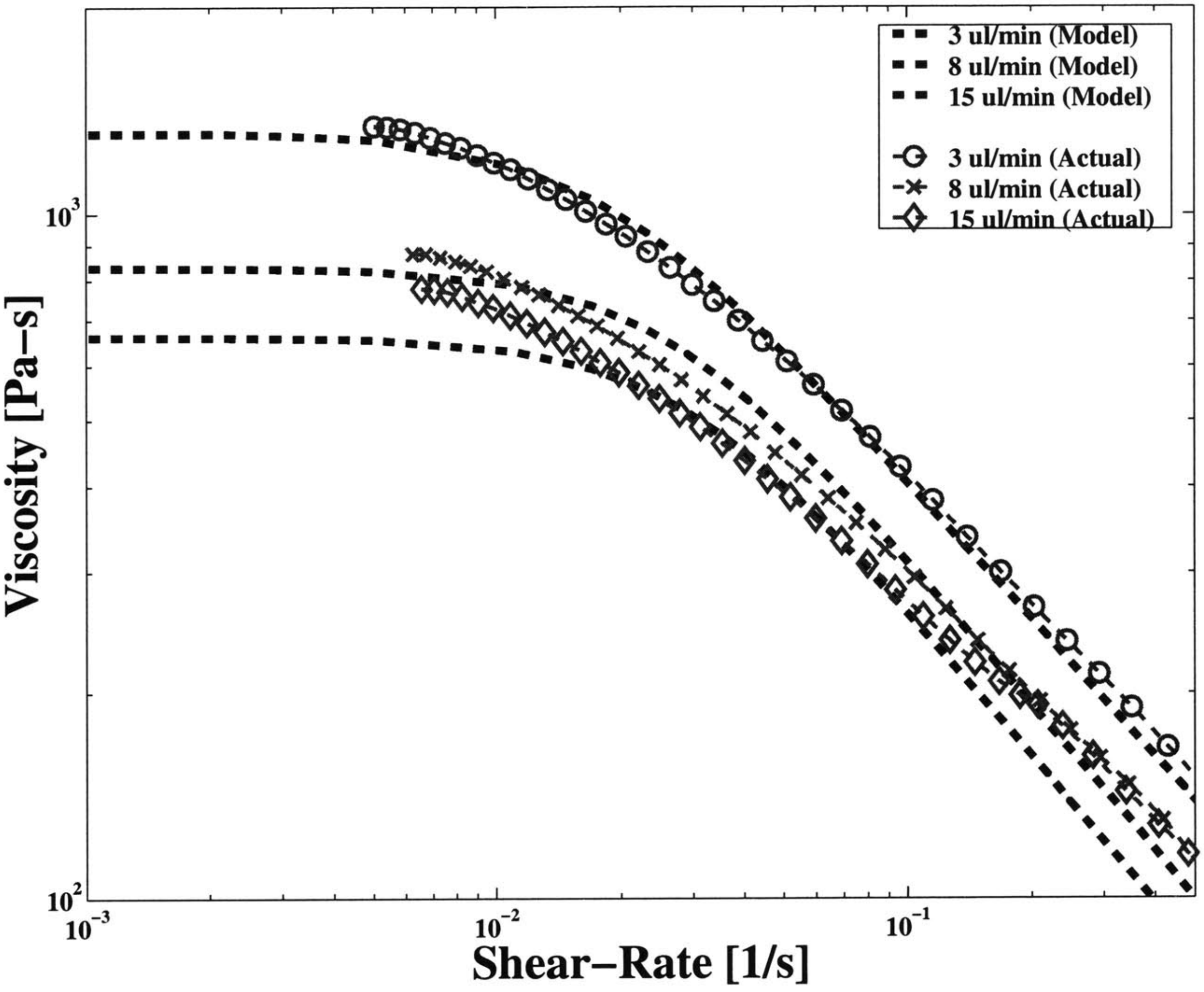

Figure 2-4: Non-Newtonian viscosity profiles of 3% (w/v) LPA solutions at 25^0C after gel-loading was performed within a 75-μm-i.d. capillary at different volume flow rates. The polymer solution shown was dissolved in de-ionized water and of molecular weight 9 MDa before gel-loading. The symbols represent viscosity data gathered using the rheometer while the dashed lines represent the viscosity predictions of the Carreau model for each flow rate.

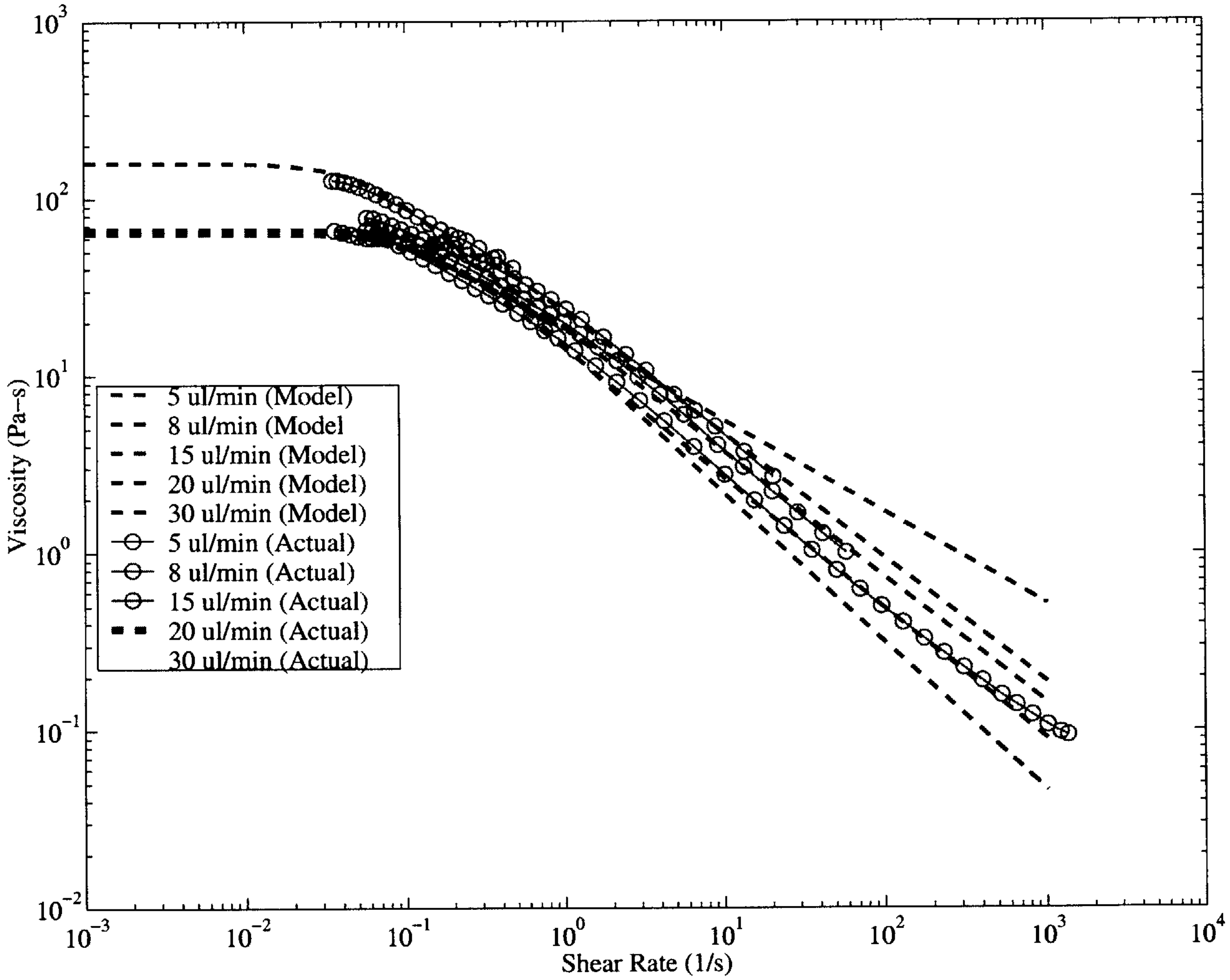

Figure 2-5: Non-Newtonian viscosity profiles of 2% LPA solutions at 25^0C after gel-loading was performed at different volume flow rates. The curves represent the viscosity profiles of the polymer after it has been loaded into 50-μm-i.d. capillaries.

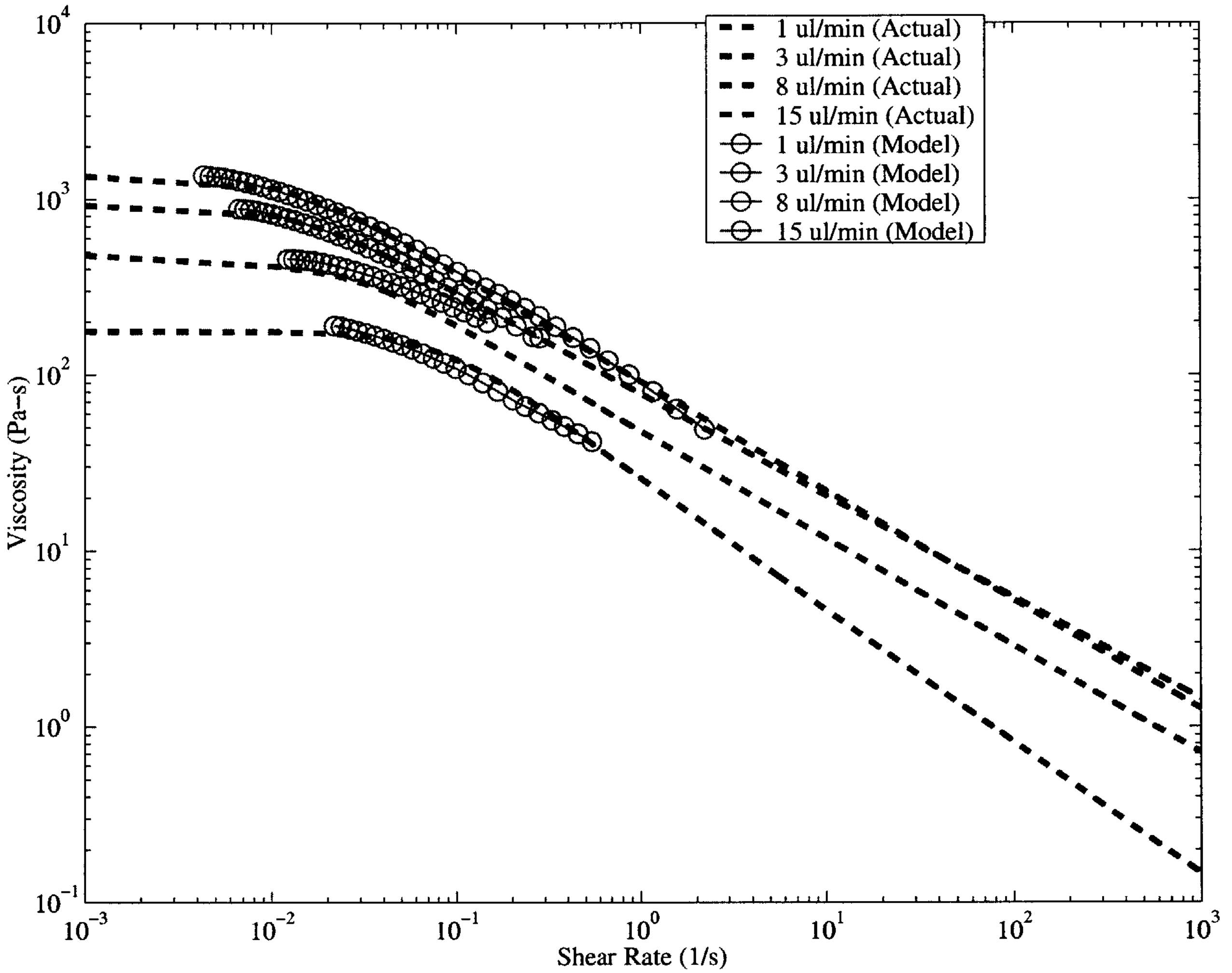

Figure 2-6: Non-Newtonian viscosity profiles of 2% LPA solutions at 25^0C after gel-loading performed at different volume flow rates. The curves represent the viscosity profiles of the polymer after it has been loaded into 75-μm-i.d. capillaries.

Via calibration, the zero shear-rate viscosity, η_0, of each polymer solution following gel-loading was used to determine the new viscosity-averaged molecular weight, M_v, of the shear-degraded polymer. Note, it is difficult to obtain viscosity data in the zero shear-rate region because of the difficulty in obtaining shear rates below $10^{-2}\ s^{-1}$ experimentally for high molecular weight polymers. Further, the viscosity curves shown in the figure begin with different shear rates due to minimum torque constraints. The minimum obtainable torque, T_{min}, for any experiment, using the commercial rheometer is 0.1 μN-m. Hence, as the zero-shear-rate viscosity of a polymer sample decreases, the minimum obtainable shear-rate must increase to maintain the 0.1 μN-m minimum torque criteria:

$$T_{min} = [\tau_{min}]\frac{2\pi R^3}{3} = [\eta(\dot{\gamma}_{min})\dot{\gamma}_{min}]\,\frac{2\pi R^3}{3} \tag{2.18}$$

As a result, viscosity measurements of the samples with lower molecular weight begin with higher shear-rates.

To insure that the viscosity measured at the lowest attainable shear rate was representative of the zero-shear rate viscosity, all of the values of η_0 calculated experimentally were compared to those predicted by the Carreau model described in Equation 2.9. The values of zero shear-rate viscosity predicted by the model were within 8% of the η_0 values obtained experimentally using the rheometer. Thus, the viscosity data obtained experimentally for shear rates of order $10^{-2}\ s^{-1}$ were good estimates of the zero shear-rate viscosity, η_0. The Carreau model is curve-fitted to the experimental data in Figure 2-3 and is represented by dashed lines.

Rather than show the viscosity profiles of each experiment, Tables 2.2 and 2.3 summarize

Table 2.2: Experimental values of non-Newtonian viscosity, η_0, viscosity averaged molecular weight, M_v, and percent degradation, D_p, for 2% (w/v) LPA solutions (disolved in deionized water with original molecular weight of 9 MDa) loaded into 50-μm-i.d. and 75-μm-i.d. capillaries at varying flow rates and 25^0C.

Q (μl/min)	η_0^{50} (Pa-s)	M_v^{50} (MDa)	D_p^{50} (%)	η_0^{75} (Pa-s)	M_v^{75} (MDa)	D_p^{75} (%)
3	129.4	8.41	4.16	–	–	–
8	77.6	6.82	22.35	121.5	8.19	6.72
15	62.06	6.33	27.96	105.6	7.73	11.90
20	55.37	5.95	32.17	77.73	6.82	22.32
33	47.88	5.17	41.12	50.19	5.59	36.33

the parameters of interest to this study: zero shear-rate viscosity, η_0, viscosity averaged molecular weight, M_v, and molecular degradation, D_p. Table 2.2 illustrates the changes in the molecular weight experienced by a 2% LPA solution when loaded into a 50-μm and 75-μm-i.d. capillary at different flow rates. Using the 50-μm capillary, the molecular weight of the polymer decreased by 4% when the solution was loaded at a flow rate of 3 μl/min, but decreased by 41% when loaded at the maximum rate of 33 μl/min. Similarly, in the 75-μm capillary, a fill rate of 8 μl/min resulted in a 7% decrease in molecular weight while a volume flow rate of 33 μl/min produced a degradation of 36%. The average gel-loading rate of 15 μl/min produced a 28% molecular weight degradation through the 50-μm capillary, but only a 12% degradation when loaded in the larger 75-μm capillary. From this data, it appears that the shear degradation experienced during gel-loading is larger in smaller diameter passages.

Table 2.3 summarizes the changes in molecular weight observed for a 3% (w/v) LPA solution loaded into a 50-μm and 75-μm-i.d. capillary. The values of viscosity-averaged molecular weight, M_v, shown in Table 2.3 also illustrate lower levels of polymer degradation in the 75-μm than in the 50-μm-i.d. capillary. During the average 15 μl/min gel-loading,

Table 2.3: Experimental values of the non-Newtonian viscosity, η_0, viscosity averaged molecular weight, M_v, and percent degradation , D_p, for 3% (w/v) LPA solutions (disolved in de-ionized water with original molecular weight of 9 MDa) loaded into 50-μm-i.d. and 75-μm-i.d. capillaries at varying flow rates and $25^0 C$.

Q (μl/min)	η_0^{50} (Pa-s)	M_v^{50} (MDa)	D_p^{50} (%)	η_0^{75} (Pa-s)	M_v^{75} (MDa)	D_p^{75} (%)
1	1370	8.66	1.31	–	–	–
4	882.9	7.54	14.10	1342	8.61	1.94
8	455.3	6.12	30.35	1050	7.97	9.25
15	182.7	4.58	47.81	851.2	7.45	15.09

the 3% polymer solution experienced a 15% molecular weight degradation within the 75-μm capillary, compared to a 48% degradation within the smaller capillary. However, further comparison of the degradation values obtained with the 2% and 3% LPA solutions indicate shear-induced degradation is more sensitive to changes in concentration than to small variations in cross sectional area. Previously, a 2% LPA solution loaded at a rate of 3 μl/min within a 50-μm-i.d. capillary resulted in a 4% degradation. Using a 3% LPA solution, the decrease is a factor of 4 higher at 14%. In fact, when using 3% solutions even the lowest attainable flow rate of 1 μl/min results in a 1% polymer degradation.

Note, as discussed earlier, since percent degradation is obtained from the calibration of viscosity averaged molecular weight, M_v, degradation values do not correlate one to one with changes in polymer length. For example, Table 2.2 illustrates that the average gel-loading rate of 15 μl/min through a 50-μm-i.d. capillary produced a 28% degradation in viscosity-averaged molecular weight. Using Equation 2.13, this means that roughly 25% of the chains were broken in half during this gel-loading. Similarly, the 12% degradation experienced by the gel in the larger capillary indicates that approximately 15% of the chains were broken in half. Looking at Tables 2.2 and 2.3, values of percent degradation for solutions gel-loaded

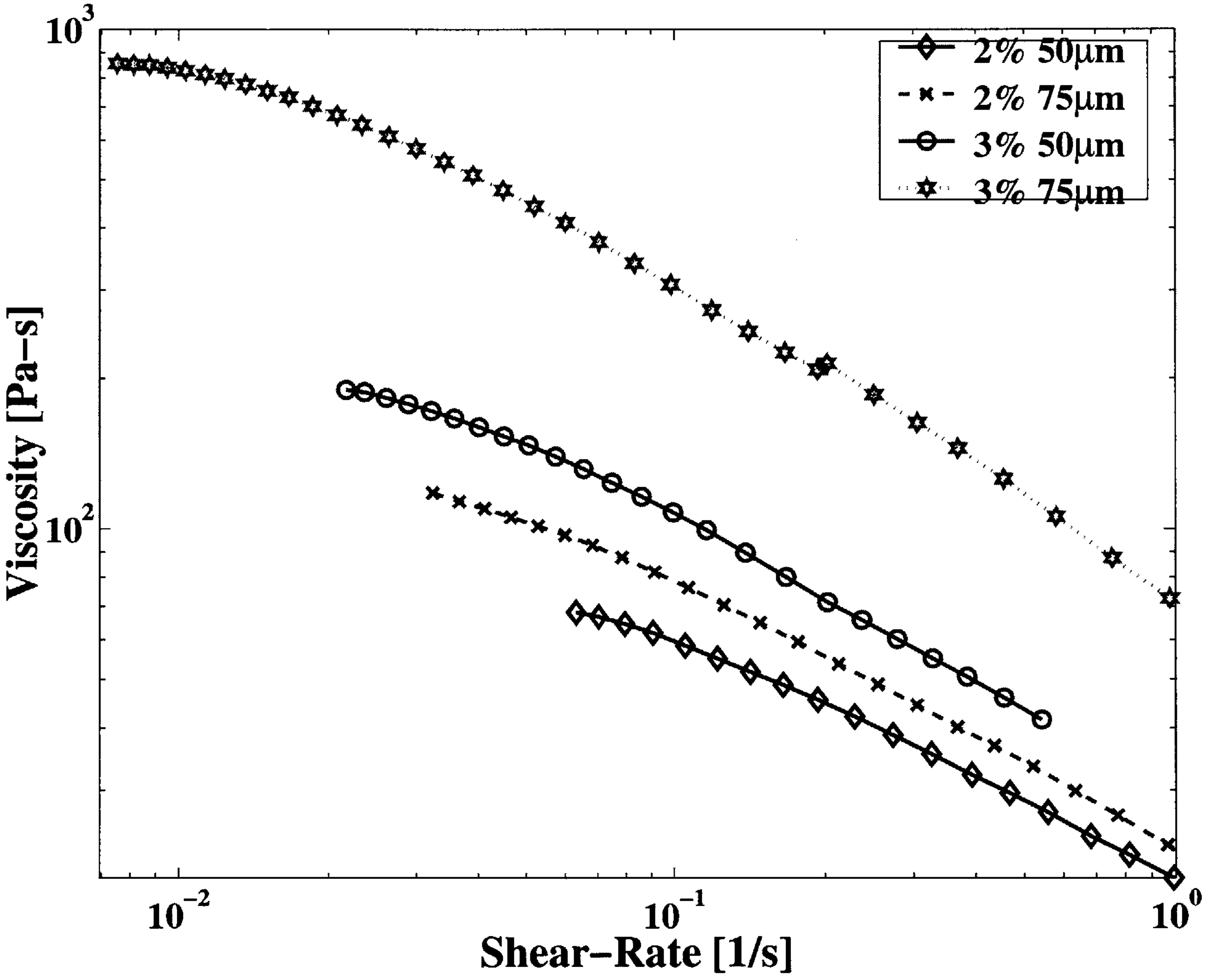

Figure 2-7: Non-Newtonian viscosity profiles of 2% and 3% (w/v) LPA solutions after gel-loading was performed at the average rate of 15 μl/min in a 50-μm and 75-μm-i.d. capillary.

within a 50-μm capillary ranged from 4% - 47%, indicating roughly 3% - 48% of the polymer chains were broken in half. Solutions gel-loaded within the larger capillary experienced 1% - 36% degradation inidcating only 1% - 33% of polymer chains were broken in half.

The effects of chain disentanglement in these experiments can be monitored using viscoelastic stress relaxation measurements. A relaxation time of a polymer is a measure of its 'fading memory' of previous deformations [159]. For an entangled polymer solution, this stress relaxation arises principally by reptation, as the deformed polymer chains slowly diffuse along their confining 'tube' until they regain their isotropic entangled configurations [91]. As mentioned in Section 2.2, the critical shear rate, $\dot{\gamma}_{crit}$, is approximately the inverse of the polymer relaxation time, λ. The viscosity measurements shown here indicate that the relaxation time of the entangled LPA solutions used is on the order of 600-900 seconds. After two relaxation times, any residual memory of previous deformations, imposed during the loading process for example, will have decayed by a factor of e^{-2} and is thereby negligible [159]. During the present experiments, as in practice, it was common to run electrophoretic separations an hour after gel-loading. Given the polymer's short relaxation time, coil disentanglement effects should be secondary when compared to the effects of coil scission.

2.4.2 Viscous Dissipation

Table 2.2, Table 2.3 and Figure 2-3 summarize the observed relationship between the viscosity of the LPA solutions and the volume flow rates at which they were loaded. In Figure 2-7 we compare the viscosity profiles obtained for each polymer sample and capillary at the average gel-loading rate of 15 μl/min. In the figure, higher LPA concentrations coupled with smaller cross sectional areas produce the largest decrease in viscosity and zero shear-rate viscosity η_0. The increased degradation can be attributed to the higher shear rates experienced by the more viscous fluid as it is loaded and displaced into smaller diameter passages. This is an important result for electrophoresis as many of the chemical additives commonly used as the buffered solvent for LPA solutions increase the viscosity of the sieving matrix making the fluid more viscous and prone to degradation. Buffers which incorporate large amounts of urea, for example, generally increase the viscosity of the sieving matrix by 10% per 1M Urea added [127].

As discussed earlier, the viscosity of a solution can be related to its molecular weight by Equation 2.2. Due to the interpenetration of polymer chains in entangled solutions, increasing the polymer concentration will increase the solution viscosity non-linearly [159]. The higher entanglement density of polymer chains present in solutions of increased concentrations implies that the shear-induced degradation of polymeric solutions will increase with increasing viscosity.

It was for this reason that LPA solutions for these experiments were prepared by dissolving LPA powder in DI water: This polymer synthesis produced LPA sieving solutions with the minimum attainable viscosities. The experimental data predicts that the percent degradation, D_p, experienced by LPA solutions of higher viscosities will be much greater. Since LPA solutions must use buffers for DNA electrophoresis, the values of Dp shown here reflect the minimum amount of polymer degradation that can be expected. LPA solutions prepared in buffers which incorporate large amounts of Urea can expect high polymer degradation during gel-loading.

An equation to estimate molecular degradation, D_p, based upon wall shear stresses, τ, and shear rates, $\dot{\gamma}$, imposed during gel-loading would greatly assist in selecting fill rates for any loading protocol. The energy lost by the polymer in the form of chain scission and disentanglement is correlated with the product of the shear stress and shear rate, often called the viscous dissipation, Φ,

$$\Phi = \tau : \dot{\gamma} \tag{2.19}$$

As defined in Equation 2.19, viscous dissipation is a universal parameter that measures the rate of energy dissipation per unit volume in any system. It represents the kinetic energy that is irreversibly converted to thermal energy due to viscous effects in the fluid [125]. In order to discuss viscous dissipation in the context of these experiments, the polymer is modeled as a power-law fluid [159] to obtain a more specific relation for Φ. As both the stresses and shear rates vary nonlinearly in the channel, the local dissipation is integrated radially to obtain the expression below:

$$\Phi = \tau : \dot{\gamma} = m \left[\frac{Q(3 + 1/n)}{\pi R^3} \right]^{n+1} \tag{2.20}$$

where Q represents the volume flow rate during gel-loading in μl/min, m is the consistency index of the polymeric solution with units Pa-s^n, n is the dimensionless power-law shear thinning exponent of the polymer and R is the inner radius of the electrophoretic channel. The units of Φ as defined by Equations 2.19 and 2.20, correspond to energy density per second, or $[\frac{J}{m^3}/s]$. Figure 2-8 displays the experimental data gathered for D_p plotted against the corresponding dissipation values described by Equation 2.20.

The data lies on a power law curve and can be used to estimate the molecular degradation expected for various gel-loading protocols. Using curve fitting, the data in Figure 2-8 can be described by the following equation with less than 8% error:

$$\Phi = (4.89){D_p}^{0.445} \tag{2.21}$$

This equation shows that the percent degradation experienced by the polymer solution during gel-loading scales approximately as the square root of the power dissipated per unit time, or the square root of the viscous dissipation. Using Equation 2.21, one can estimate the shear-induced degradation experienced by the polymeric solutions. For instance, when a 2% LPA solution was gel-loaded within a 75-μm capillary at the average flow rate of 15 μl/min, a 12% decrease in molecular weight was measured experimentally, as shown in Table 2.2. Using the equation in Figure 2-8 to estimate the degradation, one obtains a somewhat lower value of 10%. It should be noted that although viscous dissipation, Φ, is a universal parameter, its correlation with the derived parameter molecular degradation, D_p, is most valid for semi-dilute, entangled solutions of LPA. Additonal experiments utilizing a larger concentration range are needed to quantitate the extent of shear-induced degradation of more concentrated solutions of LPA during gel-loading.

At first glance the estimated average gel-loading rate of 15 μl/min might appear too conservative. However, for a 12-cm-long channel of 4418-μm^2-cross-sectional area (75-μm-i.d. capillary), the volume flow rate reveals that the channel volume is replaced 30 times per minute during this gel-loading. Put into these terms, a 15 μl/min gel-loading is hardly

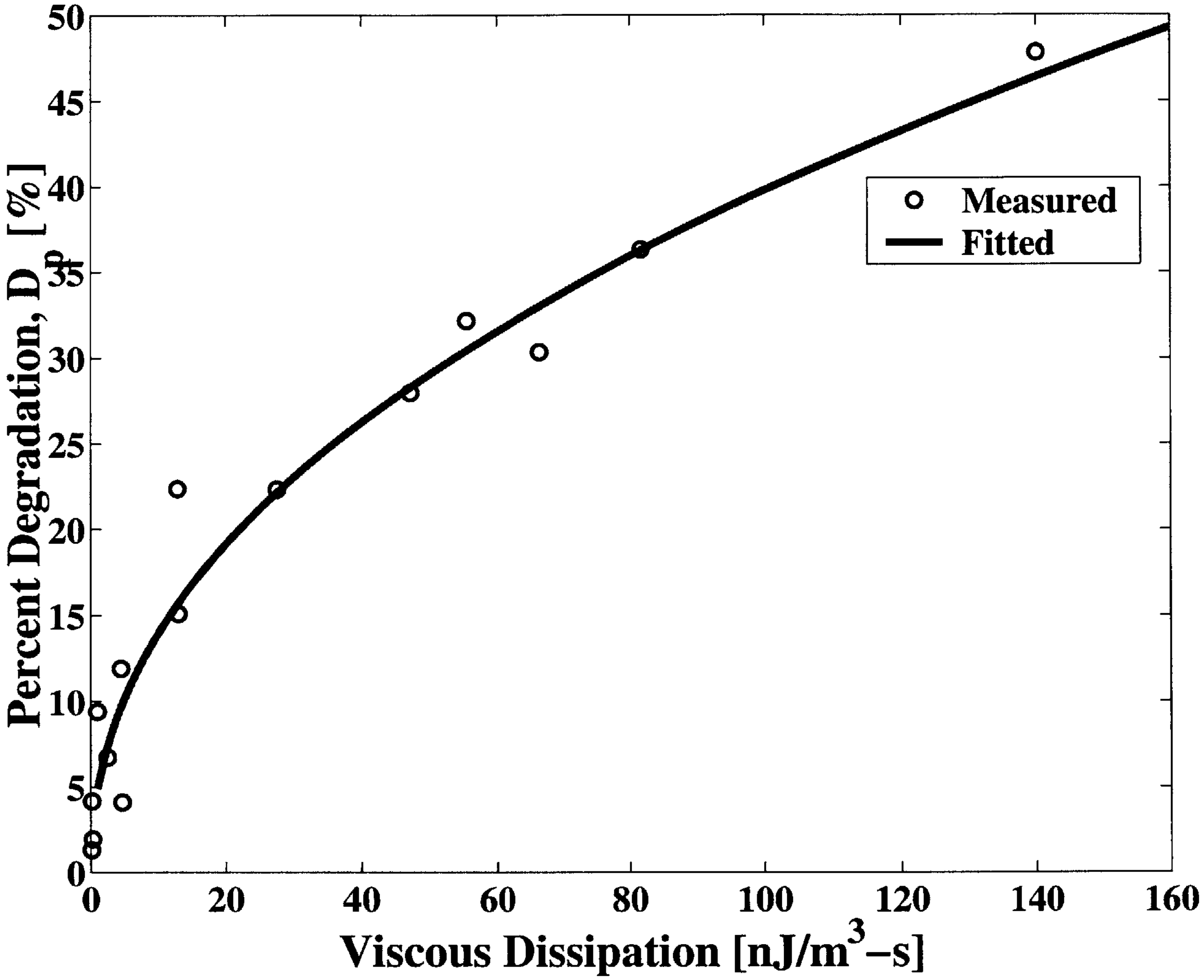

Figure 2-8: Experimental data of percent molecular degradation, D_p, plotted against the energy dissipated during gel-loading, Φ. The polynomial curve which fits the data is described by $D_p = 4.89\Phi^{0.445}$ with less than 8% error.

conservative. By tripling the loading time to 3 minutes, the fill rate is reduced from 15 μl/min to 3 μl/min, and hence, the polymer volume is replaced only 6 times in one minute. Since current experimental data indicates no polymer degradation is evident for such fill rates, the polymer degradation problem seems easily alleviated through implementation of longer gel-loading times.

2.4.3 Electrophoresis Measurements

Shear-induced degradation of LPA solutions during gel-loading has been clearly demonstrated through measurements of their viscometric properties. To observe how imposed shear influences DNA separations, each degraded polymer solution was used as a sieving matrix for DNA sequencing by microdevice electrophoresis. Experiments were reproduced over a 3 day period by 2 separate technicians. Microfabricated channels, 12 cm long and of 3600-μm^2-cross-sectional area, were loaded with 2% LPA solutions at carefully metered flow rates of 3, 15, and 25 μl/min with the same apparatus described earlier. Note, the cross-sectional area of the microchannels was specifically fabricated to enable better comparison of the rheology data gathered in the circular 75-μm-i.d. capillary (4418-μm^2 area) to the electrophoretic results gathered in the rectangular microchannel (3600-μm^2 area).

Figure 2-9 illustrates that there is a pronounced decrease in resolution as the gel-loading rate is increased. The figure also shows a pronounced dip in each resolution curve at base number 201. This compression effect is solely a result of the sample preparation protocol, not gel-loading, and indicates the electrophoretic mobility of base number 201 is identical to that of base number 200. The result is a sharp drop in resolution as bases 200 and 201 can no

Table 2.4: Bases of DNA resolved by electrophoresis of an M13mp18 DNA Cycle Sequencing mixture on a 12-cm-long microfabricated device. Separations were performed at 55^0C using 2% LPA solutions injected into electrophoretic channels at three separate flow rates as shown.

Q (μl/min)	Continuous Sequence with $R_L > 0.5$	Number of Resolved Bases
3	85-465	380
15	92-415	323
25	107-390	283

longer be separated by their mobilities alone. Although sample compression is undesirable in an electrophoretic separation, in this particular instance the evidence of compression in all separations illustrates the consistency of the results.

Data analysis revealed broader peak widths and lower resolution values for faster loading rates. Each shear-degraded sieving matrix produced a resolution curve of the same shape but with decreasing resolution values as gel-loading rates were increased. From these experiments, it is seen that shear-induced degradation of LPA solutions does affect sequencing analysis as documented in Figure 2-9 and Table 2.4. Effects are most notable in the data showing the separation of DNA fragments larger than 300 bases. Further, these results were reproduced in five consecutive electrophoretic trails performed by 2 different technicians.

Electrophoresis performed using the sieving matrix loaded at the lowest flow rate of 3 μl/min produced separations which could resolve 380 base pairs of continuous DNA sequence with resolution values greater than 0.5, as defined by Equation 2.16. Separations performed in the polymer matrix loaded at the average rate of 15 μl/min resulted in a lower read length of 323 bases, whereas the separations corresponding to the accelerated 25 μl/min gel-loading were only able to resolve 283 bases. As seen, increasing the gel-loading rate from the average 15 μl/min to 25 μl/min diminished read lengths by 12%. Conversely, a lower gel-loading

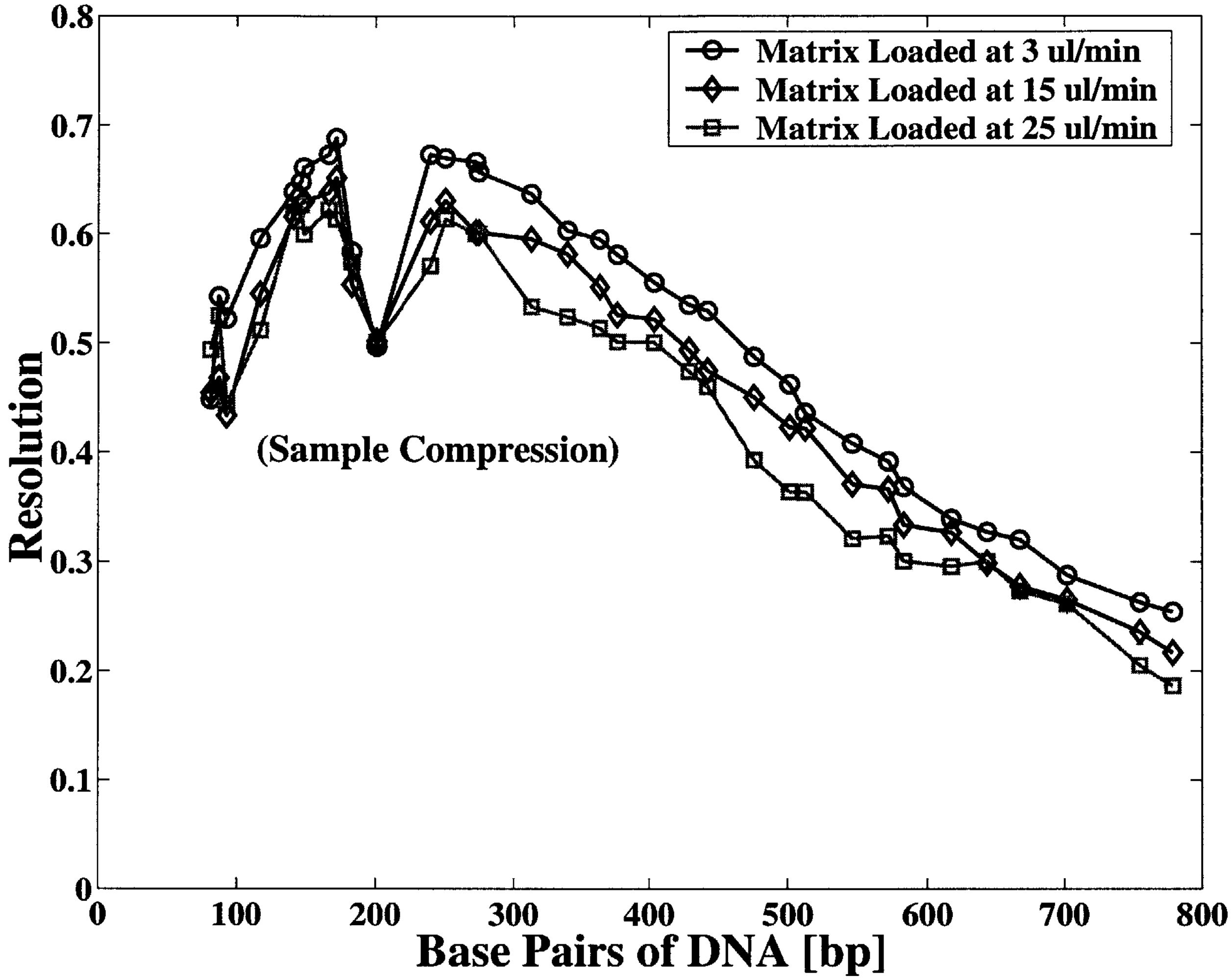

Figure 2-9: Resolution measurements obtained from electrophoregrams of DNA separations. The separations were performed with an LPA gel-loading of 3, 15, and 25 μl/min. Compression due to sample preparation protocol is noted.

rate of 3 μl/min produced a 15% increase in the number of bases resolved over the average 15 μl/min gel-loading and a 25% increase compared to the read lengths obtained using a 25 μl/min gel-loading.

Admittedly, the significance of a 15% increase in the number of bases resolved may vary with the opinion of the researcher. However, the impact of such an improvement strongly depends on the application. For instance, when working with Short Tandem Repeats, STRs, a 15% increase in the number of bases resolved can be the determining factor in DNA forensics [5]. Further, when working with high-throughput screening devices such as those in a genome center, a 15% increase in the number of bases resolved is rather substantial.

2.5 Conclusions

The data presented here illustrate how shear-induced degradation of the sieving matrix can result from improper gel-loading. Further, diminished resolution of subsequent DNA sequencing can be directly linked to this degradation. The experimental data also indicate degradation of the sieving matrix during gel-loading is more affected by the viscosity and concentration of the polymer than it is by the channel cross section. This implies that electrophoretic separations using more entangled solutions of LPA will sustain higher degradation than shown here. For LPA concentrations lower than 3% (w/v), induced degradation can be eliminated if the polymer is loaded at rates below 3 μl/min. Note, in all experiments, the most significant effects were seen in the separation of fragment sizes larger than 300 bases.

As this work has demonstrated, careful scrutiny of conventional loading protocols may lead to significant improvements in DNA separations. While this chapter has fully explored the detriments associated with utilizing conventional gel-loading protocols within microdevices, the next section will examine the effects of adopting typical sample-loading protocols for use within microfabricated devices. This forthcoming study will explore the current methods used to introduce DNA molecules into the microfabricated channel and investigate new protocols to specifically optimize DNA migration into the separation channel.

Chapter 3

Study of Sample Loading Protocols

3.1 Background

As discussed in chapter 1, electrophoretic techniques are widely used for the separation of biological molecules and are becoming increasingly important in the era of protenomic analysis and biotechnology-derived drugs. Although electrophoresis is routinely performed in gels [12] and capillaries [149], electrophoresis performed in microdevices has recently received particular attention because microfabrication [5], [62], [143] enables massively parallel analysis as well as total process integration [143]. However, the potential for such future devices lies in the ability to understand and apply current electrophoretic techniques in these devices. Simultaneously, electrophoresis in microdevices will benefit from the volume of research performed in the development of the sieving matrix [151], [152], preparation of the sample solution [145], [141], and improvement of electrophoretic protocols [144], [148].

One way to deepen our understanding of the electrophoretic process is to carefully examine and question the protocols typically used during DNA separations. This was the goal of the gel-loading study presented in the preceding chapter regarding the effects of the polymeric matrix on DNA separations. The present study now examines the protocols used during sample-loading by utilizing a microscopy-based approach to capture the dynamics of DNA samples at different stages during their separation.

The present study visualizes the motion of fluorescently-tagged DNA samples at the beginning of each separation, during sample loading and electrophoretic injection. This stage of electrophoresis is particularly critical to separations because DNA molecules experience two distinct physical processes during their initial migration towards the anode: stacking [179], [178], [55] and de-stacking [26]. Distinct from the separation process, stacking occurs within milliseconds of sample injection and can be readily monitored within the microdevice using the new microscopy-based approach described here.

DNA separations are performed within microdevices using four different reservoirs (cathode, anode, sample and waste), and three distinct channel sections (separation channel, cross-injector and channel tail) [5] as shown on Figure 3.4.1. DNA molecules are first drawn into the microdevice by a potential gradient that is imposed between the sample and waste reservoirs of the cross-injector. This process is called sample-loading and is used to create a uniformly distributed DNA sample plug within the cross-injector offset. During the next step, called injection, a run voltage is imposed between the cathode and anode of the microdevice in order to initiate DNA migration towards the anode.

During the early stages of injection, there is a rapid re-distribution of DNA molecules which is driven by differences in ionic conductivity [153] between the sample and electrolyte buffer solutions [26], [155], [154]. Typically, the ionic concentration of the electrolyte buffer is much higher than that of the DNA sample solution [141]. When the run voltage is imposed, areas of high conductivity then experience low potential gradients while areas of low conductivity experience high potential gradients [76], [15]. As a result, DNA molecules migrate rapidly within the high fields of the low-conductivity region of the cross-injector, but experience an abrupt drop in velocity upon reaching the lower fields within the high-conductivity electrolyte buffer [156], [157]. The subsequent decrease in velocity creates a thin and focused zone of DNA molecules at the interface between the sample and separation buffer, called the stacked zone [26], or stacked sample [154].

In order to visualize the motion of DNA samples during sample loading and electrophoretic injection, DNA molecules were fluorescently tagged with propidium iodide and observed using an epi-fluorescence microscope. Once the sample was introduced into the microdevice, detailed images of its loading within the cross-injector, and subsequent electrophoretic injection into the separation channel, were captured using a CCD camera. These images demonstrate the complete process of sample loading and stacking, as well as illustrate the effect of many commonly-used protocols.

The study in this present chapter has quantitatively measured the width of the stacked sample plug using the values of intensity recorded for each pixel within the digital images. Experimental data gathered from the images is used to identify specific parameters that define stacking and its level of intensity. Additionally, we have developed a model which represents the sample plug by N Gaussian distributions of DNA molecules that migrate with similar group velocity throughout injection. The transient redistribution of DNA molecules within each Gaussian then describes the formation and propagation of the stacked sample during electrophoretic injection. The results are used in conjunction with an analytical model [26], [67] to build an empirical tool that gauges the level of stacking experienced by DNA molecules under various experimental conditions.

Additionally, results from video microscopy are correlated with electropherograms in order to quantify the benefits of increased stacking to DNA sequencing. A new high voltage injection protocol is shown to dramatically increase the level of stacking exhibited by DNA samples and subsequently increase resolution measurements by 35%. This study performed DNA injections within microdevices imposing run voltages of 85 V/cm - 850 V/cm between the cathode and anode ports of a microfabricated device. Data from 3 different offset lengths of a double-T cross-injector, 10 different applied voltages, and 2 different sample preparation protocols are presented.

3.2 Theory

The stacking process incorporates the simultaneous migration of various DNA molecules under the influence of high potential gradients. Study of such a process is particularly difficult because it incorporates the effects of moving ionic gradients [1], [67], and conformational properties of polyelectrolytes [74]. However, a more fundamental understanding of the stacking process, and electrophoresis in general, can be gathered from review of the basics of polymer physics [89], [68] electrostatics [78], [2], [73] and mechanisms of electrophoretic migration [10], [132], [42]. The basic principles of these areas were highlighted from an engineering standpoint in chapter 1, and now are used in this section to present a simplified, analytical model of the mechanism of stacking.

3.2.1 The Mechanism of Stacking

The phenomenon of stacking within a cross-injector operates on the same principle as stacking in a capillary [61], [156], [155], [154]. When an electric field is applied along a channel, the flux of charged ions within the channel generates a current that is described by its current density, I [76]. This vector points in the direction of current flow and is strongly influenced by the ionic conductivity of the medium.

$$\mathbf{I} = -\kappa \nabla \mathbf{\Phi} \tag{3.1}$$

In the above expression, κ denotes the ionic conductivity of a material, expressed in Siemens per centimeter, S/cm, while $\nabla(\Phi)$ represents the potential gradient, or electric field applied along the material, in units of V/cm. The conductivity of a material reflects its ability to facilitate the transport of ions within it [76],[15]. As seen from Equation 3.1, materials of high conductivity facilitate ion transfer quite easily and, therefore, require low potential gradients to sustain a steady flux of ions within it. Conversely, materials of low conductivity interact with transporting ions and require higher potential gradients to sustain the same steady flux.

Due to the chemical composition required for separations, the ionic conductivity of the buffer electrolyte solution, κ_B, is much higher than that of the DNA solution κ_D. Hence, when the run voltage is applied along the channel, a disproportionate amount of the potential drop is found along the low-conductivity-sample plug [132]. However, as the molecules migrate towards the buffer solution, they exhibit an abrupt drop in velocity upon experiencing the lower potential gradients present within the electrolyte. The sudden decrease in velocity creates a very thin and concentrated zone of DNA molecules at the injector exit via the mechanism called 'stacking' [152], [26], [155], [154].

The Moving Boundary Equation

Stacking can be described analytically using the one-dimensional moving boundary equation first described by Longsworth in the late 1950's [22]. The moving boundary equation is particularly appropriate for the discussion of DNA stacking because it relates the concentrations of ions on either side of a boundary to the distance traveled by the boundary, and the relative mobility of ions on either side of it [76]. Since DNA molecules are constrained within the cross-injector prior to separation, the sample plug has two DNA boundaries, the frontal and terminating boundaries. The frontal boundary is formed between the sample plug and buffer region closest to the anode, while the terminating boundary is formed between the sample plug and buffer closest to the cathode. Molecules on the frontal boundary immediately migrate out of the sample plug and into the buffer electrolyte during injection because of their proximity to the anode [26], [67]. In contrast, molecules on the terminating boundary migrate towards the anode within the sample plug at all times during injection as a consequence of their position within the cross-injector. Using the moving boundary equation, stacking is described utilizing a Lagrangian reference frame that migrates concurrently with the sample's frontal interface. The stacking velocity can be determined from the expression [26], [22]:

$$\frac{\mu C_{D,S}}{\kappa_S} - \frac{\mu C_{D,B}}{\kappa_B} = \frac{V_{ST}(C_{D,S} - C_{D,B})}{I} \tag{3.2}$$

where μ represents the electrophoretic mobility of DNA, $C_{D,S}$ is the concentration of DNA, D, present in the sample plug, S, and $C_{D,B}$ is the concentration of DNA in the electrolyte buffer, B. The ionic conductivity of the sample plug, (S), is denoted by κ_S, while κ_B represents the ionic conductivity of the buffer, (B). The parameter V_{ST} represents the stacking velocity, i.e. the velocity of the terminating boundary with respect to the frontal boundary, and I is the total current density within the channel. From Equation 3.2, the current density is defined by the total flux of ions within the channel. In the general case, flux can be attributed to electromigration, diffusion, and convection.

$$I = -\kappa \nabla \Phi - F \Sigma z_i D_i \nabla (C_i) + F u \Sigma z_i C_i \tag{3.3}$$

Where Φ is the electric potential in volts, F is Faraday's constant of value 9.65×10^4 C/mol, κ is ionic conductivity in S/cm, D is diffusivity measured in cm^2/s, z is the dimensionless valence number of the i'th ion, u is the bulk velocity (which is identically zero for a fixed external matrix), and C is concentration in $1/m^3$. For the general problem, conductivity, κ, can change in time due to redistribution of ions within the channel. Although many of the outstanding variables must first be determined, an expression for the stacking velocity, V_{ST}, can be obtained utilizing Equations 3.2 and 3.3 simultaneously. The main difficulty in this endeavor, however, is finding an expression for the distinct concentrations of interest. For this, conservation of chemical species must be considered.

Conservation of Chemical Species

Identifying a small control volume within the sample zone, conservation of chemical species is applied according to the principles of transport phenomenon [1]. For a given chemical species, i, within the sample zone, the local rate of accumulation within the control volume is balanced by the rate of flux to the volume, f_i.

$$\frac{\partial(n_i)}{\partial t} = -\nabla \cdot f_i \tag{3.4}$$

Where n is the concentration of species i, and f_i is the rate of flux as described by Equation 3.3. Equation 3.4 can be solved for a concentration profile of DNA, n, as a function of position within the stacked sample plug. A single equation to describe the concentration profile of DNA within the sample plug during stacking has been derived by Russell et. al. [67].

$$C(x) = \frac{(2-\gamma)}{2(1-\gamma)} \frac{\xi^{(1+\nu)}}{\sqrt{(1+\xi)}} \left[\int \frac{\omega^{(-2-\nu)}}{\sqrt{(1+\omega)}} d\omega \right] \tag{3.5}$$

where C denotes the spatial variation in the concentration of DNA molecules, ω is a variable of integration, and the dependent variables, ξ, γ, and ν are defined as per Saville et al. [67], [67] as:

$$\xi = \exp \frac{-x(-\mu_1 - \mu_2)}{(\mu_1 \mu_2)} \tag{3.6}$$

$$\gamma = \frac{(1+\mu_1)\mu_2}{(1+\mu_5)\mu_3} \tag{3.7}$$

$$\nu = \frac{\gamma}{2(1-\gamma)} \tag{3.8}$$

Where μ denotes electrophoretic mobility, and x represents position in the sample zone, measured positively from the interface of the sample and buffer zones towards the cathode.

Equations 3.5 - 3.7 represent an equation that describes the concentration profile of DNA within the sample plug as a function of position, x. This expression is integrated along the channel length in order to obtain numerical estimates for $C_{D,S}$ and $C_{D,B}$, the final concentration of DNA molecules that migrate within the sample zone during stacking, and the final concentration of DNA that migrate within the electrolyte buffer, respectively. When the integration is completed, all of the parameters in Equation 3.2 are identified, and a numerical value for the stack velocity, V_{ST}, can be assessed via substitution of appropriate values.

Potential Gradients

Stacking has been predominantly studied assuming the potential gradients within the sample plug remain constant throughout the process [10], [67]. One of the more complete stacking models proposed by Gebauer et. al. [26] defined two types of stacking termed frontal- or terminator-type stacking. DNA exhibit frontal-type stacking when molecules accumulate near the frontal boundary of the sample zone, nearest the anode. Conversely, DNA exhibit terminator-style stacking when molecules accumulate near the terminating boundary of the sample zone, nearest the cathode.

In the first type of stacking, molecules are concentrated on the frontal boundary. To first order, with constant potential gradients within the sample plug, DNA molecules experience an abrupt decrease in velocity only when they reach the frontal boundary, and are influenced by the lower potential gradients of the electrolyte buffer almost immediately. In a more complex model, potential gradients within the sample are modeled as time dependent and gradients change accordingly with the width of the sample plug during stacking. Here, potential gradients change within the stacked sample because the conductivity of the sample plug is proportional to its width and void fraction of molecules [15], [76].

In terminator-type stacking, the potential within the sample plug is continuously modified as the sample width diminishes, imposing the largest gradients near the terminating boundary [26] and the smallest potential gradients towards the frontal boundary. Accordingly, molecules accelerate during electrophoretic injection when the stacked sample reaches their position, developing a concentrated, stacked plug of DNA molecules on the sample's terminating boundary as a larger number of molecules are accelerated by the high potential gradient associated with this interface. Note that although molecules also decelerate at the frontal boundary as they experience the lower potential gradients of the electrolyte buffer, the stacked sample is developed on the terminating boundary of the sample plug.

Regardless of the specific type of stacking exhibited by a system, the principal driving forces and experimental parameters that determine the level of stacking are incorporated in the analysis of the stack velocity, V_{ST}, described Equation 3.2. What is lacking, however, is a model to describe the transient formation of the stacked sample under different experimental conditions. The present work, therefore, proposes a simplified model of stacking based upon direct observation of the stacking process via microscopy. Here, an N-Gaussian model is used to describe the effects of DNA velocity, ionic conductivity, concentration and potential gradients on sample loading and electrophoretic injection.

3.3 Experiments

Sample loading and electrophoretic injections of DNA solutions were observed within the cross-injector portion of microdevices using an inverted, epi-fluorescence microscope. Microfabricated devices used in this study utilized a double-T cross-injector configuration, identical cross-sectional areas, and equal separation lengths. The inner walls of the microfabricated channels were coated using a Hjerten procedure [54] while a polymeric sieving solution was gel-loaded into the channel center at rates that insured minimum degradation [113]. Channels were re-loaded with a new volume of sieving solution prior to, and in between, successive sample-loadings and injections. Additionally, pre-electrophoresis was performed at 300 V/cm for 3 minutes, before each sample-loading.

Both monodisperse and polydisperse solutions of DNA were utilized for the study of sample-loading and electrophoretic injection. Monodisperse samples consisting of 500-base-long DNA fragments were obtained from PCR amplification, while polydisperse samples were generated using DNA sequencing reactions from the same template vector (M13mp18). All of the molecules in each sample solution were fluorescently labeled with propidium iodide so that their fluorescent signal emitted under illumination could be recorded by a CCD camera. The camera provides a digital image of the recorded signal by assigning an intensity value to each pixel within the field of view of the microscope. Digital images were stored in 8-bit format utilizing an intensity measurement from 1 to 256 on a gray scale. Images are used to qualitatively compare the different behavior of DNA molecules observed under various experimental conditions. Quantitative analysis of these images enables a more thorough description of the stacking process.

3.3.1 Micromachining

Electrophoretic microdevices were made from 150-mm-diameter glass wafers (Corning, NY) using techniques described in the literature [5]. The devices each utilize a double-T cross-injector geometry for sample-loading which consists of a sample, offset, and waste channel. The separation channel is hemispherical in cross-section, approximately 40 μm deep and 90 μm wide, and has an effective length of 11.5 cm. The sample and waste channels of each cross-injector are $\sim$ 5.0 mm in length, and horizontally offset by a distance of 150μm, 250 μm, or 500μm. Glass reservoirs (Ace Glass, Vineland, NJ) of 50 μl volume are affixed around the laser-drilled holes accessing the electrophoretic channel in order to contain the appropriate sample and buffer solutions.

3.3.2 Preparation of Polymeric Solutions

The inner surfaces of the microfabricated channels were coated using a commercially available (PolySciences), low molecular weight Linear Polyacrylamide (LPA) solution of $\sim 3 \times 10^9$ g/mol or Daltons, Da. The sieving matrix loaded into the channel center is a different LPA solution of $\sim 9 \times 10^9$ Da [113] synthesized in-house according to the procedure described by Goetzinger et. al. [141]. Solutions of 2% (w/w) LPA were prepared using 1 x TTE (50 mM Tris/50.0 TAPS/2.0 mM EDTA) with 9.0 M urea. The solutions were ready for pre-electrophoretic gel-loading after 3 days of slow stirring.

3.3.3 Electrophoresis

DNA sequencing reactions were loaded into the cross-injector by applying a negative potential of 2300 V (corresponding to 300 V/cm) to the sample reservoir and keeping the waste reservoir at ground. During sample-loading, the buffers in both the anode and cathode reservoirs were left floating. Leakage of excess sample from the cross-injector into the separation channel was prevented with a small electric pull back voltage ($\sim$ 40 V/cm) applied to both halves of the loading channel 10 seconds after injection. In all experiments, a run voltage between 85 V/cm and 850 V/cm was applied for 5 seconds during electrophoretic injection and then reduced to the standard 150 V/cm for full separation using a voltage relay switch.

In order to obtain resolution data from electropherogram analysis, the G-traces of BigDye-Terminator labeled DNA sequencing reactions were used [5]. The G-traces were selected due to minimal cross-talk and ease of tracking isolated peaks over the entire range of fragment sizes. From the resulting electropherograms, the migration time of the sequencing fragments were plotted against their base number and fitted with a Gaussian distribution using Microcal Origin 6.0 software (Microcal Software Inc., Northampton, MA).

3.3.4 DNA Samples and Purification Methods

The dynamics of DNA molecules during sample-loading and electrophoretic injection were studied using both monodisperse and polydisperse samples. Monodisperse solutions were prepared using 10^{-10} M concentrations of single stranded, 500-base-long molecules obtained through PCR amplification of the M13mp18 vector (New England Biolabs, Beverly, MA). Polydisperse reactions were prepared using 10^{-10} M concentrations of DNA sequencing reactions obtained from the M13mp18 vector. Sequencing reactions were comprised of single-stranded DNA molecules ranging from 1 to 7300 bases in length, including the template molecule. Polydisperse samples were synthesized via standard cycle sequencing chemistry with AmpliTaq-FS, Big-Dye-Terminator-labeling (Applied Bio-systems/Perkin Elmer Corp., Foster City, CA). A total of 200 μg of template DNA was used per 96 sample preparation. Cycle sequencing was performed on a Genius thermo-cycler (Techne, Duxford, Cambridge, UK) consisting of 15 cycles of 10 seconds at 95^0C, 5 seconds at 50^0C and 1 minute at 70^0C, followed by 15 cycles of 10 seconds at 95^0C and 1 minute at 70^0C. Note that samples used for the microscopy portion of the experiments were additionally labeled with 10^{-10} M propidium iodide to intensify fluorescence for the CCD camera.

All of the monodisperse samples and half of the DNA sequencing samples were desalted using Centri-Sep spin columns (Princeton Separations, Adelphia, NJ). The remaining sequencing reactions were purified using ethanol precipitation. The spin columns were hydrated for at least 30 minutes by adding 800 μL of de-ionized water. The interstitial volume was excluded by spinning the columns for 3 minutes at 3000 RPM. The sequencing sample was diluted in 40 μL of de-ionized water and then placed in the column and spun for 3 minutes at 3000 RPM. The resulting sample volume was diluted to 50 μL with de ionized water, and a 10-μL aliquot was then pipetted onto the electrophoretic device during experiments.

The samples obtained via ethanol precipitation followed the protocols given in the ABI Prism Big-Dye-Terminator handbook [57]. Sequencing reactions were combined with 95% ethanol and de-ionized water before placed in a centrifuge for a 20-minute-spin cycle at the maximum speed of 3600 rpm. Samples were then aspirated and combined with 70% ethanol for a 10-minute-spin cycle. A final aspiration was performed, and the samples were left to dry for 10 minutes in a vacuum centrifuge. The resulting sample volume was diluted to 50 μL with de-ionized water, and a 10-μL aliquot was then pipetted onto the electrophoretic device during experiments.

3.3.5 Microscopy and Digital Imaging

Electrophoretic injections were observed using the 10X objective of an inverted, epi-fluorescence microscope [Nikkon TE 3000]. The microscope is equipped with filter cubes [Nikkon 34-TA47], CCD camera [Orca-Hamamatsu 54327] and a mercury lamp for the illumination of samples. The CCD camera collected the intensity of the fluorescent signals emitted by the labeled molecules at a rate of 8 frames per second using a simple time lapse protocol [Openlab software]. This data was then converted into 8-bit digital images utilizing a 256 gray scale. Using this scale, an intensity value of 1 is recorded when the camera detects a very low amount of fluorescence emitted by the labeled molecules. Since the molecules are uniformly tagged with propidium iodide, an intensity value of 1 also corresponds to a low number of molecules in the pixel of interest. On the other extreme, an intensity reading of 256 indicates the camera is near its saturation limit, meaning the strength of the fluorescent signal emitted by the molecules is approaching the camera's recordable limit. In order to utilize the full dynamic range of the camera, low concentrations of propidium iodide were used to ensure intensity values were maintained between 30 and 200 on the gray scale at all times.

The microscopy images shown are all two-dimensional projections of a three-dimensional channel. Note that although the depth of the channel is not visible in the images, this third dimension influences the intensity of the fluorescent signal recorded by the CCD for each pixel. That is, a labeled molecule positioned farther away from the microscope objective may exhibit a lower fluorescent intensity than if it were located at a closer distance. This is a particular problem when measuring the intensity of pixels within a channel fabricated with uneven depth. Since the channels used for this research were hemispherical, not rectangular, pixels closer to the channel walls have different depths than those located in the center. Hence, in order to eliminate any three-dimensional effects in the digital image, no matter how slight, only pixels in the centerline of the channel were used to describe the shape of the sample plug during stacking. The intensity of each pixel is plotted against its position within the cross-injector in order to build a mathematical profile of the shape of the DNA sample plug. This method is applied to the images gathered from the electrophoretic injections of both monodisperse and polydisperse samples.

OpenLab software [Improvision, Lexington, MA] was used for all data collection through the CCD camera. However, all subsequent numerical manipulations of the intensity values recorded by the CCD camera were performed using NIH Image 3.1 [NIH shareware] and Matlab 5.3 [The MathWorks Inc., Natick, MA.].

3.4 Results

In this section, the qualitative observations and quantitative conclusions derived from the video microscopy of sample-loading and electrophoretic injection are discussed. From data gathered via digital imaging, the stacking behavior of polydisperse reactions appears significantly more complex than expected. The investigation indicates DNA molecules migrate within independent concentrated regions of the sample plug and a new N-Gaussian Model is proposed to empirically describe these observed dynamics. Lastly, the practical benefits of increased levels of stacking are demonstrated via electropherograms and resolution measurements gathered utilizing high voltage injection protocols.

3.4.1 Sample Loading

Figure 3.4.1 illustrates the sample-loading of both monodisperse and polydisperse DNA solutions within the 250-μm-long offset of a cross-injector. In both cases, DNA molecules are initially loaded into the microdevice by a potential gradient imposed between the sample and waste reservoirs of the cross-injector. The sample-loading displayed on the left-hand-side of Figure 3.4.1 was performed for 3 minutes using a 300 V/cm load voltage. The sample shown is a monodisperse sample comprised of DNA molecules obtained through PCR amplification, each 500 bases in length. The solution was purified using spin columns and its concentration was kept near 10^{-10}M, consistent with DNA sequencing protocols. The loading process is represented by 6 images localized within the cross-injector of the micro-device. Images are displayed from top to bottom, depicting the sample arm on the upper right-hand-side and the waste arm on the lower left. The cathode and anode are located at the far right and left, respectively, of the main separation channel oriented horizontally in each image. Using a time-lapse protocol, images were collected every eighth of a second and the representative snapshots used in Figure 3.4.1 are identified by their time indices in the upper-left-hand corner. The variety of colors displayed in each of the images corresponds to the intensity values recorded by the CCD camera as described in the experimental section.

The image at time t = 75 s displays the initial migration of DNA molecules into the injector offset while the next image illustrates the migration of an increased number of DNA molecules within the offset. At time t = 110 s, DNA molecules are seen entering the waste arm of the cross-injector, and by the end of the sample-loading, the injector offset is filled with a uniform distribution of molecules at time t = 180 s.

For comparison, the right-hand-side of Figure 3.4.1 illustrates the sample-loading of a polydisperse sequencing reaction under identical conditions. The sample is prepared from 10^{-10} M sequencing reactions and is also purified using spin columns. During this loading, smaller molecules with the quickest velocity migrate into the cross-injector first, followed by molecules of increasing molecular length. This pattern is clearly demonstrated by the early presence of DNA molecules within the cross-injector offset as seen at time t = 60 s. Molecules from the polydisperse sample have migrated well within the injector offset at this time in contrast to the monodisperse sample whose molecules have only just begun to enter the offset at t = 75 s.

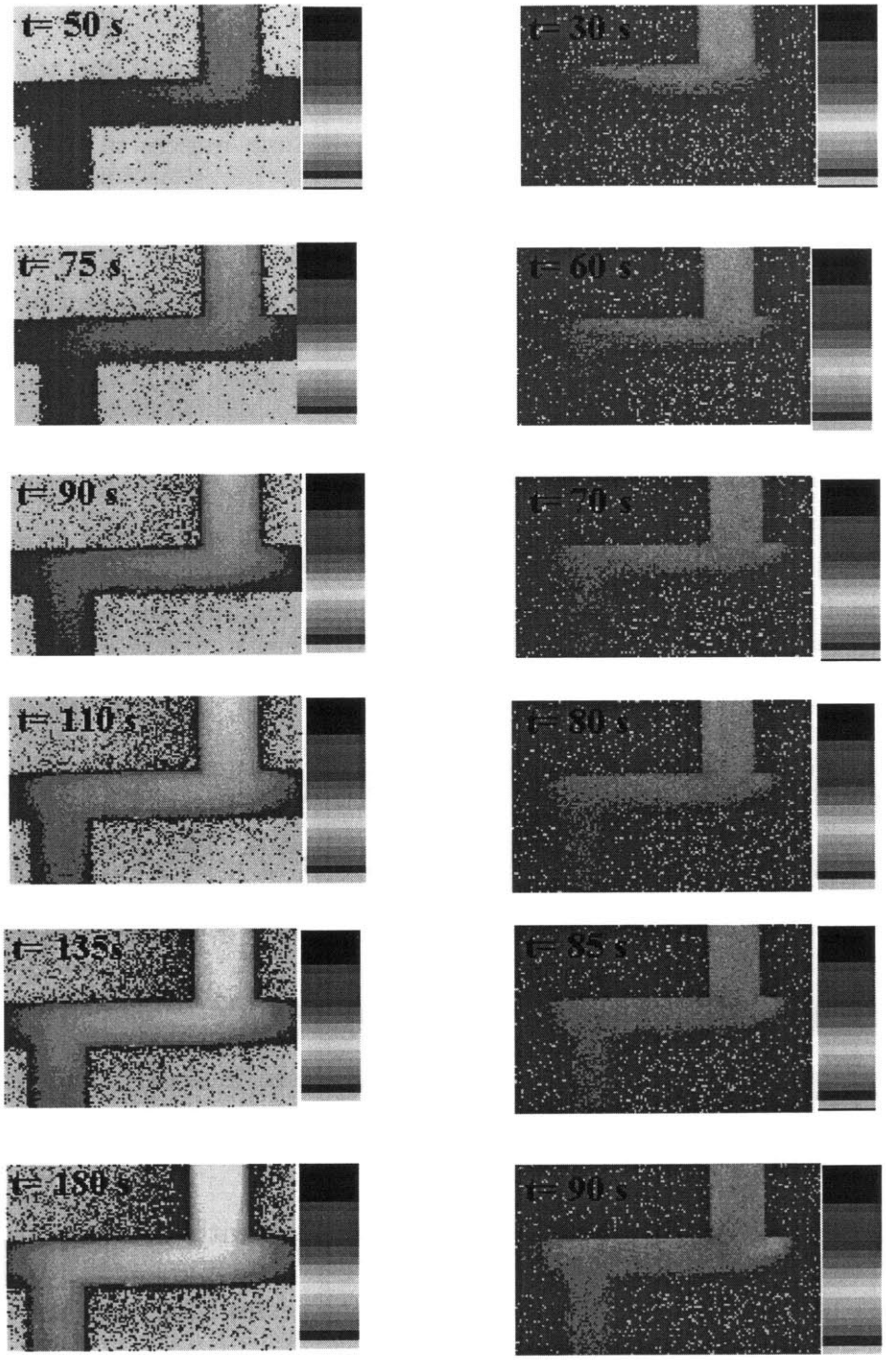

Figure 3-1: The set of 6 digital images on the left-hand-side of the figure illustrate the observed sample-loading of a 10^{-10} M monodisperse solution of DNA. Molecules were each 500-bases in length as determined by PCR amplification and spin column purification. The sample channel is depicted on the upper right while the waste channel is shown on the lower left-hand-side of each image. The complimenting set of 6 images on the right-hand-side of the figure display the observed sample-loading of a 10^{-10} M DNA sequencing reaction purified using spin columns. Length of DNA molecules vary between 1 base and 7300 bases and include template molecules(m13mP18). Both sample loadings were performed for 3 minutes under an applied load voltage of 300 V/cm.

Dynamics of Loading

In general, the overall loading of both samples is similar. The most significant observation gathered from Figure 3.4.1 is the distribution of DNA molecules within the cross-injector. Since the injector offset is formed by sharp, right angles, the equipotential lines around these corners results in regions of large local curvature and, hence, regions of large potential gradient. These nonuniform regions modify the equipotentials and form the curved interfaces seen on both sides of the sample plug.

Diffusive migration of DNA molecules additionally extends the width of the sample near its interfaces with the buffer. Comparing the width of the sample plug throughout sample-loading, these interfaces increase the initial width of the sample by ~ 30 μm, or 15%. Additional experiments performed using injectors of 150-μm and 500-μm-offset-lengths indicate the overall sample width is extended by a similar amount regardless of the injector used. However, sample-loadings performed for up to 10 minutes indicate that while the width of the sample plug remains largely unchanged, its concentration and distribution of DNA molecules change significantly. As seen in Figure 3.4.1, when sample-loading is performed at the typical 300 V/cm load voltage for durations that exceed ~ 5 minutes, the center of the sample plug becomes depleted of molecules while its ends become highly concentrated with, presumably, smaller molecules. Such a non-uniform distribution is later shown to result in poor separations with low resolution.

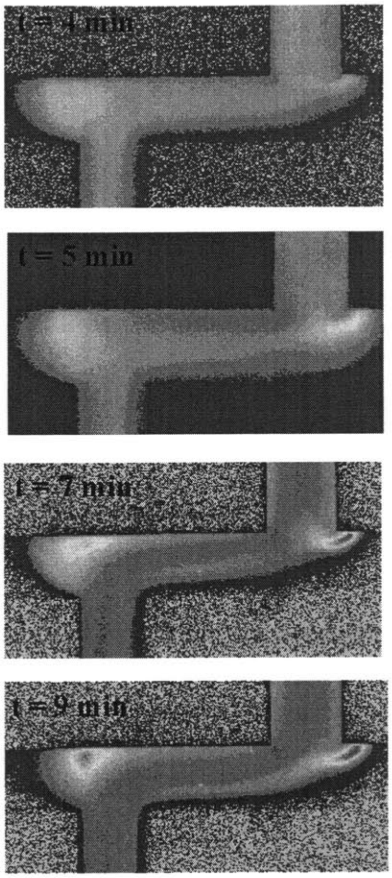

Figure 3-2: Images of the DNA sample plug after samples are loaded into a 250μm-long-cross-injector at 300 V/cm for durations that exceed 5 minutes.

Effects of Protocols

Recent investigations of sample-loading [145] protocols have questioned the benefit of particular sample preparation methods used to remove unincorporated nucleotides and primers from sequencing reactions. As part of the present work, differences in the sample-loading of sequencing reactions purified via spin columns and ethanol precipitation are observed through video microscopy. Both samples were loaded into electrophoretic channels using identical protocols described in the materials and methods section. The concentration of both samples were kept near 10^{-10} M and template molecules were not removed from either sample.

Images of sample loading obtained from both polydisperse samples were virtually identical. The major difference between the two was the time required for loading. DNA molecules of the spin-column-purified reactions were not visible within the offset of the cross-injector until $\sim$ 60 seconds after a load voltage of 300 V/cm was applied. In contrast, DNA sequencing reactions purified using ethanol precipitation were quickly detected within the cross-injector offset $\sim$ 30 seconds after the load voltage was applied. This can be attributed to the larger number of primer molecules and unincorporated nucleotides that remain in the sample as a consequence of ethanol precipitation.

During the 3-minute sample-loading of an ethanol precipitated sample, the width of the sample plug increased by $\sim$ 45 μm instead of the 30 μm seen visually in the loading of the sample purified by spin columns. Further, the migration of these smaller molecules draws excess current from the electrophoretic device without facilitating their separation. Readings gathered during sample-loading indicate reactions purified by ethanol precipitation require an additional 20% of current on average from the system than samples purified using spin columns.

However, the most significant difference between the sample-loading of reactions purified by both methods was evidence of DNA aggregation near the sample reservoir. This behavior often made it impossible for efficient sample-loading, as only a biased population of DNA could migrate past the aggregated molecules within the pre-specified loading time. From the experiments, DNA samples purified with spin columns seemed most susceptible to aggregation after 5 minutes of sample-loading at 300 V/cm. As seen in Table 3.1, aggregations of

Table 3.1: Number of minutes before aggregation of DNA molecules was visible within the cross-injector of a microfabricated device.

V/cm	Ethanol Precip	Spin Column
350	10	4
300	10	5
200	10	5
150	10	6

molecules within the ethanol-precipitated samples were not observed for up to 10 minutes of sample-loading at 300 V/cm. Additionally, representative images of DNA aggregation during sample-loading are shown in Figure 3.4.1.

3.4.2 Electrophoretic Injection

Although DNA molecules are introduced into microdevices via sample-loading, molecules do not migrate towards the separation channel until after electrophoretic injection is initiated. Thus, after the 3-minute sample-loading, the load voltage along the cross-injector was turned off, and a run voltage was applied between the cathode and anode. The subsequent electrophoretic injection of both mono- and polydisperse samples are shown in Figure 3-4. The injection of the monodisperse sample is represented by 6 digital images shown on the left-hand-side of the figure. The injection was initiated by a run voltage of 150 V/cm and utilized a small pull back voltage of 40 V/cm imposed along the cross-injector. The sample injection began when the run voltage was applied at time $t = 0$ s, and ended when the sample plug exited the cross-injector at $t = 3$ s.

At time $t = 0$ s, DNA molecules are uniformly distributed within the offset of the cross-injector, as a consequence of sample-loading. As the electrophoretic injection is initiated,

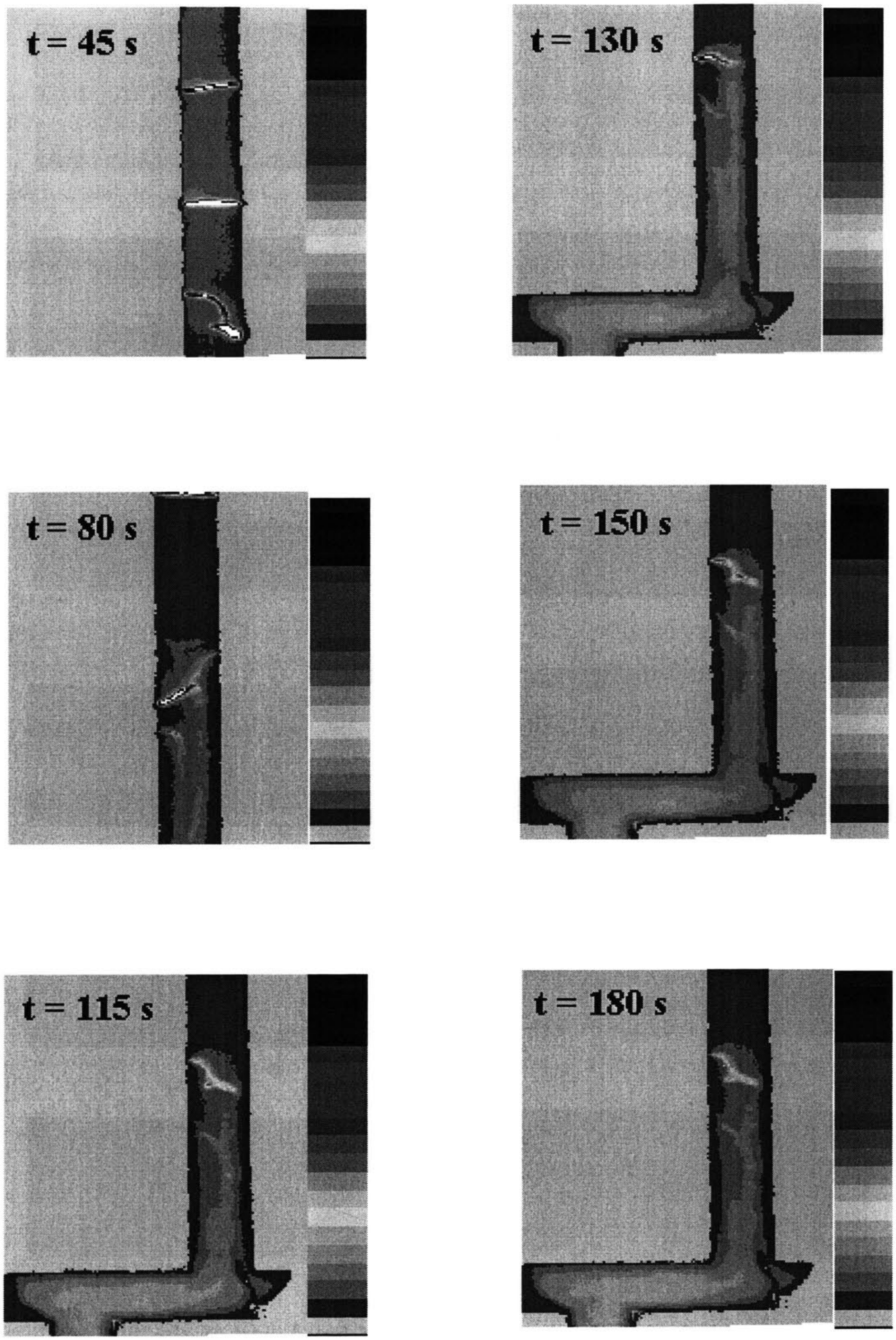

Figure 3-3: Images of DNA aggregation within the channel when polydisperse samples purified via spin columns are loaded into the cross-injector.

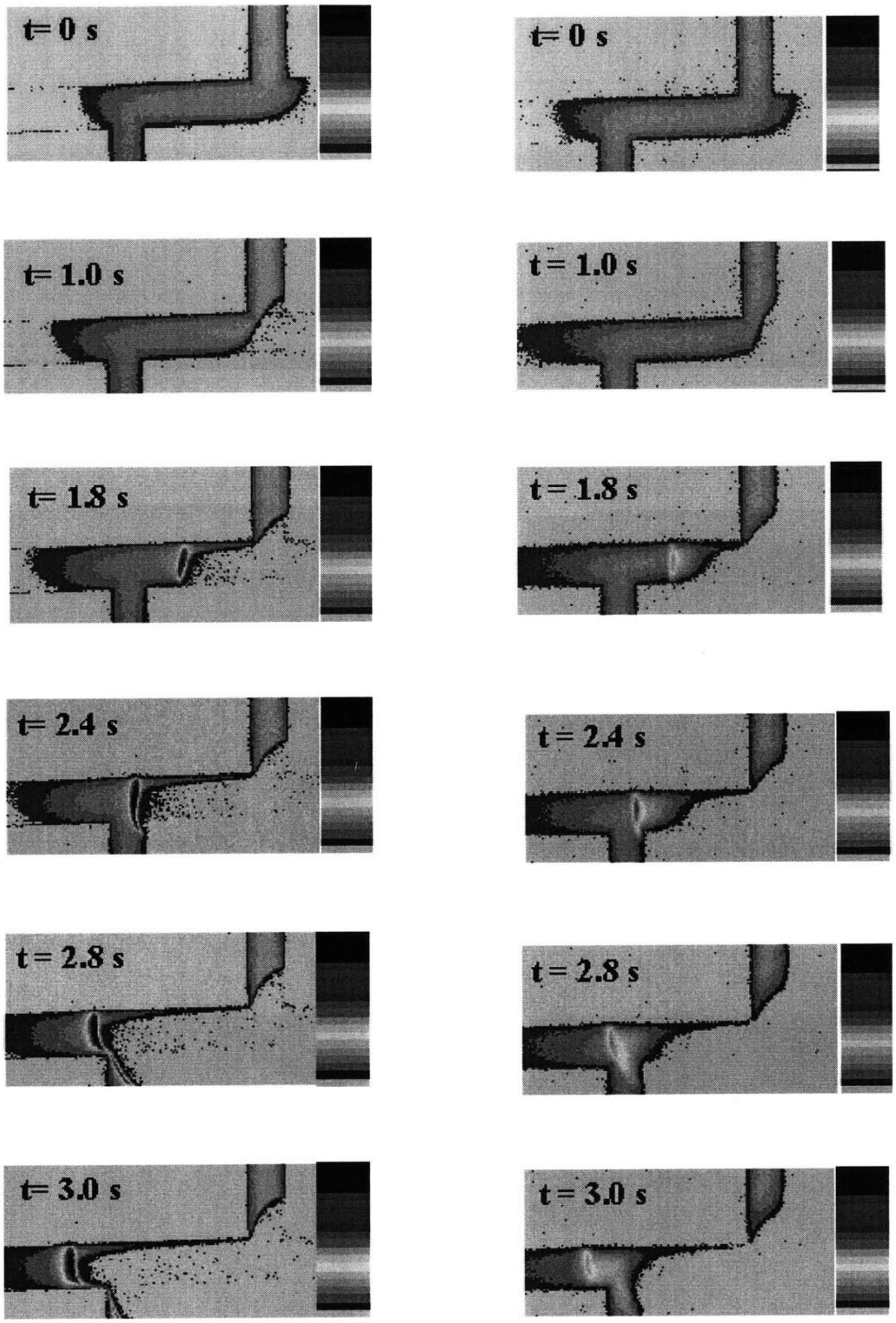

Figure 3-4: The set of 6 digital images on the left-hand-side of the figure illustrate the observed electrophoretic injection of the 10^{-10} M monodisperse DNA solution. The opposite set of images on the right-hand-side of the figure display the electrophoretic injection of the 10^{-10} M DNA sequencing reaction purified using spin columns. Injections were initiated by a 200 V/cm run voltage following a 3-minute sample-loading at 300 V/cm. Time $t = 0$ s, corresponds to when the run voltage was first applied.

the width of the sample plug is visibly diminished as molecules migrate towards the anode. During this migration, the sample's terminating boundary becomes increasingly bright, as first seen at $t = 1.8$ s, indicating the formation of an increasingly concentrated zone of DNA molecules. The high color density seen near the sample rear qualitatively illustrates the development of the stacked sample and its progression towards the separation channel. At time $t = 3.0$ s, the re-distribution of DNA molecules is complete, as the sample plug is reduced to a very concentrated stack near the exit of the cross-injector.

In contrast, the electrophoretic injection of the polydisperse sample under identical conditions is shown on the right-hand-side of Figure 3-4. The sample contains 10^{-10} M DNA sequencing reactions, purified via spin columns as discussed in the materials and methods section. At $t = 0$ s, the polydisperse solution is also uniformly distributed within the injector offset as a consequence of sample-loading. However, as molecules migrate towards the anode, the formation of the stacked sample at the rear of the plug is rather distinct. Whereas molecules of the monodisperse sample formed a tightly concentrated stacked sample at the terminating boundary of the plug, the stacked sample developed by the polydisperse molecules is nonuniform and positioned towards the center of the sample plug. As seen at time $t = 2.4$ s, while molecules from the monodisperse sample exhibit a sharp terminating boundary, the terminating boundary of the polydisperse sample plug remains diffuse during injection. Further, molecules of the polydisperse sample develop a fully stacked sample plug more slowly than do the molecules of the monodisperse sample, as evidenced by their respective stack locations at time $t = 3.0$ s.

Additionally, the electrophoretic injection of the polydisperse sample purified via spin columns is compared to the injection of a polydisperse sample purified via ethanol precipitation in Figure 3-5. The DNA sample on the right-hand-side contains 10^{-10} M DNA sequencing reactions, purified via ethanol precipitation protocols as discussed in the materials and methods section, 3.3. As seen, the injections are very similar and differ primarily in the widths of the sample plug at different times. The sample purified via ethanol precipitation exhibits a much wider sample plug at all stages of injection, but particularly at the injector exit.

The digital images in Figure 3-4 and Figure 3-5 illustrate stacking behavior that is largely consistent with the analytical description of stacking discussed in section 2.4. As stipulated by the moving boundary equation, the sample plug displays both a frontal and terminating boundary, each with a different velocity. Additionally, the formation of a stacked sample is identified from concentration gradients within the sample as predicted by conservation of chemical species. Further, Figure 3-4 illustrates terminator-type stacking during both injections as the stacked sample is initiated on the terminating boundary of each sample plug. As discussed in section 2.4, the stacked sample develops on the terminating boundary of the sample plug due to the changing potential gradients within the sample. The largest gradients are located near the terminating boundary and accelerate molecules ahead of it to develop a stacked sample at the rear of the sample plug. Note, had this system exhibited frontal-type stacking, a concentrated DNA stack would have been formed on the sample's frontal boundary and the images of Figure 3-4 would have illustrated brighter regions near the frontal boundary.

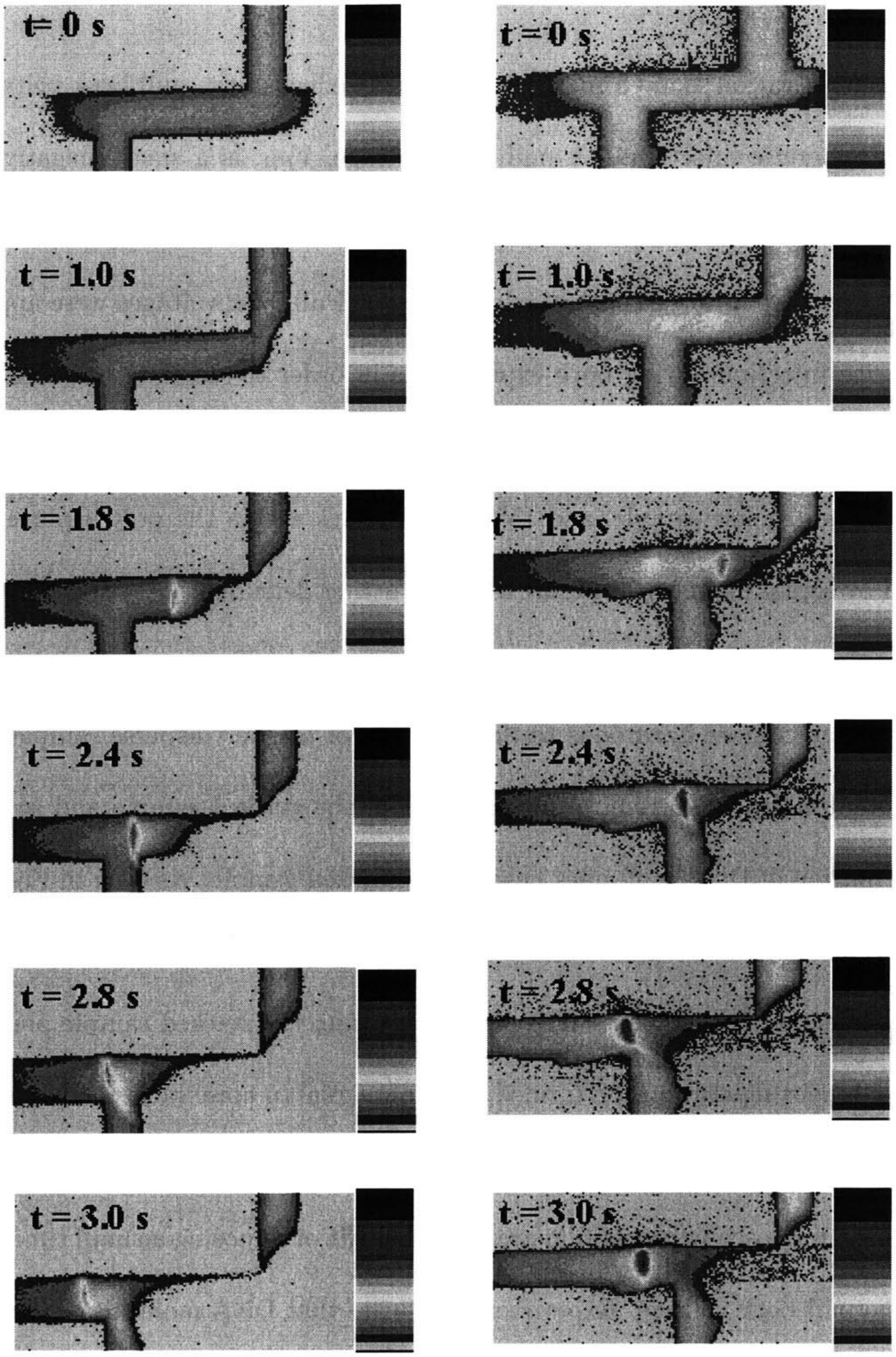

Figure 3-5: The set of 6 digital images on the left-hand-side of the figure illustrate the observed electrophoretic injection of a DNA sequencing reaction purified using spin columns. The set of images on the opposite side of the figure display the electrophoretic injection of the 10^{-10} M DNA sequencing reaction purified via ethanol precipitation. Injections were initiated by a 200 V/cm run voltage following a 3-minute sample-loading at 300 V/cm. Time $t = 0$ s, corresponds to when the run voltage was first applied.

Effects of Protocols

One obvious observation made from Figure 3-4 is the effect of the pull back voltage on both of the electrophoretic injections. A pull back voltage, V_{PB}, is a small, negative potential gradient applied between the sample and waste reservoirs of the cross-injector in order to prevent DNA leakage into the separation channel [5]. Pull back voltages were applied simultaneously with injection during both experiments in order to simulate the commonly used protocol. As seen, the applied pull back voltage extracted roughly 10% of DNA molecules within the monodisperse sample, and 15% of molecules within the polydisperse sample, as determined by signal intensity in Figure 3-4. As further detriment, V_{PB} specifically removes DNA molecules from the stacked sample as illustrated by the image at $t = 2.4$ s. The pull back voltage is more hazardous to the injection of the polydisperse sample because its imposed potential gradients remove molecules from the stacked sample and severely affect the re-distribution of DNA molecules behind the stacked sample. As seen in Figure 3-4, the sample's terminating boundary is visibly 'tilted' upon migrating through the pull back field of the cross-injector. By removing DNA molecules from the stacked sample plug, pull back voltages can hinder separations performed with low signal to noise ratios. Further, use of the protocol as described here wastes costly, and time-intensive DNA preparation unnecessarily.

Subsequent microscopy images illustrate the benefit of imposing a small time delay when applying the pull back voltage. Experiments indicate that DNA molecules within the channels of the cross-injector do not leak into the separation channel if V_{PB} is not applied immediately. Hence, a pull back voltage initiated 5 - 10 seconds after injection enables the complete migration of the sample plug into the separation channel without molecular loss or leakage from injector channels. The benefit of this delay has been experimentally verified for running voltages between 85 V/cm and 850 V/cm.

Intensity Profiles

The images in Figure 3-4 illustrate that differences in velocity are significant even during the sample stacking process. Further, differences in velocity largely influence the formation, and propagation of the stacked sample prior to its molecular separation. Although the images in Figure 3-4 provide excellent visual representations of stacking, the differences in molecular width and distribution of the stacked samples are better understood by using more quantitative methods. In this section, the intensity measurements of pixels located along the channel centerline in each image are plotted against their position in the channel, x, and time, t. We refer to these intensity graphs as DNA profiles and utilize them to represent the changing molecular distribution of the sample throughout its electrophoretic injection.

Profiles of the monodisperse sample during its electrophoretic injection are shown on the left-hand-side of Figure 3-6, while profiles of the spin-column-purified polydisperse sample are displayed on the right-hand-side. The figure is composed of 12 plots, where each set of 6 illustrates the distribution of DNA molecules within the sample at different times during its injection. The initial shape of the monodisperse sample at $t = 0$ s is rectangular, consistent with the uniform distribution obtained via sample-loading. As the electrophoretic injection progresses, the formation of the stacked sample is illustrated by a peak that grows in intensity near the terminating boundary of the sample plug. Its continuous growth represents the increasing number of molecules that begin to migrate within the concentrated stacked sample.

At the end of the injection, the overall profile of the sample resembles a Gaussian peak as shown at time $t = 3.0$ s.

Similarly, the more complicated stacking behavior of polydisperse molecules are represented by intensity profiles on the right-hand-side of Figure 3-6. At $t = 0$ s, the profile of the polydisperse sample is rectangular, consistent with the uniform distribution attained previously. At time $t = 1.0$ s, a sharp peak begins to develop at the terminating boundary of the sample plug as also displayed by the monodisperse sample. However, with increasing time, molecules within the peak advance towards the frontal boundary at a faster rate than surrounding molecules. At $t = 2.8$ s, the peak surpasses the frontal boundary producing a sharp frontal boundary and a diffusive terminating boundary. Later, at $t = 3.0$ s, the peak migrates quickly to create a disjointed profile. As seen, the polydisperse sample never develops the fully focused Gaussian distribution of stacked molecules exhibited by the monodisperse sample.

The profiles of both samples indicate there are populations of DNA molecules whose velocities vary with time throughout injection. This is expected as changes in the ion distribution within the injector causes time-varying changes in the potential gradients which act upon different populations of DNA at different times. As a result, DNA molecules experience different velocities at different locations within the sample plug. This point is well described by Figure 3-7 which illustrates the intensity profiles of the DNA sample plug at different points during its migration within the cross-injector.

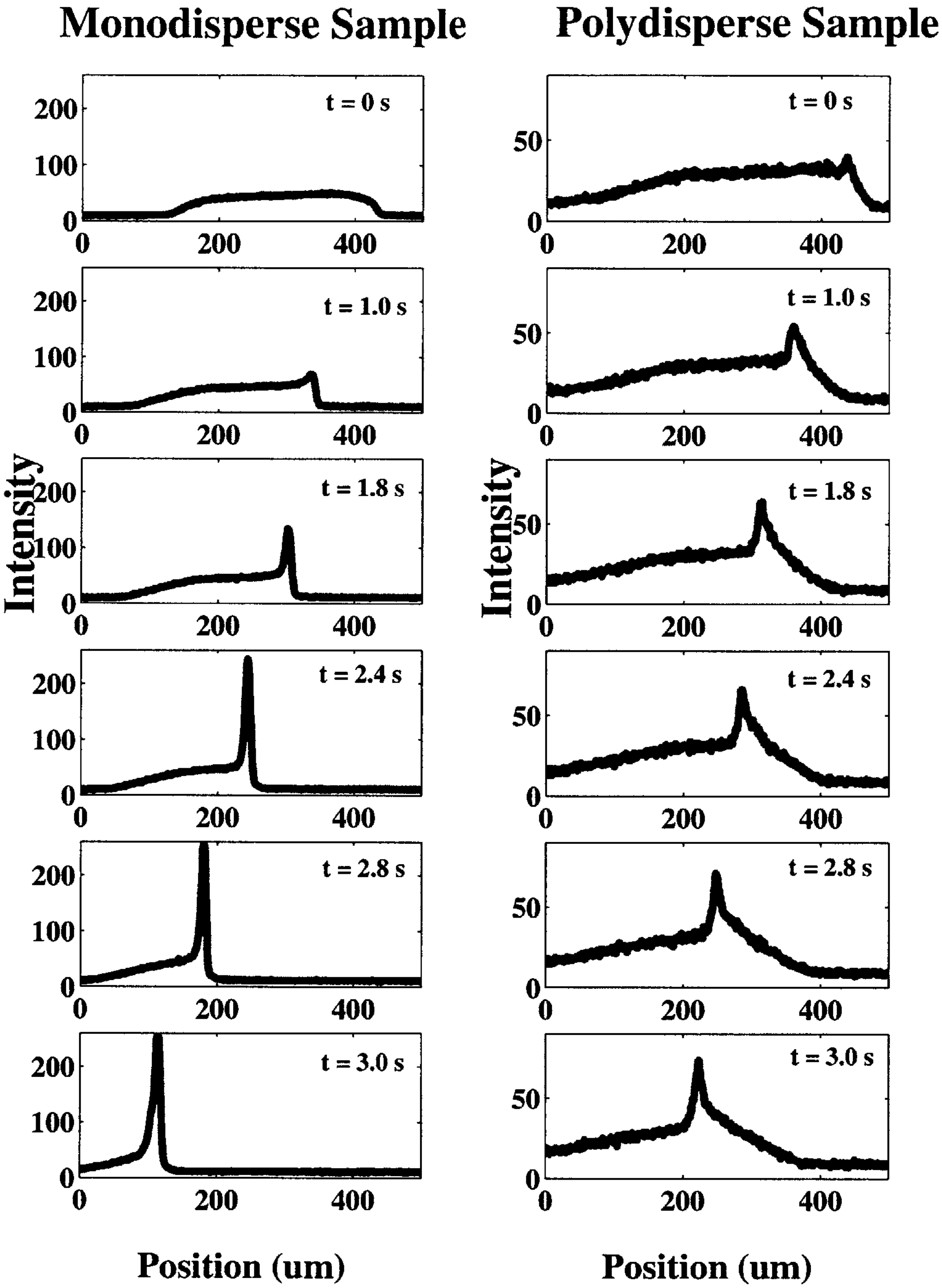

Figure 3-6: Measurements on the left-hand-side correspond to the intensity measurements gathered during the electrophoretic injection of the 10^{-10} M monodisperse DNA solution at 200 V/cm. The profiles on the right-hand side of the figure correspond to the intensity measurements taken during the injection of a 10^{-10} M polydisperse sample purified via spin columns.

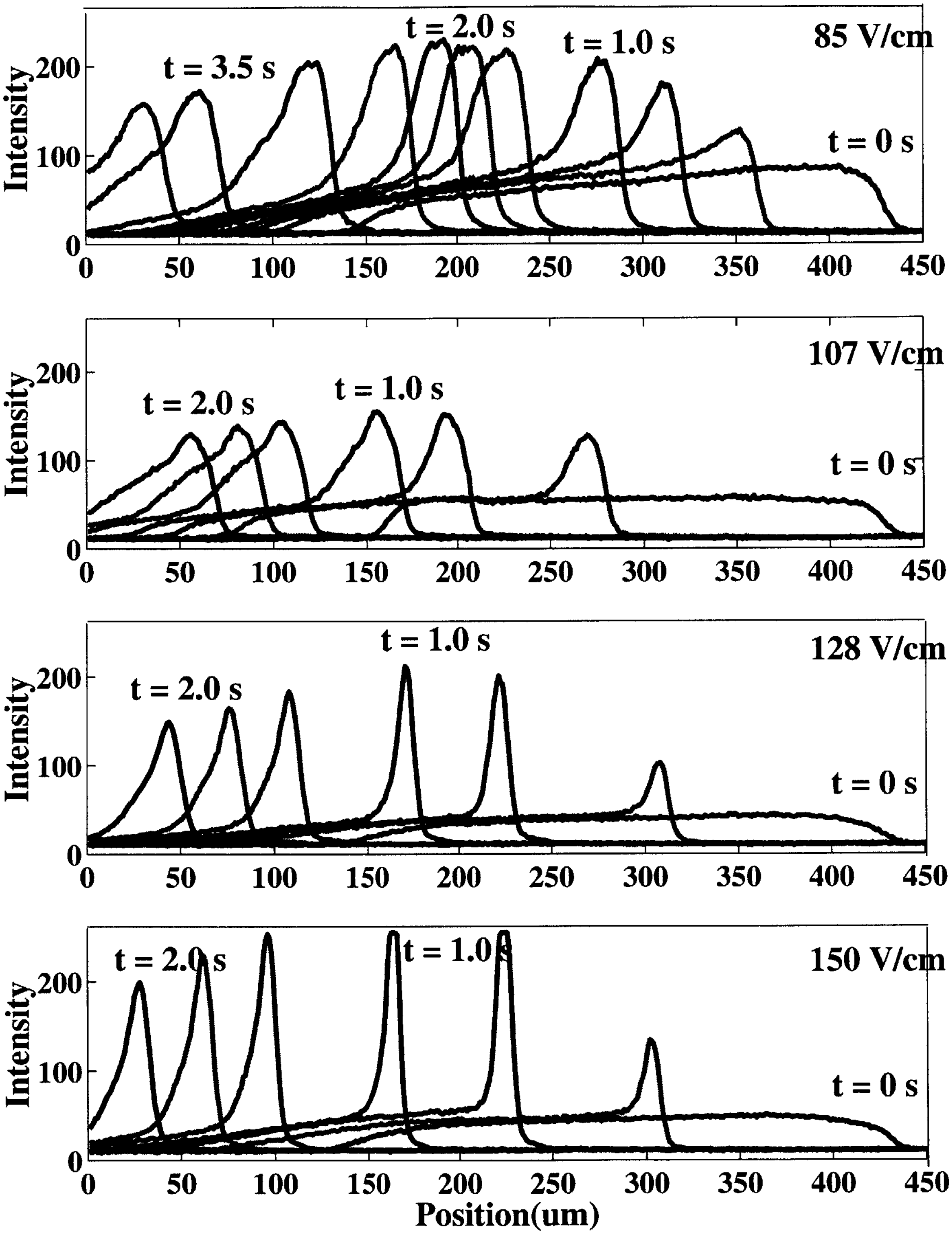

Figure 3-7: Intensity profiles of a DNA sample plug within a 250-μm-long-cross-injector at different stages during its migration. Profiles are shown for three different injection voltages of 85 V/cm, 135 V/cm and 150 V/cm.

3.4.3 The N-Gaussian Model

In order to describe the re-distribution of DNA molecules during electrophoretic injection, we take a finite element approach and divide the initial sample plug, at time $t = 0$ s, into N velocity domains. Gaussians are labeled 1 through N where the 1^{ST} Gaussian represents molecules which exhibit the slowest velocity, V_1, and the N^{TH} Gaussian describes the distribution of molecules that migrate with the fastest velocity, V_N. Consequently, the 1^{ST} Gaussian is located closest to the frontal boundary of the sample while the N^{TH} Gaussian is positioned nearest the sample's terminating boundary.

As the sample width decreases during injection, the potential gradients within the sample plug change similarly. Since the samples illustrate terminator-type stacking in Figure 3-4, the larger potential gradients of the sample plug are presumed to be at the terminating boundary. Initially, at time $t = 0$ s, the potential gradient is highest near the terminating boundary of the sample and decreases towards the frontal boundary. At some time $t = t_N$, the width of the sample plug is diminished, and the distribution of potential gradients within the sample is no longer identical to those observed at $t = 0$s.

In our model, as the terminating boundary approaches the frontal boundary during injection, the higher potential gradients associated with the stacked portion of the sample incrementally increase the velocity of molecules in its path. Since DNA accelerate incrementally under the approaching higher potential gradients, the population of DNA molecules within each Gaussian changes rapidly with time and position. That is, a molecule initially within the population of the $(N-1)^{TH}$ Gaussian, traveling with velocity V_{N-1}, is accelerated by the higher potential gradients approaching its position. This molecule then obtains a new, higher velocity, V_N, and transfers to the population of the faster moving N^{TH} Gaussian. Similarly, as the higher potential gradients approach the molecules within the $(N-2)^{TH}$ Gaussian, these molecules are accelerated to a higher velocity group, V_{N-1}. These molecules then quickly exit the slower $(N-2)^{TH}$ Gaussian and transfer within the adjacent $(N-1)^{TH}$ Gaussian. In this manner, molecules transfer within sequentially labeled Gaussians several times during injection. Consequently, populations of fast moving Gaussians steadily increase during the formation of the stacked sample while populations of slower Gaussians diminish to zero. Intermediate Gaussians, denoted 1 through $(N-1)$, therefore, represent regions of transient DNA velocity. Note, however, that all Gaussians are needed during the formation of the stacked sample to more accurately describe the re-distribution of DNA molecules based upon their velocity.

Intermediate Gaussians, denoted 1 through $(N-1)$, therefore, represent regions of transient DNA velocity. That is, these Gaussians represent the velocities of DNA molecules as they accelerate incrementally towards the highest velocity, V_N. Intermediate Gaussians 1 through $(N-1)$ do not exist in the final stacked sample because velocities V_1 through V_{N-1} are not steady state velocities of any of the molecules within the sample. Note, however, that all Gaussians are needed during the formation of the stacked sample to more accurately describe the unique re-distribution of DNA molecules based upon their velocity. Further, due to the changing potential gradients within the sample plug, the number of molecules that transfer out of a particular Gaussian does not equal the number of molecules that transfer into it. Molecules continue to transfer towards faster migrating Gaussians until they obtain, V_N. Consequently, populations of fast moving Gaussians steadily increase during the formation of the stacked sample while populations of slower Gaussians diminish to zero.

N-Gaussians of the Monodisperse Sample

The model is now used more specifically to describe the electrophoretic injection of the mono- and polydisperse samples, respectively. Importing the data obtained from the intensity profiles into Matlab, the molecular distribution of the sample plug at each time step is decomposed into 10 Gaussian velocity groups as shown on the right-hand-side of Figure 3-8. The 1^{ST} Gaussian represents the motion of DNA molecules nearest the frontal boundary of the sample while the 10^{TH} Gaussian represents those molecules nearest the sample's terminating boundary. Using Matlab, a mathematically fit is made to the area of the sample plug with minimum error. At time $t = 1.8$ s, an increasing number of molecules are accumulated within the 10^{TH} Gaussian as its intensity increases rapidly. Similarly, the amplitude and location of all intermediate Gaussians change rapidly as a larger number of molecules are transferred towards the 10^{TH} Gaussian. During this time, the number of Gaussians needed to describe the different velocities of the sample is reduced from the initial N = 10, to N = 5 as seen by the Gaussian decomposition shown at time $t = 2.4$ s. Molecules of intermediate Gaussians continue to transfer rapidly within adjacent populations until they migrate with an increased velocity, V_N and accumulate within the population of the 10^{TH} Gaussian. As additional molecules continue to transfer towards the 10^{TH} Gaussian, the final stacked sample plug seen at time $t = 3.0$ s is represented by one large Gaussian at the sample's terminating boundary and one rather small Gaussian near the frontal boundary.

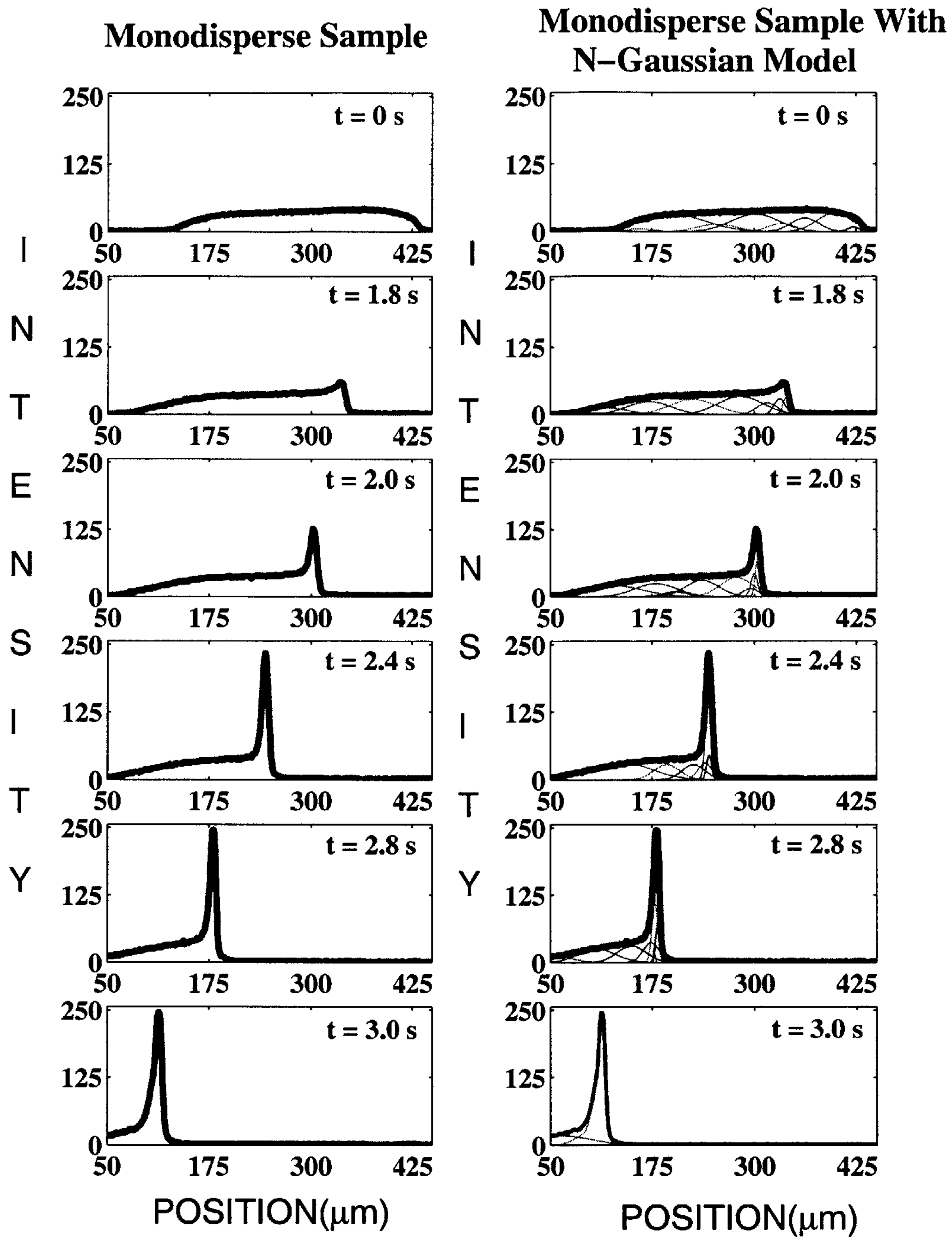
Monodisperse Sample

Monodisperse Sample With N–Gaussian Model

Figure 3-8: Measurements correspond to the electrophoretic injection of the 10^{-10} M monodisperse DNA solution at 200 V/cm. The profiles on the left-hand side of the figure represent values of intensity measured from pixels located along the centerline of the channel. The set of profiles on the right-hand-side illustrate the N-Gaussian Model applied to the monodisperse sample. The sample plug was divided into N = 10 Gaussians at time $t = 0$ and each subsequent image was numerically decomposed into the minimum number of Gaussians needed in order to describe the various of regions of electrophoretic velocity during injection. As seen, DNA molecules are accumulated within 1 larger Gaussian by the end of the injection.

N-Gaussian Model of the Polydisperse Sample

The model can also describe the formation of the stacked sample for polydisperse solutions such as sequencing reactions. However, in this case, the numerous molecular lengths increase the complexity of DNA re-distribution during injection, as molecular lengths vary by two orders of magnitude in our samples. Using the N-Gaussian Model, the stacking of the sample plug is again described by the migration of 10 Gaussian velocity groups positioned in between the frontal and terminating boundaries as described earlier. Just as before, molecules able to accelerate to the fastest group velocity, V_N, transfer into the population of the N^{TH} Gaussian. However, molecules separate according to molecular weight and distinct velocity groups develop within the injector.

As seen in Figure 3-9, molecules from the sequencing reaction quickly transfer within N = 10 Gaussians to exhibit N = 7 distinct Gaussians by time $t = 1.0$ s, and N = 4 Gaussians at time $t = 1.8$ s. However, by $t = 2.0$ s, the remaining dynamics of the injection are well described by 3 stongest Gaussians. Unlike the monodisperse sample of Figure 3-8, molecules of the polydisperse sample do not accumulate into a single final velocity group.

Correlation with DNA Sequencing Results

A typical electropherogram for a sequencing reaction, labeled with Big-Dye-Terminators, displays a series of small, individual peaks followed by large peak at the end of the experiment as shown in Figure 3-10. Each peak represents the fluorescence intensity emitted by a particular population of DNA molecules with the same number of bases in length. The large peak seen at the end of the electropherogram represents the failure of molecular sieving for

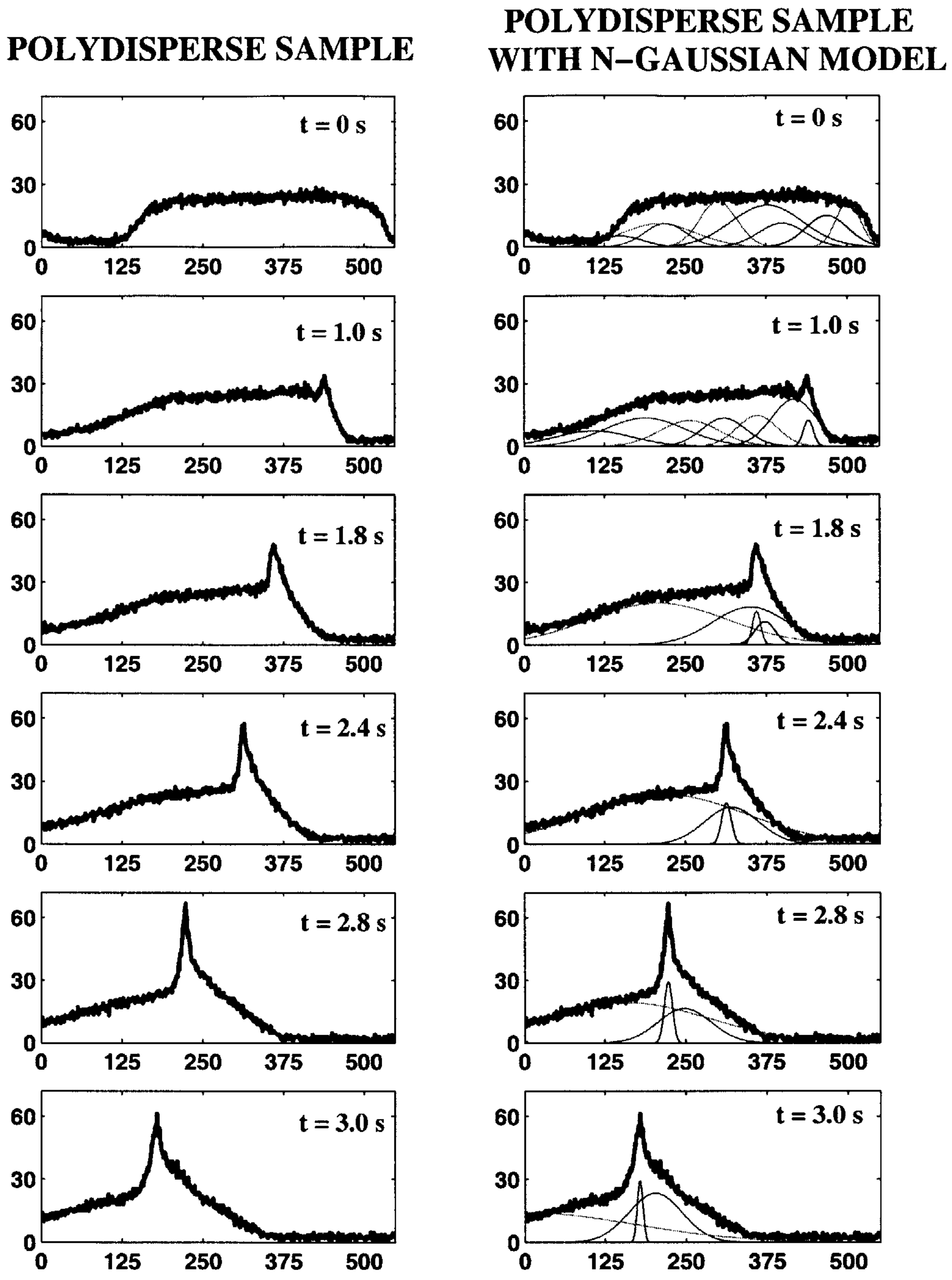

Figure 3-9: Measurements correspond to the electrophoretic injection of the 10^{-10} M polydisperse DNA solution at 200 V/cm. The profiles on the left-hand side of the figure represent values of intensity measured from pixels located along the centerline of the channel. The set of profiles on the right-hand-side illustrate the N-Gaussian Model applied to the polydisperse sample. The sample plug was initially divided into N = 10 Gaussians at time $t = 0$ and each subsequent image was numerically decomposed into the minimum number of Gaussians needed to represent the different regions of electrophoretic velocity during injection. As seen, the dynamics of sequencing reactions are largely represented by 3 distinct Gaussians throughout injection. This is called the modified N-Gaussian Model.

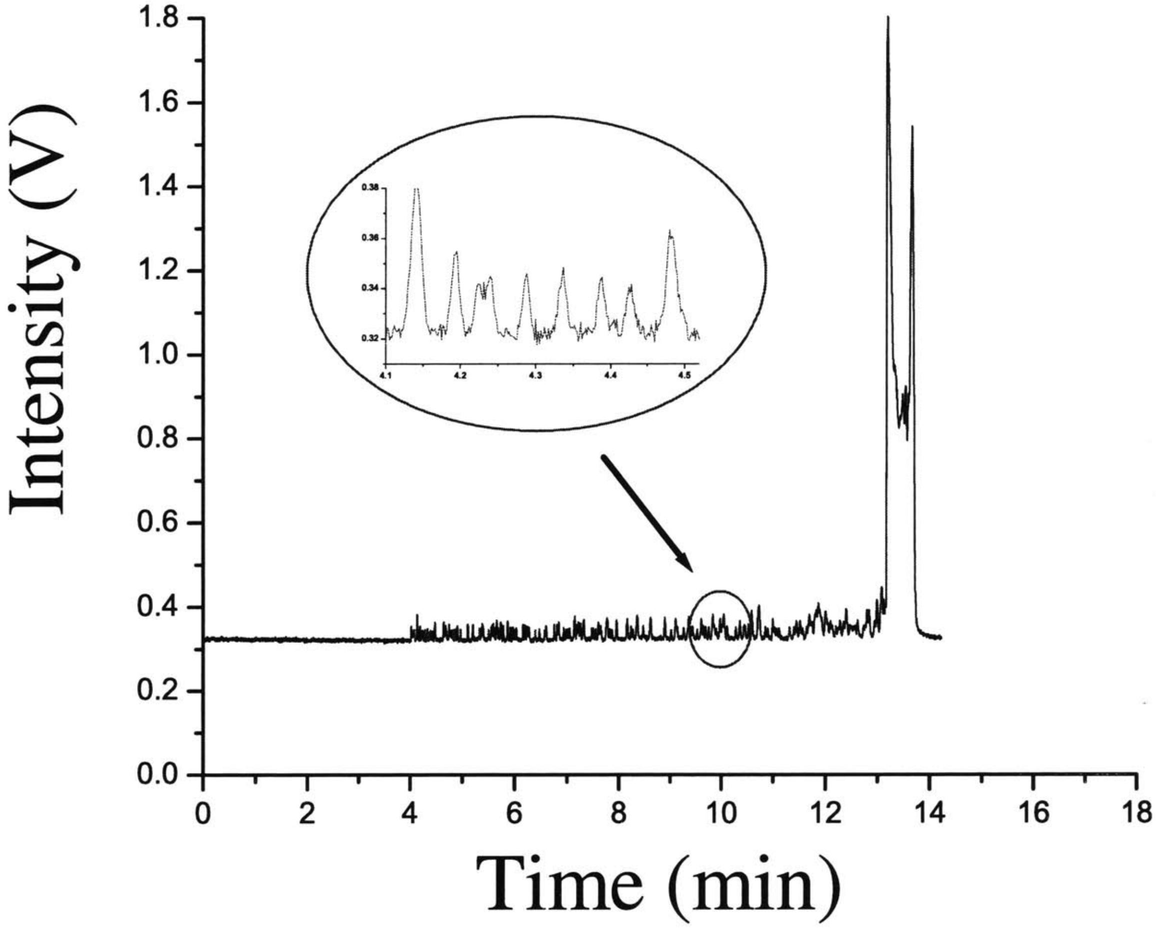

Figure 3-10: A representative electropherogram displays the results of a separation performed with a 10^{-10}M sequencing reaction, labeled with Big-Dye-Terminators and purified using spin columns. Electrophoresis was performed at 50^o C within a 12-cm-long device following a 3-minute pre-electrophoresis, and subsequent 3-minute sample-loading, both at 300 V/cm.

large molecules, usually attributed to reptation.

By plotting the velocity, u, against DNA size, N, on a log-log scale, three velocity domains

Table 3.2: Different measurements of velocity for DNA molecules of various sizes obtained from the electrophoretic injection of polydisperse samples within 250 μm injector offset. Superscripts denote spin column purification, S and ethanol precipitation, E, respectively. The parameter V_A represents velocities obtained analytically using the most appropriate expression for electrophoretic migration, V_E illustrates those velocities measured experimentally from electrophoregrams, and V_{NGM}, represents velocities measured using the N-Gaussian Model representation of the sample zone.

DNA Length (Bases)	V_A^S (cm/s)	V_E^S (cm/s)	V_{NGM}^S (cm/s)	V_A^E (cm/s)	V_E^E (cm/s)	V_{NGM}^E (cm/s)
30	0.032	0.029	0.030	0.034	0.29	0.036
182	0.028	0.026	0.025	0.029	0.026	0.025
300	0.026	0.025	0.025	0.027	0.025	0.021
517	0.024	0.023	0.025	0.025	0.023	0.020
800	0.0095	0.009	0.0089	0.0091	0.0084	0.0076

are evident for small, medium, and larger sized molecules. The electrophoretic velocities of the smallest molecules within the sequencing reaction demonstrate a negative dependence on size. The velocity of the next set of molecules is inversely proportional to size, and the velocity of the largest molecules is altogether independent of size. The simplest assignment for this distribution corresponds to the classical modes of migration via molecular sieving [92], [106], reptation with orientation [41] [91], and reptation without orientation [44], [42].

Since DNA molecules of a polydisperse sample illustrate 3 distinct velocity domains in the electropherogram measured at the exit of the separation channel, the same populations emerge during stacking within the cross-injector. That is, the fastest Gaussian in the injector represents the migration of the smallest molecules which transport via molecular sieving. The intermediate Gaussian represents the reptative migration of longer molecules, and the slowest Gaussian illustrates the motion of the longest molecular fragments via reptation without orientation. The detailed comparison is made in Table 3.2.

In the table, the velocity of each Gaussian is obtained by plotting the position of its mean as a function of time and then measuring the slope. The velocities calculated using Gaussian measurements are directly compared to the velocities recorded in our own electropherograms under identical running conditions. For example, a molecule that is 30 bases long exhibits a velocity of 0.029 cm/s on an electrophoregram, and has an analytical velocity of 0.0033 cm/s obtained via molecular sieving [10]. Similarly, the velocity exhibited by the N^{TH} Gaussian in the model is 0.031 cm/s. Note that the velocity derived using the N-Gaussian Model cannot compare exactly to the velocity obtained from electrophoregrams because it represents the group velocity of a Gaussian distribution of DNA fragments, not that of the individual 30-base-long molecule. However, as seen in Table 3.2, the velocities obtained using the model are well within 5% of the velocities measured experimentally from the electropherograms. This suggests that the strong fields and ion gradients that induce stacking in the injector are dissipated relatively quickly and that a time-averaged velocity similar to the final migration velocity is reached after only several seconds of injection.

Further support for this assignment velocity groups in the injector can be obtained from an area analysis as seen in Table 3.3. The areas underneath the different peaks of the electropherogram determine the percentage of the total signal attributed to molecules of different sizes. Performing the size-based analysis previously described by Heller [44], 21% of the total signal is obtained from DNA molecules less than 150 bases in length, 27% can be attributed to fragments longer than 800 bases and the remaining 52%, is recorded from the fluorescent detection of fragments 150 - 800 bases in length. The signal distribution of the 3 Gaussians similarly mimics these results with values of 18%, 35%, and 47% respectively.

The most significant contribution obtained from the intensity profiles and Gaussian de-

Table 3.3: Comparision of the signal distribution obtained via the N-Gaussian Model, to the molecular composition of DNA samples.

DNA Size (b)	% of Sample	% of Signal
$10^1 - 10^2$	21	18
$10^2 - 10^3$	52	47
10^3+	27	35

composition is the newly-found ability to describe the stacking process quantitatively and continuously during electrophoretic injection. Using the N-Gaussian Model, the relative position, area, and width of each Gaussian can be measured and compared to those values determined from different operational parameters. The N-Gaussian Model produces numerical quantities that enable the direct comparison and analysis of DNA stacking behavior induced by different protocols, device designs and experimental parameters.

As seen from Figure 3-9, the migration of DNA samples comprised of sequencing reactions can be described by 3 distinct Gaussians. Using these results, the migration of the DNA sample plug can be represented by three Gaussians from the beginning of the injection at time $t = 0$s. The left-hand-side of Figure 3-11 illustrates the migration of a polydisperse DNA sample purified by spin columns within a 250μm-long-injector. Three Gaussians denote the migration of various DNA molecules within the sample plug as well as exhibit their distinct stacking properties. Similarly, the migration of a polydisperse DNA sample purified via ethanol precipitation is shown in the right-hand-side of Figure 3-11.

Additional experiments also illustrate the migration of DNA samples within a 500μm-long-offset of a cross-injector. Figure 3-12 represents these dynamics using the N-Gaussian model as in Figure 3-11. However, as seen from the figures, much of the dynamics are

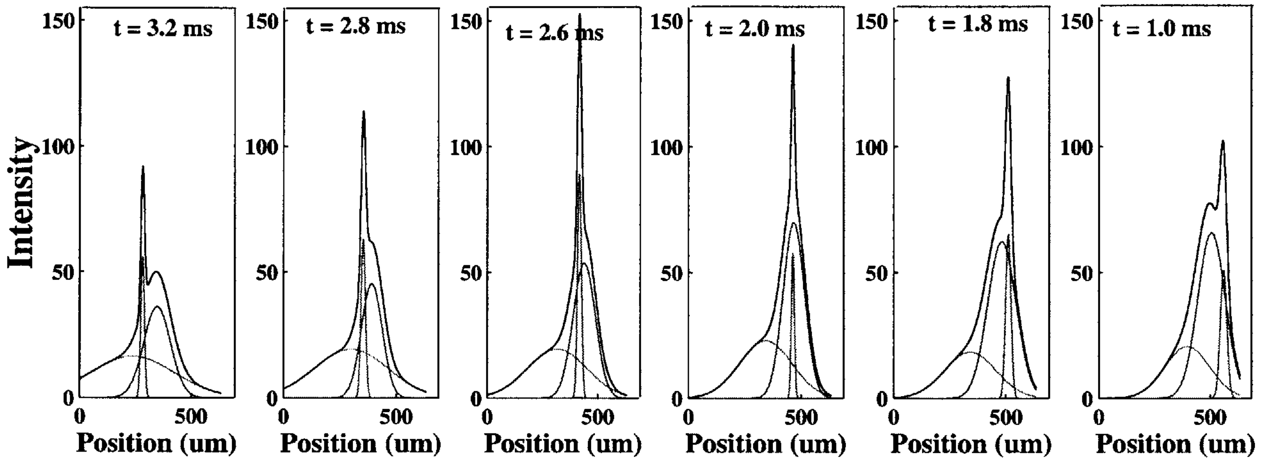

Spin–Column–Purified Polydisperse Sample

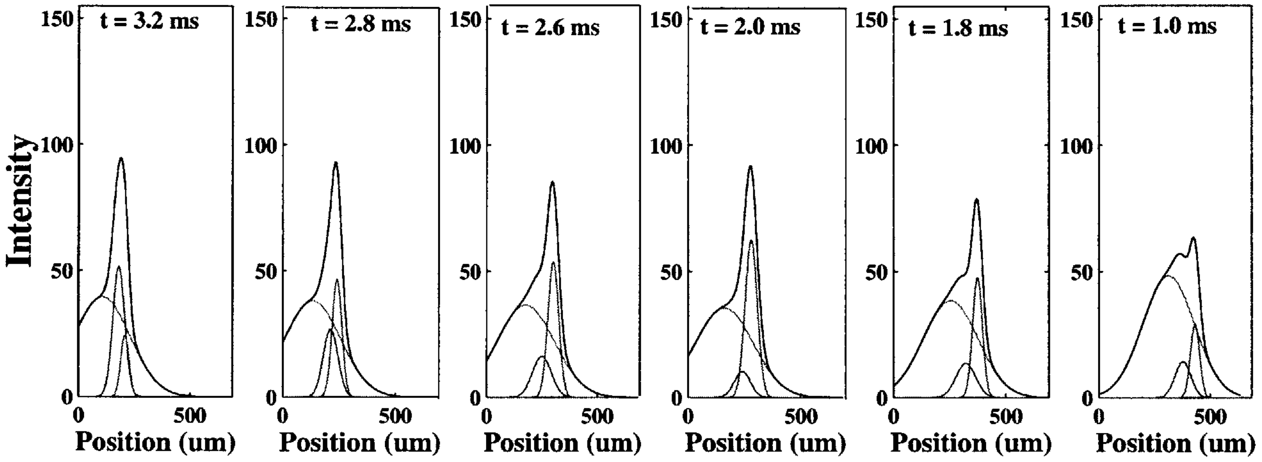

Ethanol–Precipitated Polydisperse Sample

Figure 3-11: The set of images on the left-hand-side use the N-Gaussian model to describe the electrophoretic injection of a polydisperse DNA sample purified with spin columns. An identical injection using a polydisperse DNA sample purified via ethanol precipitation is represented by the N-Gaussian model on the right-hand-side of the figure. Both injections were performed within a 250μm-long-offset of a cross-injector.

lost using a 500μm-long-offset because a large percentage of the DNA sample plug exits the field of view of the microscope using a 10X objective lens. These experiments would be greatly enhanced using a lower magnification. Despite this limiatation, the N-Gaussian model continues to provide a very good qualitative representation of the injection.

Although complete sample-loadings, injections and separations were performed under applied voltages ranging between 85 V/cm and 850 V/cm, the N-Gaussian Model is most distinguishable for experiments performed under typical electrophoretic fields of strength between 85 V/cm and 350 V/cm and within 250μm-long cross-injector offsets. Based upon the present research, polydisperse DNA samples do not develop one Gaussian distribution of molecules unless fields upwards of 700 V/cm are applied during injection. As will be described shortly, new high voltage injection protocols can be used to stimulate this dynamic condition, resulting in better resolution.

3.4.4 Stacking Width and Stacking Parameter

In the analysis above, the Gaussian width of each velocity group is left as a time-evolving parameter. This width can be used to quantify the effect of sample concentration by stacking. Using this approach, we define a stacking parameter, P_S, to represent the percent change in the width of the distribution:

$$P_S = \frac{W_I - W_F}{W_I} \times 100\% \tag{3.9}$$

where W_I is the width of the initial distribution of DNA molecules prior to electrophoretic injection, and W_F is the width of the final DNA distribution when injection is completed.

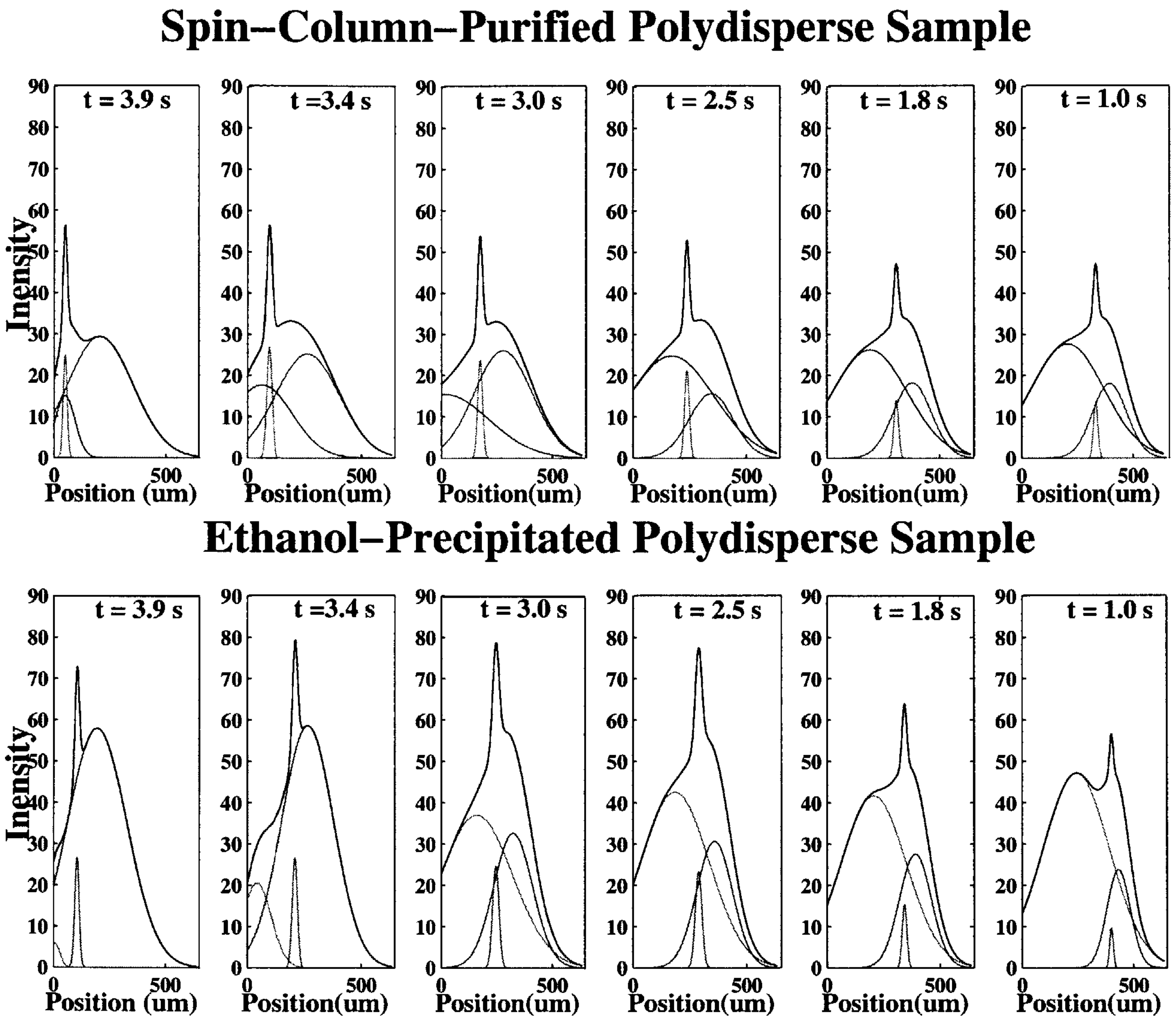

Figure 3-12: The set of images on the left-hand-side use the N-Gaussian model to describe the electrophoretic injection of a spin-column-purified polydisperse DNA sample within a 500μm-long-offset of a cross-injector. An identical injection using a polydisperse DNA sample purified via ethanol precipitation is represented by the N-Gaussian model on the right-hand-side of the figure.

Since DNA molecules are uniformly distributed within the cross-injector during sample-loading, the width of the initial distribution of all molecules is well represented by the offset length of the injector used. The final distribution of particular molecules of interest is then measured using the standard deviation, or width, of the appropriate Gaussian. Table 3.4 displays the different values of P_S exhibited by molecules of the polydisperse sample during electrophoretic injections utilizing 3 different injector lengths, 4 different applied loads, and two methods of sample purification. Note, all data utilized the same 1xTTE buffer and 2% (w/v) solutions of LPA as the sieving matrix.

As seen from Table 3.4, during an electrophoretic injection at 300 V/cm, using samples purified via spin columns and a 250-μm-long injector, smaller DNA fragments re-distributed to develop a Gaussian profile whose width was less than 20% of the width of the original sample plug. Similarly, molecules within the intermediate Gaussian stacked to generate a sample plug whose width was less than 35% of the original sample. Closer inspection of Table 3.4 illustrates the Gaussian distributions of all molecules become increasingly narrow under larger applied voltage. Further, smaller DNA molecules are always more tightly stacked than medium and larger sized molecules regardless of the experimental conditions imposed.

Empirical Tool for Stacking Estimates

Experimentally measured values of P_S are compared against the stack velocity, V_{ST} because it incorporates, injector length, conductivity, DNA size, and run voltages as described in section 2.4. In this manner, it is possible to incorporate all particular parameters of interest

Table 3.4: Experimentally measured values of stacking parameters obtained from the electrophoretic injection of polydisperse solutions within 250 μm injector. The applied run voltage is represented by V_{RUN}, the final width of a Gaussian distribution of DNA molecules is denoted by W_F, and the percentage of stacking exhibited by DNA molecules is represented by the parameter, P_S. Superscripts of S and E represent polydisperse reactions purified via spin columns and ethanol precipitation respectively.

Gaussian (-)	V^S_{RUN} (V/cm)	W^S_F (μm)	P^S_S (%)	V^E_{RUN} (V/cm)	W^E_F (μm)	P^E_S (%)
N^{TH}	150	86	65.6	150	98	60.8
	200	81	67.6	200	92	63.2
	250	74	70.4	250	83	66.8
	300	68	72.8	300	74	70.4
	350	61	75.6	350	70	72.0
$(N-1)^{TH}$ (Intermediate)	150	184	26.4	150	198	20.8
	200	172	31.2	200	182	27.2
	250	161	35.6	250	175	30.1
	300	150	40.8	300	160	36.0
	350	143	42.8	350	149	40.4
1^{ST} (Frontal)	150	240	4.1	150	245	2.0
	200	239	4.4	200	243	2.8
	250	238	4.8	250	243	2.8
	300	237	5.2	300	240	4.1
	350	237	5.2	350	239	4.4

into one value and use it to estimate the level of stacking their protocols will produce. Measurements of the stacking parameter, P_S, are plotted against the values of stack velocity, V_{ST}, in Figure 3-13. Note that values of V_{ST} were determined using analytical values of all empirical constants found in general electrophoresis texts. These values are also represented in Table 3.4.

As seen, the stacking dynamics of each population of molecules remain distinct. This graph indicates that smaller DNA molecules will always stack more readily than medium or longer sized molecules regardless of the injector, sample purification or applied voltages used. Figure 3-13 also illustrates that few combinations of experimental parameters can induce any significant level of stacking within the population of longest molecules. By representing the stacking behavior of DNA molecules in this manner, it is possible to use Figure 3-13, at least qualitatively, to develop new electrophoretic protocols, design new microdevices, or experiment with new operational parameters to achieve better stacking for molecules of interest. For example, from Figure 3-13 it is seen that for forensic science, one can obtain more concentrated stacked samples by utilizing smaller injectors and higher voltages. For sequencing, it is possible to obtain more concentrated stacked samples by utilizing DNA purified via spin columns, therefore of higher conductivity, and elevated run voltages. Similarly, researchers interested in the separation of the largest molecules can see from Figure 3-13, that significantly larger voltages are needed to induce any level of stacking within the semi-dilute LPA solutions described here.

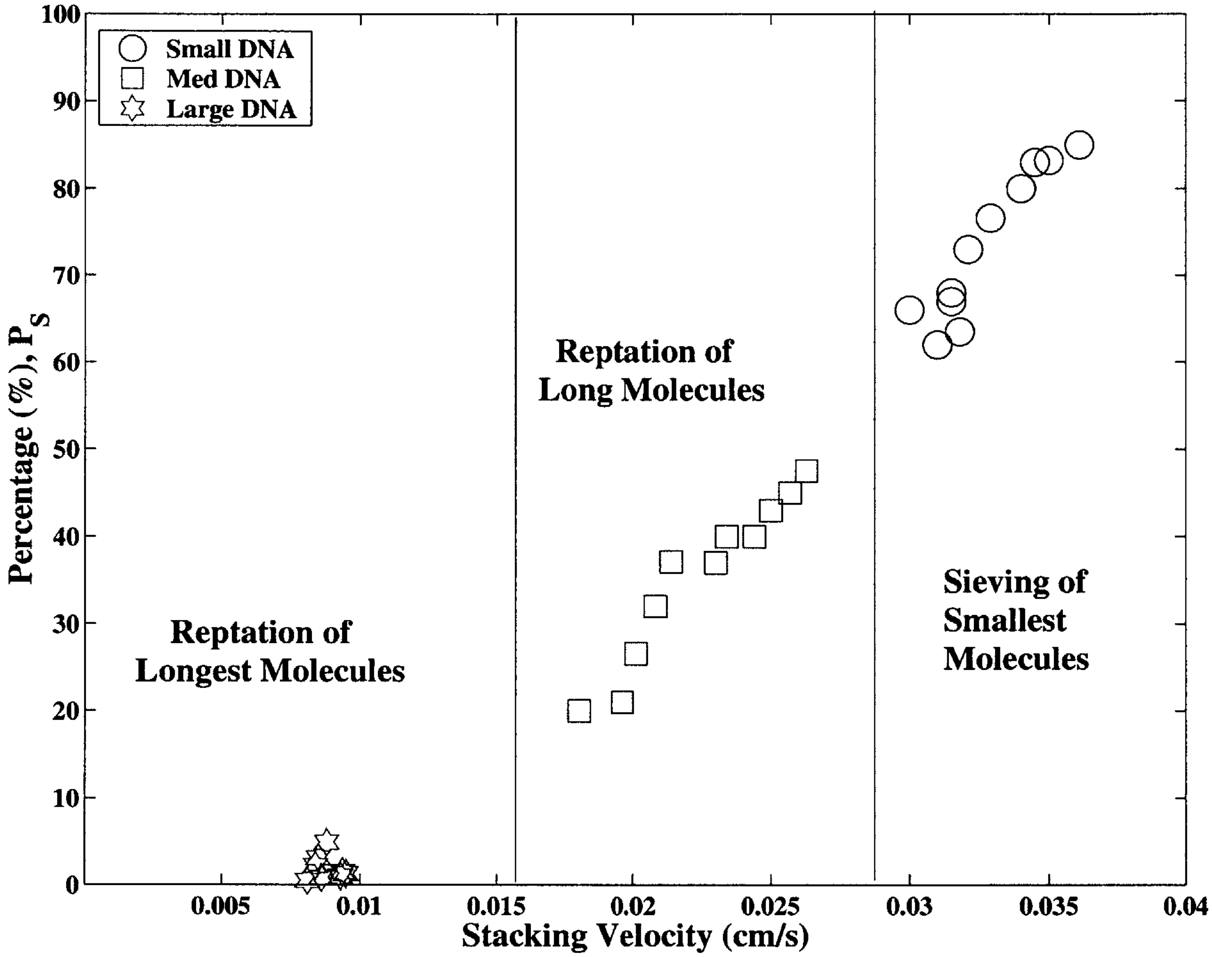

Figure 3-13: The changing width of each DNA distribution is experimentally measured as a percentage of its initial width prior to injection, P_S, and plotted against analytically determined values of its stack velocity. The graph incorporates all possible permutations of injector length, sample purification, applied voltage and DNA size. Circular markers represent the measurements of smaller DNA molecules, while measurements of medium-sized and larger molecules are illustrated by square and star-shaped markers respectively.

3.4.5 High Voltage Injection Protocol

The negative effects of high voltages, V_R, at the separation stage have been documented by numerous researchers [149], [10], [144]. Experiments performed under the influence of high fields exhibited lower levels of resolution and selectivity due to the breakdown of selective sieving and earlier onset of biased reptation [158]. As a result, typical run voltages applied during electrophoresis are kept below $\sim$ 200 V/cm in order to maintain longer read lengths [150]. However, our newest experiments indicate that short periods of high voltage during injection are not necessarily destructive to the quality of DNA separations, as we shall elaborate below.

Conventional separations are performed using 4 consecutive steps: pre-electrophoresis, sample-loading, electrophoretic injection, and separation, characterized by V_P, V_L, V_I, V_R, respectively. During pre-electrophoresis, a large potential gradient of several hundred volts per centimeter, V_P, is first imposed between the cathode and anode ports of the device in order to evenly distribute ions of the buffer solution within the separation channel. Afterwards, the same potential gradient, V_P, is applied along the sample and waste reservoirs of the cross-injector before DNA molecules have been introduced into the microdevice. During this stage, de-ionized water is placed in the sample reservoir in order to deplete buffer ions located within the offset of the cross-injector and replace them with a zone of water ions having a lower conductivity. Previous research has indicated that this protocol induces a low-conductivity zone within the cross-injector that facilitates better sample-loading and subsequent stacking of DNA molecules [155], [152].

Following pre-electrophoresis, purified DNA solutions are drawn into the cross-injector using a load voltage, V_L. This sample-loading is generally performed for 3 minutes in order to generate a uniform distribution of DNA molecules within the cross-injector offset [5]. After this time, the load voltage is turned off, and a higher run voltage, V_R is imposed between the cathode and anode ports of the microdevice. This voltage initiates electrophoretic injection and leads into the final step of overall separation of DNA molecules.

The experiments described here utilize a new protocol which incorporates a distinct injection voltage, V_I, to introduce DNA molecules into the separation channel, and a separate run voltage, V_R for separation. Values of V_P, V_L and V_R, remain identical to those used during conventional electrophoresis, but the newly applied injection voltage, V_I can be significantly greater than V_R. In order to prevent voltage-induced degradation of the sequencing separation, V_I is turned off after 5 seconds and a more typical run voltage, V_R, is applied.

Digital Images

Figure 3-14 demonstrates the shape of the stacked sample at the exit of a 250-μm-long cross-injector offset after electrophoretic injection was performed using 6 different values of injection voltage, V_I. The set of six images on the left-hand-side displays the digital image of the sample plug obtained through video microscopy. The corresponding set of images on the right-hand-side display the flourescence intensity of each molecular distribution within the sample plug as measured along the channel centerline. Images are arranged in order of increasing injection voltage as indicated by the values of V_I on the upper-left-hand corner. The image of the final stacked sample obtained using V_I = 236 V/cm is shown first, followed by images of stacked samples obtained using increasing injection voltages up until V_I = 708

V/cm. In each image, the sample arm of the cross-injector is seen on the upper-right-hand-side while the waste arm is shown on the lower left. The cathode and anode are located at the far right and left, respectively, of the main separation channel oriented horizontally in each image. The digital images visually represent the molecular re-distribution of the sample when electrophoretic injection is complete. As seen, the distribution and overall width of the sample zone decrease quickly with increasing voltage.

The first image taken using an injection voltage of V_I = 236 V/cm represents the conditions derived using run voltages only slightly higher than conventional values of V_R. As seen, the width of the sample plug is fairly wide and its molecules exhibit 3 visually distinguishable regions of DNA as discussed extensively in section 4.3. Using V_I = 394 V/cm, the width of the sample plug is slightly decreased and its distribution of DNA is significantly more compact. The electrophoretic injection performed using V_I = 473 V/cm is the first to illustrate the improved stacking dynamics desired. Here, 92% of the stacked sample area is represented by 1 Gaussian distribution, while only traces of DNA molecules are unstacked. The stacked saples developed using injection voltages of 552 V/cm, 630 V/cm, and 709 V/cm demonstrate decreasing widths and increasingly concentrated sample plugs. From the data illustrated in Figure 3-14, the distribution of all DNA molecules is identically Gaussian when electrophoretic injection is performed using $V_I \geq 630$ V/cm. Measurements of the final width of the sample plug, W_F, and corresponding full width at half-maximum analysis, W_{FWHM}, are shown in Table 3.5.

Overall, the results of Figure 3-14 demonstrate the ability of the electrophoretic system to generate a stacked sample during injection. Clearly, the formation of one Gaussian distri-

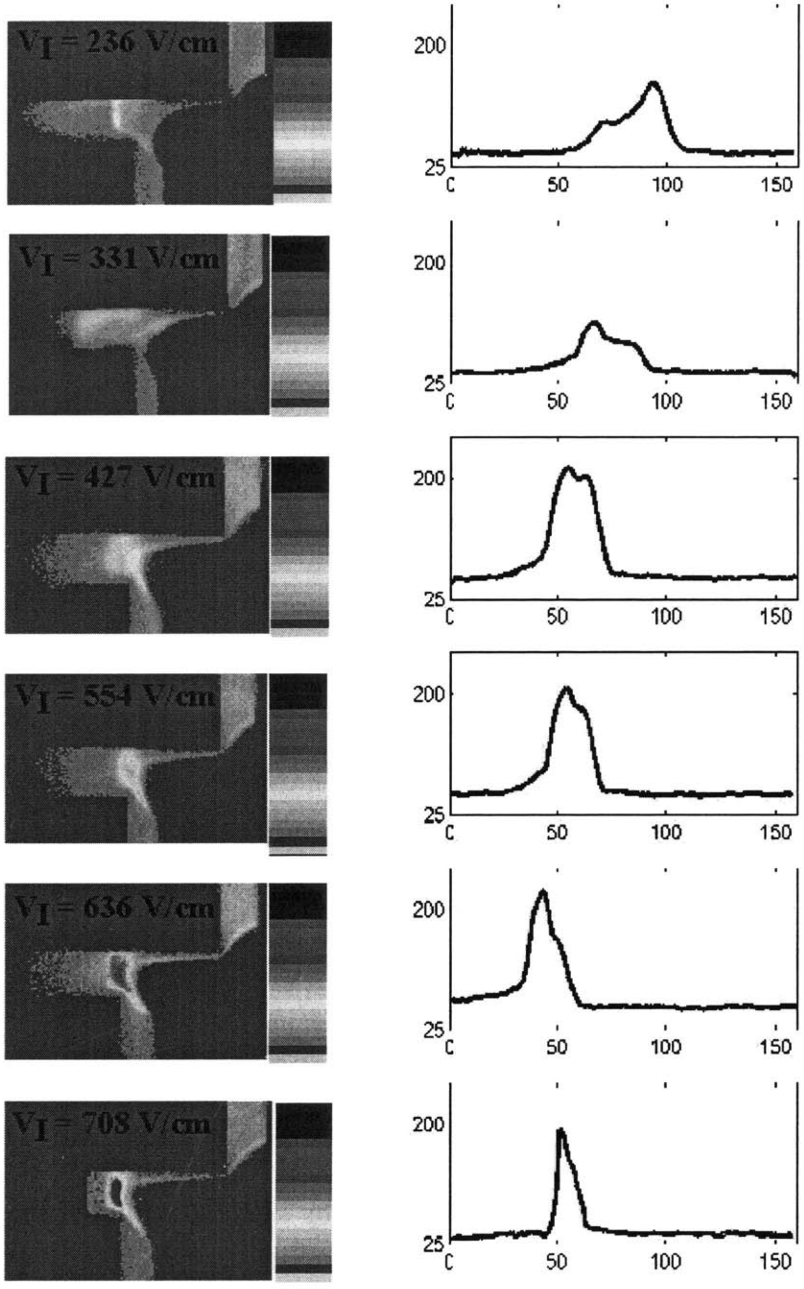

Figure 3-14: The set of digital images on the left-hand-side represent the shape of the sample plug at the end of electrophoretic injection as captured via video microscopy. Each image illustrates the final stacked sample generated by using a new high-injection protocol. The different values of V_I used for each experiment are shown in the upper left corner of the images. The right-hand-side of the figure illustrates the mathematical representation of each stacked sample as described by its intensity measurements.

Table 3.5: Measured widths of stacked sample plug, W_F, exhibited by electrophoretic injections during high voltage protocol, V_I. Sample widths were determined via microscopy measurements of the entire sample plug, while intensity measurements provided an additional full-width at half-maximum analysis representation, W_{FWHM}. Sample-loading was performed for a 3-minute period at 300 V/cm prior to injection for all experiments.

V_I (V/cm)	W_F (μm)	W_{FWHM} (μm)
236	73	–
394	62	–
426	55	21
554	51	19
630	40	15
708	27	9

bution was accomplished with higher voltages because the large potential gradients within the sample plug were sufficient to increase the velocity of all sequencing fragments to a value exclusively dependent upon the applied field. The next step is to test the practical benefits of increasingly concentrated stacked samples.

Resolution Data

The beneficial effects of stacking on actual DNA separations depend upon the experimental conditions and limitations of the apparatus. For example, in seaquencing there are typically domains of molecular read length that are limited by injected sample plug length, diffusive broading of the injected plug, and the spatial resolution of the detector. Stacking can have significant benefits so long as the electrophoretic result is limited by the first aspect, the sample plug length. Table 3.4 illustrates with a typical example. In this case, separations were performed within a microdevice comprised of a 11.5-cm-long separation channel and a 250-$/mu$m-long cross-injector, using a run voltage of $V_R = 150$ V/cm, and estimated detector resolution of $\sim 200\mu$m. Distinct injection voltages of $V_I = 236$ V/cm, 554 V/cm, and 708

V/cm were used, respectively, as shown.

Under the experimental conditions of Table 3.4, the sequencing results for DNA molecules 150 to 300 bases in length benefited significantly from increased stacking as seen in Figure 3-15. In this case, a 35% increase in peak resolution was observed for these mid molecular weights due to increased stacking. This is because, for this apparatus and run conditions, the results for longer and shorter molecular size are limited by factors other than the injection plug length. The optimal benefits of stacking and optimal channel geometry will depend upon a detailed match of the channel geometry and experimental conditions with the desired assay. This can be determined using the analysis presented above.

Although the resolution of long fragments in particular was largely increased by the improved stacking induced by high voltage protocols, Table 3.6 illustrates there is no significant increase in the overall read-length of each separation. That is, 400 bases of DNA were separated within each 12-cm-long device filled with 2% LPA regardless of which injection voltage was used. Furthermore, the range of molecules separated remains largely the same indicating the injection voltage does not affect the molecular range of DNA molecules separated. Lastly, signal to noise ratios remained nearly identical for all separations.

However, the sharp increase in resolution seen in Table 3.6 may be of great importance to forensic and genotyping applications. These methods operate with a relatively limited range of DNA sizes, 100 - 400 bases, and require minimum resolution values of ~ 0.8. A combination of a concentrated polymer matrix, e.g. 4% LPA, and an optimized sample stacking protocol should be particularly beneficial for these applications. Experiments for these specific areas are currently ongoing.

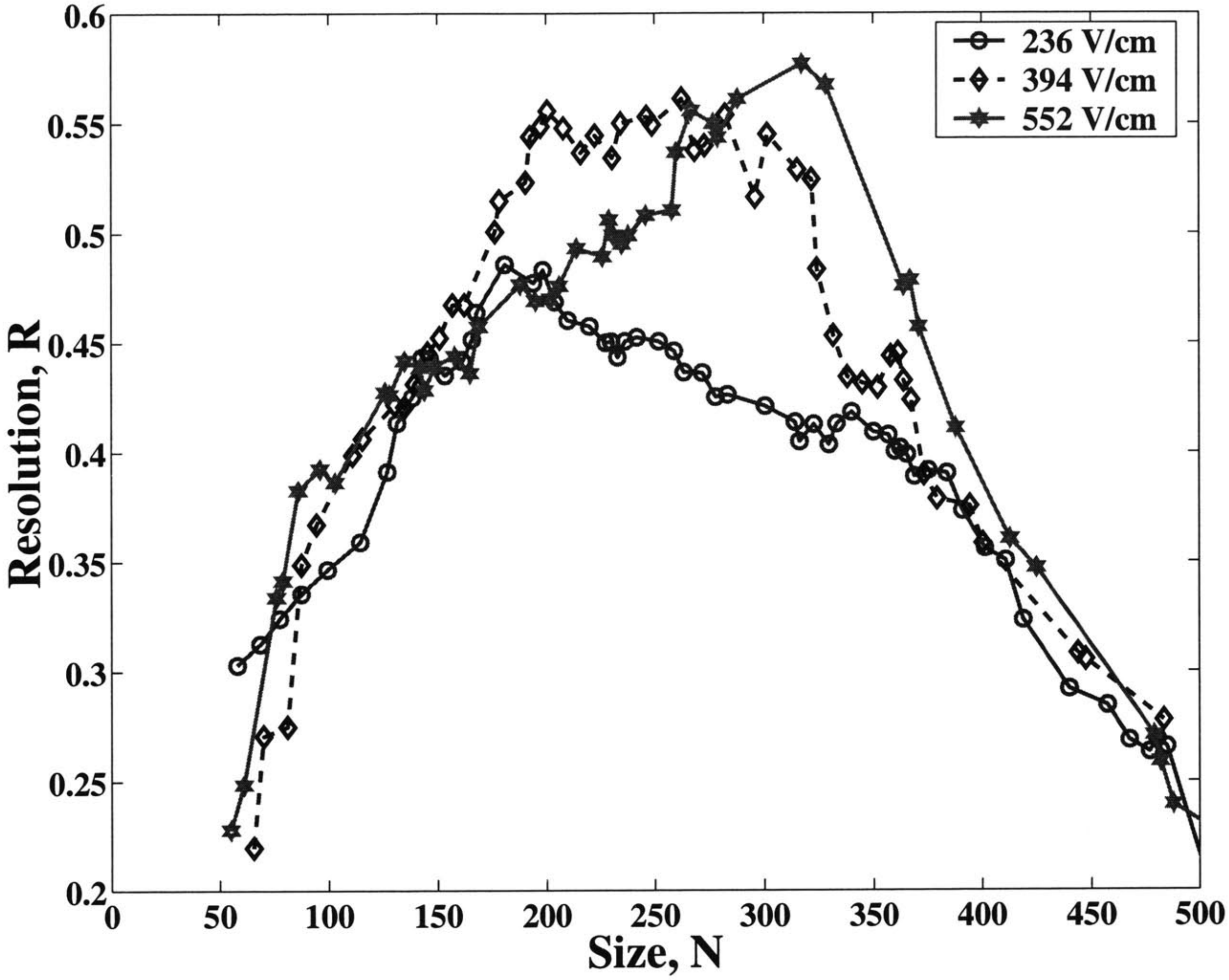

Figure 3-15: Resolution measurements obtained from separations that utilized a new high voltage protocol. Each curve represents the average resolution measurements obtained from at least 3 independent electrophoretic separations. Experiments were performed using a run voltage of 150 V/cm after a higher injection voltage, V_I, was applied for 5 seconds prior. Data from the lower injection voltage of 236 V/cm is denoted by red circular markers while data from 556 V/cm and 708 V/cm are denoted by blue diamond and red star-shaped markers, respectively. All separations utilized sequencing reactions purified with spin columns within identical 12-cm-long microdevices.

Table 3.6: Read-lengths and resolution measurements obtained from separations that utilized high-voltage injection protocols. All separations were performed using a run voltage of 150 V/cm within identical 250 μm-length injectors. Injections were performed at the elevated voltages denoted on the table. DNA samples were purified using spin columns and a 2% solution of 9 MDa LPA was used as the sieving matrix.

V_I (V/cm)	Read Lengths (Bases)	Bases of Highest R_L (Bases)	R_L (Average)
236	50 - 510	150 - 250	0.42
554	52 - 512	178 - 310	0.55
708	55 - 510	250 - 325	0.57

3.5 Conclusions

In this study, digital imaging has been used to explore the sample loading and electrophoretic injection of various populations of DNA molecules in microfabricated injectors. The distinct migration of molecules during sample-loading was well illustrated by the images, as was the complexity of DNA re-distribution during the stacking process. Data were analyzed using an N-Gaussian model that decomposed the sample into different velocity groups. The model can represent the observation that polydisperse samples develop distinct velocity groups within the overall sample plug. These groups were then identified as molecules that migrate with different electrophoretic mechanisms. This approach can be used to develop an empirical tool able to gauge the qualitative level of stacking experienced by DNA molecules under various conditions.

The intensity profiles gathered via digital imaging demonstrate the increased level of stacking induced by high voltage injections, while resolution measurements correlate their effects to separations. Stacking can be improved through buffer composition, novel device designs, and the high voltage protocols described here.

Chapter 4

Conclusions

4.1 Summary

This research has been one of the first comprehensive studies undertaken to enrich the electrophoretic separation of DNA within microdevices. Here, we have concisely outlined the theory of electrophoresis and, via experiments, also deepened our understanding of the electrophoretic process within microfabricated devices. Further, this research has demonstrated that DNA separations can be largely improved via careful inspection and re-examination of conventional loading and operational protocols. For example, in chapter 2, rheological study of the polymer matrix used for DNA separations identified remarkably high levels of shear-induced degradation imposed during conventional gel-loading protocols. Supplemental experiments also quantified the effects of this matrix degradation to the results of DNA separations. As a consequence of this particular study, gel-loading protocols have been redesigned to protect the properties of the external matrix and have produced separations with longer read-lengths and higher resolution. In chapter 3, fluorescence microscopy was used to capture the dynamics of DNA molecules unexpectedly induced by traditional sample-loading protocols. These results were adopted to construct an N-Gaussian model that accurately describes DNA migration during injection and also assists in the design of more optimized loading protocols. This distinctive research produced fundamental contributions to the field of DNA stacking, including a detailed exploration of the stacking process, a standardized method to measure the level of stacking exhibited by a system, and an empirical model to estimate the level of stacking attained with specific experimental parameters. Furthermore, higher levels of stacking were quantitatively correlated to increases in resolution via traditional electrophoretic experiments. Lastly, high voltage results underscored the need for additional optimization of operational protocols. Although ultra-high voltages were originally presumed detrimental to DNA separations, our experiments have verified increases in resolution when short durations of high voltage are applied during sample injection. These preliminary results demonstrate great promise for new sample-loading and upgraded operational protocols.

Overall, this research has produced significant and practical contributions to the electrophoresis industry. Developments realized through these experiments will assist in the design of novel new technologies and future microdevices. Further, by highlighting protocols that dramatically improve the performance of conventional systems, this work enables researchers to upgrade traditional electrophoretic systems as new techniques are developed. Lastly, the uniqueness of this research was due in large part to the integration of several engineering and science disciplines such as biology, fluid mechanics, microfabrication and fluorescence microscopy. Consistent inter-disciplinary research will undoubtedly continue to contribute significantly to the current and future study of electrophoretic techniques.

4.2 Future Outlook

This study has demonstrated that although electrophoresis has been widely practiced for over two decades, modifications of electrophoretic techniques remain unexplored. Further, the improvements proposed in this work illustrate the benefit of integrated engineering and manufacturing. In this section, we outline several anticipated future developments in the electrophoresis industry likely induced by the improvement of electrophoretic techniques, components, and applications to other biotechnology areas.

4.2.1 Polymer Matrixes

Extensive research in polymer chemistry has largely enhanced the electrophoretic separation of various biological molecules. Modern polymer blends show great promise for increased electrophoretic performance via increased sieving capacity and lower viscosity. Further, the need to consider gel-loading protocols, as demonstrated in chapter 2, may lead to the development of synthetic polymers resistant to shear-induced degradation. Advances such as these may change the entire nature of the sieving matrix, as well as remarkably alter the gel-loading process.

Developments in dynamic coatings have the potential to dramatically reduce the preparation time needed for microdevice electrophoresis. Further, newly synthesized coatings are working to increase separation efficiency via elimination of electro osmotic flow. These benefits will significantly streamline the current electrophoretic process and help incorporate microdevice electrophoresis into other cross-disciplinary biotechnologies.

4.2.2 Entropic Trapping

The evolution of the theories used to describe electrophoretic migration will undoubtedly impact the techniques used in future DNA separations. While the models of Ogston-type sieving and reptation are systematically reviewed and critiqued, the entropic barriers model is revolutionizing the methodology used for the separation of larger biomolecules. Advancements in the field of entropic trapping have already produced microdevices that achieve entropic separation of chromosomes and peptide fractionation [59]. Entropic separation of larger DNA molecules unaffected by conventional electrophoretic techniques will dramatically improve DNA sequencing technologies as well as stimulate biotechnology suppliers to develop more optimized sequencing reactions and PCR devices.

4.2.3 Microdevices

Although microfabricated channels are the latest development in electrophoresis, microdevices are undergoing extensive revision and optimization and are being incorporated into several different biotechnology applications. This combination introduces several new areas of research as well as interesting business opportunities. From an optimization standpoint, conventional microdevices have been predominantly rectangular, leaving room for novel designs that incorporate circular, triangular, or multi-channel geometries for sample-loading and separation. Further, the rapid adaptation of low-cost micromolding techniques is quickly antiquating the conventional BioMEMS manufacture described in chapter 1.3. Microdevices manufactured using plastics, or other disposable material, provide greater flexibility in channel design, and will facilitate the rapid integration of microdevices into the medical and forensics fields.

Some of the more recent developments in microdevices have been largely tied to massive parallelization efforts. The parallelization of electrophoretic lanes has enabled total process integration as well as the manufacture of completely automated electrophoretic systems. From a practical point of view, microdevices are ideally suited for parallelization because of their compactness, durability, and ability to produce results close to the theoretical performance limit of electrophoresis. With these attributes, multi-lane microdevices are likely to outperform older apparati comprised of multi-lane capillaries. Parallelization is also significant on a component basis, as traditional robotic systems designed for multi-lane sample loaders are being quickly upgraded and incorporated into total process systems. In addition, the requirements of the detection systems needed for larger microdevices will stimulate new designs in opto-electronic engineering.

On a larger scale, microdevice electrophoresis is certain to dominate the forthcoming Protenomic project [4], already in progress at select institutions. Although capillary electrophoresis was predominantly used for the sequencing of the Human Genome, biologists are rapidly incorporating microdevices into their study of protein folding and crystallization. Microfabricated channels are already largely used to analyze and determine the folding structures of several key proteins. As shown in chapter 3, the study of macromolecular dynamics within microdevices is well complemented by fluorescence microscopy and has already led to significant discoveries. As a result, microdevices are expected to play a key role in the Protenomics world and will certainly produce breakthroughs in protein analysis.

Overall, the integration of microdevices with biology-related processes provides an abundant area of research. It is a remarkably growing area of biotechnology with great promise for current and future applications. The general review of electrophoresis presented in this text, coupled with an outline of the benefits and possibilities of microdevices, has hopefully encouraged the reader to pursue his or her interest in biotechnology. It is exciting to live in a time where traditional fields such as medicine and drug treatment are revolutionized by novel, inter-disciplinary research. It brings even greater excitement to see that microdevices are the first step towards this future.

Bibliography

[1] Probstein, R.F. *PhysicoChemical Hydrodynamics*, 2nd Edition, John Wiley Sons, New York, NY 1994.

[2] Ohanian, H.C. *Physics*, 2nd Edition, W.W. Morton and Company, San Francisco, 1980.

[3] Smithies, O. *Biochem. J., 61, 629, 1955.*

[4] Lander, E.S. et al. *Nature, 2001,409, pp860-925.*

[5] Schmalzing D.; Adourian A.; Koutny L.; Ziaugra L.; Matsudaira P.; Ehrlich D. *Anal. Chem. 1998, 70, pp2303-2310.*

[6] Schmalzing, D.; Koutny, L,; Adourian, A.; Belgrader, P.; Matsudaira, P.; Ehrlich, D. *Proc. Natl. Acad. Sci., 1997, 94, pp10273-10278.*

[7] Petersen, K.E.; McMillian, W.A.; Kovacs, G.T.A.; Northup, M.A.; Christel, A.; Pourahmadi, F. *J. Biomedical Devices, 1998, 1, pp71-79.*

[8] Eigen, M.; Rigler, R. *Proc. Natl. Acad. Sci., 1991, 91, pp5740-5747.*

[9] Salas-Solano, O.; Carrilho, E.; Kotler, L.; Miller, A.W.; Goetziinger, W.; Sosic, Z.; Karger, B.L. *Anal. Chem., 1998, 70, pp3996-4003.*

[10] Grossman, P.D.; Colburn, J.C. *Capillary Electrophoresis, Theory and Practice*, Academic Press, Inc., San Diego, 1992.

[11] Hoagland, D.A.; Smisek, D.L.; Chen, D.Y. *Electrophoresis, 1996, 17, pp1151-1160.*

[12] Purves, W.K.; Orians, G.H.; Heller, H.C. *Life: The Science of Biology*, 4th Edition, W.H. Freeman and Company, New York, NY 1995.

[13] Kroschwitz,K. ed., *Encyclopedia of Chemical Technology,* 4th Edition, John Wiley Sons, 1994.

[14] Stryer, L. *Biochemistry*, 3rd Edition, W.H. Freeman and Company, New York, 1988.

[15] Atkins, P. *Physical Chemistry*, 5th Edition, W.H. Freeman and Company, New York, NY 1996.

[16] Cottet, H.; Gareil, P. *Electrophoresis, 2000, 21, pp1493-1504.*

[17] Rousseau, J.; Drouin, G.; Slater, G.W. *Electrophoresis, 2000, 21, pp1464-1470.*

[18] Mosher, R.A.; Saville, D.A.; Thormann, W. *The Dynamics of Electrophoresis*, VCH Publishers, London, 1988.

[19] Westermeier, R. *Electrophoresis in Practice,* 3rd Edition, Wiley-VCH, Weinheim, 2000.

[20] Tiselius, A. *Trans. Faraday. Soc., 1937, 33, pp524-530.*

[21] Dole, V.P. *J. Phys., 1945, 67, pp1119-1125.*

[22] Longsworth, L.G. *J. Phys., 1943, 61, pp1755-1765.*

[23] Raymond, S. and Weintraub, L. *Science, 1959, 130, pp711-712.*

[24] Gorg, A.; Obermaier, C.; Boguth, G.; Harder, A.; Scheibe, B.; Wildgruber, R.; Weiss, W. *Electrophoresis, 2000, 21, pp1037-1053.*

[25] Townshend, A.; editor, *Encyclopedia of Analytical Science*, vol. 2, Harcourt Brace and Company, 1995, p. 1041.

[26] Gebauer, P.; Thormann, W.; Bocek, P. *Electrophoresis, 1995, 21, pp11-19.*

[27] Magnusdottir, S.; Isambert, H.; Heller, C.; Viovy, J.L. *Biopolymers, 1999, 49, pp385-401.*

[28] Palusinksi, O.A.; Graham, A.; Mosher, R.A.; Bier, M.; Saville, D.A. *AIChE Journal, 1986, 32, pp205-223.*

[29] Larson, R.G.; Hu, H. *J. Rheol. 1999, 43, pp267-304.*

[30] Viovy, J.L. *Rev. Mod. Phys., 2000, 72, pp813-872.*

[31] Heiger, D.N.; Cohen, A.S.; Karger, B.L.; *J. Chrom. 1990, 516, pp33-48.*

[32] Cohen, A.S.; Najarian, D.R.; Karger, B.L.; *J. Chrom. 1990, 526, pp49-60.*

[33] Marko, J.F.; Siggia, J.D. *Macromolecules, 1995, 28, pp8750-8770.*

[34] Dhara, D.; Chatterji, P.R. *J. Phys. Chem. B, 1999, 103, pp8458-8461.*

[35] Simpson, P.C.; Woolley, A.T.; Mathies, R.A. *J. Biomedical Devices, 1998, 1, pp7-26.*

[36] Liu, S.; Ren, H.; Gao, Q.; Roach, D.J.; Loder, R.T.; Armstrong, T.M.; Mao, Q.; Blaga, I.; Barker, D.L.; Jovanovich, S.B. *Proc. Natl. Acad. Sci., 2997, 97, pp5369-5374.*

[37] Backhouse, C.; Caamano, M.; Oaks, F.; Nordman, E.; Carrillo, A.; Johnson, B.; Bay, S. *Electrophoresis, 2000, 21, pp150-156.*

[38] Krivacsy, Z.; Gelencser, A.; Hlavay, J.; Kiss, G.; Sarvari, Z. *J. Chrom. A, 1999, 834, pp21-44.*

[39] Waki, S.; Harvey, J.D. *Biopolymers, 1982, 21, pp1901-1926.*

[40] Cifuentes, A.; Canalejas, P.; Diez-Masa, J.C. *J. Chrom. A., 1999, 830, pp423-438.*

[41] Semenov, A.N.; Rubinstein, M. *Eur Phys. J. B.,1998, 1, pp87-94.*

[42] Duke, T.; Viovy, J.L.; Semenov, A.N. *Biopolymers, 1994, 34, pp239-247.*

[43] Mitnik, L.; Salome, L.; Viovy, J.L.; Heller, C. *J. Chrom. A, 1995, 710, pp309-321.*

[44] Heller, C. *Electrophoresis, 2001, 22, pp629-643.*

[45] Lumpkin,O.; Dejardin, P.; Zimm,B. *Biopolymers, 1985, 24, pp 1573-1593.*

[46] Jorgenson, J. W.; Lukacs, K. D. *Anal. Chem., 1981, 53, pp1928-1934.*

[47] Jorgenson, J. W.; Lukacs, K. D. *Science, 1983, 222, pp266-267.*

[48] Quirino, J.P.; Terabe, S. *J. Chrom. A, 1999, 856, pp465-482.*

[49] Altria, K.D. *J. Chrom. A., 1999, 856, pp443-463.*

[50] Heller, C. *Electrophoresis 1999, 20, pp1962-1977.*

[51] Nishikawa, T.; Kambara, H. *Electrophoresis, 1996, 17, pp1115-1120.*

[52] Jorgenson, J. W. *Analytical Chemistry, 1986, 58, 7, 743A.*

[53] Grushka, E.; McCormick, R.M.; Kirkland, J.J. *Anal. Chem., 1989, 61, pp241-246.*

[54] Hjerten, S. *J. of Chrom., 1985, 347, pp191-198.*

[55] Guttman, A. *Anal. Chem., 1999, 71, pp3598-3602.*

[56] Fan, Z.H.; Harrison, J. *Anal. Chem., 1994, 66, pp177-184.*

[57] PE Applied Bio Systems *1998 Automated DNA Sequencing/ABI Prism 310 User's Manual,* Foster City, CA.

[58] Bullard, K.M.; Hietpas, P.B.; Ewing, A.G. *J. Biomedical Devices, 1998, 1, pp27-37.*

[59] Turner, S.W.; Craighead, H.G. *J. Physics. B, 1999, 3258, pp 114-121.*

[60] Chou, H.P.; Spence, C.; Scherne, A.; Quake, S. *Proc. Natl. Acad. Sci., 1998, 96, pp11-13.*

[61] Shultz-Lockyear L.L.; Colyer, C.; Fan, Z.H.; Roy, K.I.; Harrison, D.J. *Electrophoresis, 1999, 20, pp529-538.*

[62] Paegel, B.M.; Hutt, L.D.; Simipson, P.C.; Mathies, R.A. *Anal. Chem., 2000, 72, pp3030-3037.*

[63] Luckey, J.A.; Norris, T.B.; Smith, L.M. *J. Phys. Chem. 1993, 97, pp3067-3075.*

[64] Luckey, J.A.; Smith. L.M. *Anal. Chem.,1993, 65, pp2841-2850.*

[65] Wennmalm, S.; Edman, L.; Rigler, R. *Proc. Natl. Acad. Sci., 1997, 94, pp10641-10646.*

[66] Heller, C. *Electrophoresis, 2000, 21, pp593-602.*

[67] Russel, W.B.; Saville, D.A.; Schowalter, W.R. *Colloidal Dispersions,* 2nd Edition, Cambridge University Press, 1990

[68] Leger, L.; Viovy, J.L. *Contemp. Phys., 1988, 29, pp579-595.*

[69] Larson, R.G.; *The Structure and Rheology of Complex Fluids*, Oxford Press, New York, 1999.

[70] Graessley, W.W.; *Adv. Polym. Sci., 1982, 47 68.*

[71] White, F.M. *Fluid Mechanics*, 4th Edition, McGraw-Hill, Boston, MA 1999

[72] Sonntag, R.E.; Borgnakke, C.; Van Wylen, G.J. *Fundamentals of Classical Thermodynamics*, 5th Edition, John Wiley Sons, New York, NY 1998.

[73] Castellanos, A. *Electrodynamics*, Springer Publishers, Wien, 1998.

[74] Oosawa, F. *Polyelectrolytes*, The M.I.T Press, Cambridge, MA 1974.

[75] Ohanian, H.C. *Classical Electrohydrodynamics*, 3rd Edition, W.W. Morton and Company, San Francisco, 1987.

[76] Halliday, D.; Resnick, R. *Fundamentals of Physics,* 3rd Edition, John Wiley Sons, New York, NY, 1980.

[77] Thomas, G.B.; Finney, R.L. *Calculus and Analytical Geometry,* 7th Edition, Addison-Wiley Publishers, Reading, MA 1988.

[78] Candau, F.; Ottewill, R.H. *An Introduction to Polymer Colloids*, Kluwer Academic Publishers, Dordrecht, 1990.

[79] Loeb, A.L.; Overbee, J.T.G.; Wiersema, P.H. *The Electric Double Layer Around a Spherical Colloid Particle,* The M.I.T. Press, Cambridge, MA 1961.

[80] Lee, E.; Yen, F.Y.; Hsu, J.P. *Electrophoresis, 2000, 21, pp475-480.*

[81] Molho, J.I.; Herr, A.E.; Mosier, B.P.; Santiago, J.P.; Kenny, T.W. *Anal. Chem. 2000,*

[82] Neuhoff, V. *Electrophoresis, 2000, 21, pp3-11.*

[83] Brahmasandra, S.N.; Ugaz, V.M.; Burke, D.T.; Mastrangelo, C.H.; Burns, M.A. *Electrophoresis, 2001, 22, pp300-311.*

[84] Schroder, E.; Muller, G.; Arndt, K.F. *Polymer Characterization,* Hanser Publishers, Munich 1988.

[85] Carreau, P.J.; De Kee, D. C.R.; Chhabra, R.P. *Rheology of Polymeric Systems,* Hanser Publishing, Munich, 1997.

[86] Cluzel, P.; Lebrun, A.; Heller, C.; Lavery, R.; Viovy, J.L.; Chatenay, D.; Caron, F. *Science, 1996, 271, pp792-794.*

[87] Bustamante, C. *Annual. Rev. Biophys. Chem., 1991, 20, pp415-446.*

[88] Foret, F.; Krivankova L.; Bocek, P. *Capillary Zone Electrophoresis,* VCH Publishers, Weinheim 1993.

[89] Grosberg, A.Y.; Khokhlov, A.R. *Giant Molecules: Here there and Everywhere*, Academic Press, Boston 1997.

[90] Clay, J.D.; Koelling, K.W. *Poly. Engr. Sci., 1997, 37, pp 793-805.*

[91] deGennes, P.G. *Scaling Concepts in Polymer Physics,* Cornell Publishers, Ithaca NY 1989.

[92] Viovy, J.L.; Duke, D.S. *Electrophoresis, 1993, 14, pp322-329.*

[93] Smith, S.B.; Bendich, A.J. *Biopolymers, 1989, 29, pp1167-1173.*

[94] Chern,S.; Coalson, R. *J. of Chem. Phy., 1999, 111, pp1778-1781*

[95] Smisek, D.; Hoagland,D. *Science, 1990, 248, pp1221-1223.*

[96] Muthukumar, M.; Baumgartner, A. *Macromolecules, 1989, 22, pp 1941-1946.*

[97] Slater,G.; Wu, S. *Phy. Rev. Let., 1995, 75, pp 164-167.*

[98] Han, J.; Turner, S.; Craighead, H. *Phy. Rev. Let., 1999, 83, pp 1688-1691*

[99] Sluder, G.; Wolf, D.E. *Video Microscopy,* Academic Press, San Diego, 1998.

[100] Ingoue, S.; Spring, K.R. *Video Microscopy: The Fundamentals,* Plenum Publishing, New York, NY 1997.

[101] Edmund Industrial Optics *Electronic Imaging Components,* Electronic Imaging Resource Guide, Edmund Scientific Company, New Jersey, 1999.

[102] Johnson, I.D. *Introduction to Fluorescent Techniques,* Molecular Probes Catalog, 1996, pp1-4.

[103] Haab, B.B.; Mathies, R.A. *Anal. Chem., 1995, 67, pp3252-3260.*

[104] Austin, R.H.; Volkmuth,D. *Nature, 1992, 358, pp600-601.*

[105] Quake, S.R. *Science, 2000, 290, pp1536-1540.*

[106] Slater, G.W.; Guo, H.L. *Electrophoresis, 1996, 17, pp977-988.*

[107] Rousseau,J; Drouin,G.; Slater, G.W. *Phys. Rev. Let., 1997, 79, pp1945-1948*

[108] Muthukumar, M.; Baumgartner, A. *Macromolecules, 1989, 22, pp 1937-1941*

[109] Slater, G.; Rousseau, J.; Turmel,C.; Lalande, M. *Biopolymers, 1988, 27, pp 509-524*

[110] Arvanitidou, E.; Hoagland, D.;Smisek, D. *Biopolymers, 1991, 31, pp 435-447*

[111] Starkweather, M.E.; Muthukumar, M.; Hoagland, D.A. *Macromolecules, 1999, 32, pp6837-6840.*

[112] Slater, G.W.; Noolandi, J. *J. Biopolymers, 1985, 24, pp2181-2185.*

[113] Vazquez, M.; Schmalzing, D.; Matsudaira, P.; Ehrlich, D.; McKinley, G. *Anal. Chem., 2001, 73, pp3035-3044.*

[114] Kohn, J., A; *Clin. Chim. Acta, 1957, 2, pp297-299.*

[115] Ornstein, L.; Davis, B. J.; *Disc Electrophoresis, Distillation Products Industries (Division of Eastman Kodak Co.), 1959.*

[116] Cifuentes, A.; Poppe, H. *Chromatographia, 1994, 39, pp391-399.*

[117] Heiger, D.N.; Cohen, A.S.; Karger, B.L.; *J. Chrom., 1990, 516, pp33-48.*

[118] Cohen, A.S.; Najarian, D.R.; Karger, B.L.; *J. Chrom., 1990, 526, pp49-60.*

[119] Sunada, W.M.; Blanch, H.W. *Electrophoresis, 1997, 18, pp2243-2254.*

[120] Carrilho, E.; Ruiz-Martinez, M.C.; Berka, J.; Smirnov, I.; Goetzinger, W.; Miller, A.W.; Brady, D.; Karger, B.L. *Anal. Chem., 1996, 68, pp3305-3313.*

[121] Wu, C., Quesada, M.A.; Schneider, D.K.; Farinato,R., Studier, F.W.; Chu, B. *Electrophoresis, 1996, 17, pp1103-1109.*

[122] Carlsson, C.; Larsson, A. *Analysis of Nucleic Acids by Capillary Electrophoresis,* Vieweg, Wiesbaden 199, pp67-89.

[123] Heller, C. *Electrophoresis, 1999, 20, pp1978-1986.*

[124] Molecular Dynamics *MegaBase 1000 Training 1999* Sunnyvale, CA.

[125] Fay, J.A. *Introduction to Fluid Mechanics,* The M.I.T. Press, Cambridge MA 1994.

[126] Doi, M.; Edwards, S.F. *The Theory of Polymer Dynamics,* 2nd Edition, Oxford University Press, Oxford, 1986.

[127] Brandup, I.; *Polymer Handbook,* 3rd Edition, John Wiley and Sons; New York 1989.

[128] Clay, J.D.; Koelling, K.W. *Poly. Engr. Sci., 1997, 37, pp 793-805.*

[129] Hubert S.J.; Slater, G.W.; Viovy, J.L *Macromolecules, 1996, 29, pp1006-1009.*

[130] Slater, G.W.; Kist, T.B.L.; Ren, H.; Drouin, G. *Electrophoresis, 1998, 19, pp3133-3142.*

[131] Kulicke, W.M.; Kniewske, R.; Klein, J. *Proceed. Poly. Sci., 1992, 8, pp373-468.*

[132] Grossman, P.D.; Soane, D.S. *J. of Chromatogr., 1991, 559, pp257-266.*

[133] Graessley, W.M. *Adv. Poly. Sci., 1980, 21, pp258-262.*

[134] Bouldin, M.;Kulicke, W.M.; Kehler, H. *Colloid Poly. Sci., 1998, 266, pp763-805.*

[135] Cottet, H.; Gareil, P.; Viovy, J.L. *Electrophoresis, 1998, 19, pp2151-2162.*

[136] Nguyen, T.Q.; Kausch, H.H. *Colloid Poly. Sci., 1991, 269, pp1099-1110.*

[137] Kim, S.; Hobbie, E.K.; Yu, J.W.; Han, C.C. *Phys. Fluid Plas. Biophys., 1998, 20, pp2301-2314.*

[138] Flew, S.; Sellin, R.H.J. *J. Non-Newt. Fluid Mech., 1993, 47, pp169-210.*

[139] Scott, J.P.; Fawell, P.D.; Ralph, D.E.; Farrow, J.B. *J. App. Poly. Sci., 1996, 62, pp2097-2106.*

[140] D'Almeida, A.R.; Dias, M.L. *Poly. Degr. Stab., 1997, 56, pp331-337.*

[141] Goetzinger, W; Kotler, L; Carrilho, E.; Ruiz-Martinez, M.C.; Salas-Solano, O.; Karger, B.L. *Electrophoresis, 1998, 19, pp242-248.*

[142] Munk, P.; Aminalhavi, T.M.; Williams, P.; Hoffman, D.E. *Macromolecules, 1980, 13, pp871-875.*

[143] Lagally, E.T.; Mathies, R.A. *Anal. Chem., 2001, 73, pp565-570.*

[144] Viovy, J.L. *Rev. Mod. Phys., 2000, 72, pp813-872.*

[145] Ruiz-Martinez, M.C.;Berka, J.; Belenkii, A.; Foret, F.; Miller, A.W.; Karger, B.L. *Anal. Chem., 1993, 20, pp2851-2852.*

[146] Larson, G. *Introduction to the Dynamics of Polymer Molecules,* John Wiley and Sons, Ann Arbor 1992.

[147] Perkins, T.T.; Smith, D.E.; Chu, S. *Science, 1997, 276, pp2016-2021.*

[148] Sassi, A.P.; Barron, A.; AlonsoAmigo, M.G.; Hion, D.Y.; Soane, D.S.; Hooper, H.H. *Electrophoresis, 1996, 17, pp1460-1469.*

[149] Pariat, Y.F.; Berka, J.; Heiger, D.N.; Schmitt, T.; Vilenchik, M.; Cohen, A.S., Foret, F.; Karger, B.L. *J. of Chrom. A., 1993, 652, pp57-66.*

[150] Hebenbrock, K; Williams, P.M.; Karger, B.L. *Electrophoresis, 1995, 16, pp1429-1436.*

[151] Berka, J.; Pariat, Y.F.; Muller, O.; Hebenbrock, K.; Heiger, D.N.; Foret, F.; Karger, B.L. *Electrophoresis, 1995, 16, pp377-388.*

[152] Foret, F.; Szoko, E.l Karger, B.L. *Electrophoresis, 1993, 14, pp417-428.*

[153] Wu, Y.C.; Berezansky, P.A. *Low Electrolyte Conductivity Standards J. Res. Natl. Inst. Stand. Technol., 1995, 100, pp521-527.*

[154] Beckers, J.L.; Bocek, P. *Electrophoresis, 2000, 21, pp2747-2767.*

[155] Zhang, C.X.; Thormann, W. *Anal. Chem., 1996, 68, pp2523-2532.*

[156] Quirino, J.P.;Terabe, S. *J. Chrom. A, 1999, 850, pp339-344.*

[157] Guirino, J.P.; Terabe, S. *Electrophoresis, 2000, 21, pp355-359.*

[158] Heller, C. *Electrophoresis, 2001, 21, pp593-602.*

[159] Bird, R.B.; Armstrong, R.C.; Hassager, O. *Dynamics of Polymeric Liquids v.1,* John Wiley and Sons, New York 1987.

[160] Bird, R.B.; Armstrong, R.C.; Hassager, O. *Dynamics of Polymeric Liquids v.2,* John Wiley and Sons, New York 1987.

[161] www.prsm.usm.edu

[162] Lumpkin, O.J.; Dejardin, P.; Zimm, B.H. *Biopolymers, 1985, 24, pp. 1573-1578.*

[163] Ladoux, B.; Quivy, J.P.; Doyle, P.; duRoure, O.; Almouzni, G.; Viovy, J.L. *Proc. Natl. Acad. Sci., 2000, 97, pp14251-14256.*

[164] Starkweather, M.E.; Muthukumar, M.; Hoagland, D.A. *Macromolecules, 1998, 31, pp5495-5501.*

[165] Ogston, A.G. *Trans. Faraday Soc. 1958, 54, pp1754-1757.*

[166] Heller, C. *Electrophoresis, 2001, 22, pp629-643.*

[167] www.magnet.ions.com

[168] Bakajin, O.B.; Brody, J.P.; Chou, C.F.; Chan, S.S.; Duke, T.A.J.; Knight, J.; Sohn, L.; Vishwanath, A.; Austin, R.H.; Cox, E.C. *J. Polymer Dynamics, Vol. 3258*

[169] Kleparnik, K.; Garner, M.; Bocek, P. *J. Chrom. A., 1995, 698, pp375-383.*

[170] de Boer, T.; Ensing, K. *J. Chrom. A., 1997, 788, pp212-217.*

[171] Shihabi, Z.K. *J. Chrom. A., 1999, 853, pp3-9.*

[172] Dose, E.V.; Guiochon, G. *Anal. Chem., 1992, 64, pp123-128.*

[173] Kuban, P.; Tennberg, K.; Tryzell, R.; Karlberg, B. *J. Chrom. A, 1998, 808, pp219-227.*

[174] Lee, T.T.; Yeung, E.S. *Anal. Chem., 1992, 64, pp1226-1231.*

[175] Sakata-Sogawa, K.; Kurachi, M.; Sogawa, K.; Fujii-Kuriyama. Y.; Tashiro, H. *Eur Biophys J, 1998, 27, pp55-61.*

[176] Jacobson, S.C.; Hergenroder, M.; Koutny, L,B.; Warmack, R.J.; Ramsey, J.M. *Anal. Chem., 1994, 66, pp 1107-1113.*

[177] He, Y.; Lee, H.K. *Anal. Chem., 1999, 71, pp995-1001.*

[178] Morales, S.;Cela, R. *J. Chrom. A., 1999, 846, pp401-411.*

[179] Palmer, J.; Munro, N.J.; Landers, J.P. *Anal. Chem., 1999, 71, pp1679-1687.*

[180] Sjogren, A.; Dasgupta, P.K. *Anal. Chem., 1996, 68, pp1933-1940.*

[181] Taylor, J.R. *An Introduction to Error Analysis,* University Science Books, Mill Valey, CA, 1982.

[182] Arvanitidou,E.; Hoagland, D. *Phy. Rev. Let., 1991, 67, pp 1464-1466*

[183] Smith, D.E.; Perkins, T.T.; Chu, S. *Macromolecules, 1996, 29, pp1373-1373.*

[184] Barker, S.L.R.; Tarlov, M.J.; Gaitan, M.; Locascio, L.E. *Anal. Chem., 2000, 72, pp5925-5929.*